

CLUSTER STRUCTURE AND THREE-BODY DECAY IN  $^{14}\text{C}$

By

Lisa Marie Carpenter

A DISSERTATION

Submitted to  
Michigan State University  
in partial fulfillment of the requirements  
for the degree of

Physics – Doctor of Philosophy

2019

## ABSTRACT

### CLUSTER STRUCTURE AND THREE-BODY DECAY IN $^{14}\text{C}$

By

Lisa Marie Carpenter

Recent model calculations with most advanced methods for cluster states have shown the need of experimental data to probe the structure of light exotic nuclei, including those with  $\alpha$ -clustering, such as  $^{14}\text{C}$ .

The prototype Active Target Time Projection Chamber (pAT-TPC) was used in the present study. The pAT-TPC is a gas-filled thick-target detector with high luminosity and full kinematic acceptance. This type of detector gives access to a full excitation function with a single beam energy.

The measurements in this work were carried out by resonant alpha-scattering of a  $^{10}\text{Be}$  beam at 38 and 20 MeV delivered by the *TwinSol* facility at the University of Notre Dame. These experiments measured resonances in  $^{14}\text{C}$  that can be compared to models by using R-Matrix reaction theory. Two new negative parity resonances were identified at high excitation energies. Additionally, using a Dalitz-type analysis, three-body decays were analyzed to determine probabilities of "democratic" and "sequential" decay. Increasing probability of democratic decay was found at high energy. Results were interpreted using Gamow Shell Model and Anti-Symmetrized Molecular Dynamics calculations which are described in detail.

Copyright by  
LISA MARIE CARPENTER  
2019

## ACKNOWLEDGEMENTS

First and foremost, I would like to thank my advisor, Wolfgang Mittig. You have been an incredible, optimistic mentor through an at-times-trying project. You have taught me so much about nuclear physics, including the value of drawing a picture and the usefulness of “scotch”. I have appreciated your tenacity, knowledge, and patience as I learn.

The rest of the AT-TPC group over the course of my time in graduate school has been very valuable with guiding my PhD and for bouncing ideas and frustrations off. These people include Daniel Bazin; a cavalcade of post-docs: Clementine Santamaria, Yassid Ayyad, Jaspreet Randhawa, Saul Beceiro-Novo, and Tan Ahn; and fellow students Josh Bradt and Nate Watwood.

There are so many other people that deserve thanks that are too numerous to name including the rest of the community of graduate students in the NSCL and physics department, the people who taught me physics both at Bucknell and MSU, and the support staff in both buildings.

Last, but certainly not least, I would like to thank my guidance committee: Wolfi, Daniel, Carl Bromberg, Scott Pratt, and Vladimir Zelevinsky for reading this document and helping me along this path.

## TABLE OF CONTENTS

<b>LIST OF TABLES . . . . .</b>	<b>vii</b>
<b>LIST OF FIGURES . . . . .</b>	<b>viii</b>
<b>CHAPTER 1 INTRODUCTION . . . . .</b>	<b>1</b>
1.1 Nuclei . . . . .	1
1.2 Clustering . . . . .	6
1.3 Previous Work . . . . .	8
1.3.1 Hoyle State . . . . .	8
1.3.2 Carbon-14 . . . . .	9
<b>CHAPTER 2 THEORY . . . . .</b>	<b>13</b>
2.1 Antisymmetrized Molecular Dynamics . . . . .	13
2.2 <i>Ab initio</i> Calculations . . . . .	22
2.3 R-Matrix Reaction Theory . . . . .	24
2.4 Three-Body Theory . . . . .	31
<b>CHAPTER 3 EXPERIMENT . . . . .</b>	<b>36</b>
3.1 pAT-TPC . . . . .	36
3.1.1 Micromegas . . . . .	41
3.1.2 Electronics . . . . .	44
3.2 Beam Facility . . . . .	44
3.2.1 Tandem Accelerator . . . . .	45
3.2.2 TwinSol . . . . .	46
3.3 Experimental Setup . . . . .	46
<b>CHAPTER 4 ANALYSIS AND RESULTS . . . . .</b>	<b>48</b>
4.1 Two-Body Events at Low Energy . . . . .	48
4.1.1 Reconstruction . . . . .	48
4.1.2 Simulation . . . . .	52
4.1.3 Analysis . . . . .	53
4.1.4 Results and Discussion . . . . .	57
4.2 Two-body Events at High Energy . . . . .	59
4.2.1 Reconstruction . . . . .	59
4.2.2 Analysis . . . . .	61
4.2.3 Interpretation . . . . .	69
4.2.4 Comparisons to Shell Model . . . . .	70
4.3 Three-Body Events . . . . .	72
4.3.1 Simulations . . . . .	73
4.3.2 Dalitz Plots . . . . .	74
4.3.3 Angular Correlation Plot . . . . .	76
4.3.4 Analysis and Results . . . . .	81

<b>CHAPTER 5 CONCLUSIONS . . . . .</b>	<b>83</b>
5.1 Future Work . . . . .	83
5.1.1 Detector Improvements . . . . .	83
5.1.2 Analysis Improvements . . . . .	85
5.2 Conclusion . . . . .	86
<b>BIBLIOGRAPHY . . . . .</b>	<b>88</b>

## LIST OF TABLES

Table 1.1: Experimentally Known States . . . . .	12
Table 2.1: $\beta$ and $\gamma$ Values . . . . .	18
Table 2.2: Typical Optical Model Parameters . . . . .	27
Table 4.1: Optical Model Parameters . . . . .	64
Table 4.2: Calculated resonance parameters . . . . .	65
Table 4.3: Comparison With Previous Work . . . . .	71
Table 4.4: Three-Body Acceptance . . . . .	79
Table 4.5: Three-Body Fit Results . . . . .	82

## LIST OF FIGURES

Figure 1.1: Breit-Wigner Form . . . . .	3
Figure 1.2: Known Energy Levels of $^{14}\text{C}$ . . . . .	4
Figure 1.3: Levels and Decays of $^{14}\text{C}$ . . . . .	5
Figure 1.4: Ikeda Diagram . . . . .	7
Figure 1.5: Example Arrangements of Clusters in $^{12}\text{C}$ . . . . .	8
Figure 1.6: Experimental Setup of [18] . . . . .	10
Figure 1.7: Summary of Linear Chain Cluster States . . . . .	11
Figure 1.8: Linear and Triangular Clusters . . . . .	12
Figure 2.1: Positive Parity Energy Surfaces . . . . .	16
Figure 2.2: Negative Parity Energy Surfaces . . . . .	17
Figure 2.3: Positive Parity AMD Wavefunctions for $^{14}\text{C}$ . . . . .	19
Figure 2.4: Negative Parity AMD Wavefunctions for $^{14}\text{C}$ . . . . .	20
Figure 2.5: AMD Energy Levels . . . . .	21
Figure 2.6: $\pi$ and $\sigma$ bonds . . . . .	22
Figure 2.7: Gamow-Teller Strengths . . . . .	24
Figure 2.8: Example Woods-Saxon . . . . .	26
Figure 2.9: Jacobi T and Y Coordinates . . . . .	33
Figure 2.10: Intercluster Distances . . . . .	34
Figure 2.11: Angular Distributions . . . . .	35
Figure 3.1: Electric Field Uniformity . . . . .	37
Figure 3.2: Prototype Active Target Time Projection Chamber . . . . .	39

Figure 3.3: Photograph of Flange	39
Figure 3.4: Operation of the pAT-TPC	40
Figure 3.5: pAT-TPC and AT-TPC	41
Figure 3.6: Micromegas Operations	42
Figure 3.7: Backgammon Micromegas	43
Figure 3.8: Backgammon Detail View	43
Figure 3.9: Layout of ISNAP	45
Figure 3.10: Experiment Setup	47
Figure 4.1: Hough Space Example	50
Figure 4.2: Hough vs Linear Fit	51
Figure 4.3: Low-Energy Detector Acceptance	53
Figure 4.4: Low Energy Two-Body Kinematics	54
Figure 4.5: Energy Resolution	55
Figure 4.6: Low-Energy Excitation Function	56
Figure 4.7: Low-Energy R-Matrix Calculation	57
Figure 4.8: Low-Energy Excitation Function Projections	58
Figure 4.9: RANSAC method	59
Figure 4.10: Example RANSAC Reconstructions	61
Figure 4.11: High Energy Excitation Function	62
Figure 4.12: Inelastic Scattering Excitation Function	63
Figure 4.13: Calcualted excitation function	66
Figure 4.14: Comparison of Calculation and Experiment near 9.5 MeV	67
Figure 4.15: Comparison of Calculation and Experiment near 10.3 MeV	68

Figure 4.16: $5^-$ Summary . . . . .	69
Figure 4.17: NuShellX Calculation . . . . .	72
Figure 4.18: Three-Body Channels . . . . .	73
Figure 4.19: Three-Body Decay Energy Levels . . . . .	75
Figure 4.20: Dalitz Plots . . . . .	77
Figure 4.21: $\varphi$ Resolution . . . . .	78
Figure 4.22: Simulated Angular Correlation Plots . . . . .	80
Figure 4.23: Experimental Angular Correlation Plot . . . . .	81
Figure 5.1: New Micromegas Design . . . . .	84
Figure 5.2: SOLARIS . . . . .	85

## CHAPTER 1

### INTRODUCTION

#### 1.1 Nuclei

A nucleus consists of a specific number of protons and neutrons which are together called nucleons. The number of protons is called the atomic number and given the variable  $Z$ . This number determines the element of a nucleus. The number of neutrons,  $N$ , determines which isotope the nucleus is of that element element. The total number of nucleons is  $A$ . These are related by  $Z + N = A$ . This is typically represented by  ${}^A_E$  where  $E$  is the chemical symbol for the element with atomic number  $Z$ . With this notation,  ${}^{14}\text{C}$  is an isotope of Carbon, which is composed of six protons, with a total of 14 nucleons, which implies that there are eight neutrons. Nucleons have a mass on the order of  $1 \text{ GeV}/c^2$  and are bound together with a binding energy on the order of  $1 \text{ MeV/nucleon}$ . The nucleus can be in an excited state that increases the total energy of the nucleus. This energy is quantized in a way that is similar to electron shells in atoms, giving rise to nuclear energy levels with quantized spin and parity. In an atom, the electrons are subject to the Coulomb force which binds the electrons to the nucleus. In contrast, individual nucleons are attracted to one another through the strong nuclear force, for which scientists are still trying to find a precise and universal description.

The ground state of the nucleus has the lowest excitation energy of this system, and is considered to have an excitation energy of 0 MeV. States with higher energy are referred to as excited states. Like most natural processes, nuclei are drawn towards being in a lower-energy state. This transition from excited states to a lower energy state occurs through a process known as nuclear decay or radioactivity. There are many different types of radioactivity. In order for a nucleus to decay, there must exist some energy level with lower total energy, either in the same nucleus or in another one.  $\gamma$  radiation occurs when an excited nucleus de-excites to a lower-energy state of the same nucleus by emitting a  $\gamma$  ray. This is an electromagnetic interaction that results in

lifetimes typically on the order of picoseconds to nanoseconds. Particle radiation occurs when the nucleus emits a  $\beta$  or a more massive particle such as a nucleon, or a composite particle such as a triton or  $\alpha$  particle. Particle decays are a result of the strong interaction and result in states with lifetimes frequently down to the order of  $10^{-20}$  seconds. However, in some cases where the Coulomb barrier is very large, this lifetime can be much longer, from  $\mu\text{s}$  to thousands of years.  $\beta$  radiation is a result of the weak interaction, which results in states with a variety of lifetimes, from milliseconds to many thousands years. [1]

In order for a particle to be radiated, the nucleus must be unbound with respect to that particle. That means that the binding energy of the nucleus is low enough that it is energetically allowable to emit that particle. The decay threshold accounts for the differences in binding energy between the initial nucleus and the final one(s). Note that a state may have many different decay modes energetically available; just because it is above a decay threshold does not mean that it will decay in that mode. A quantity called the branching ratio tells us what fraction of all decays proceed by a given channel. [2]

The fundamental law of radioactive decay,

$$\dot{N} = \lambda N, \quad (1.1)$$

gives the “decay constant” ( $\lambda$ ) in terms of the number of decays per unit time. This decay constant is related to the lifetime of the nucleus by

$$\tau = \frac{1}{\lambda} \quad (1.2)$$

where the lifetime ( $\tau$ ) indicates how long it takes for  $1/e$  of the nucleus to decay. We can use the Heisenberg uncertainty relation,

$$\tau \Delta E \gtrsim \hbar, \quad (1.3)$$

which gives us the energy width of the excited state. Note that this is not experimental or statistical uncertainty, but physical property of the state. This width is frequently represented by

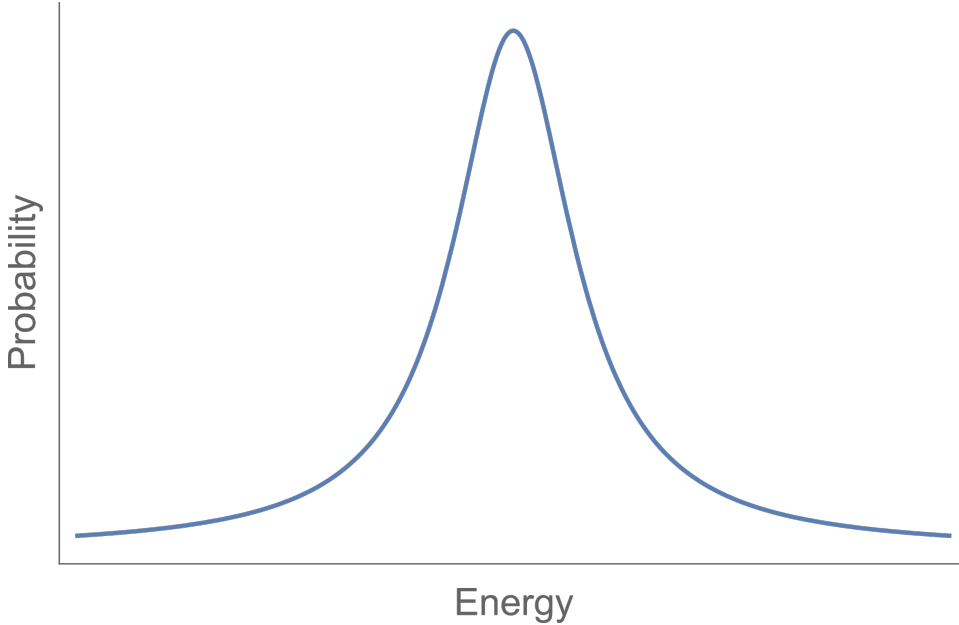


Figure 1.1: **Breit-Wigner Form** Example of the Breit-Wigner distribution for an arbitrary energy and width.

$\Gamma$  and is related to the width of the distribution of observed energies for a particular state. This distribution, which is described by the Breit-Wigner form in simple cases, is given by,

$$f(E) \propto \frac{A}{(E - E_0)^2 + \frac{1}{4}\Gamma^2}, \quad (1.4)$$

where  $A$  is the amplitude of the peak,  $E_0$  is the central energy, and  $E$  is the measured energy. An example of this kind of function is given in Fig. 1.1. In a state where there are several possible decay channels, each channel has its specific width, known as the “partial width” ( $\Gamma_i$ ). These partial widths follow a simple sum rule,

$$\Gamma = \sum \Gamma_i, \quad (1.5)$$

that relates these partial widths to the total width.[2]

Finding the locations, widths, and decay patterns of excited states is a primary effort in nuclear physics, and falls under the heading of nuclear structure. Much work has already been put in to determining the structure of  $^{14}\text{C}$ . The currently known energy levels and decays are shown in Figs. 1.2 and 1.3. These energy levels were primarily determined by scattering experiments

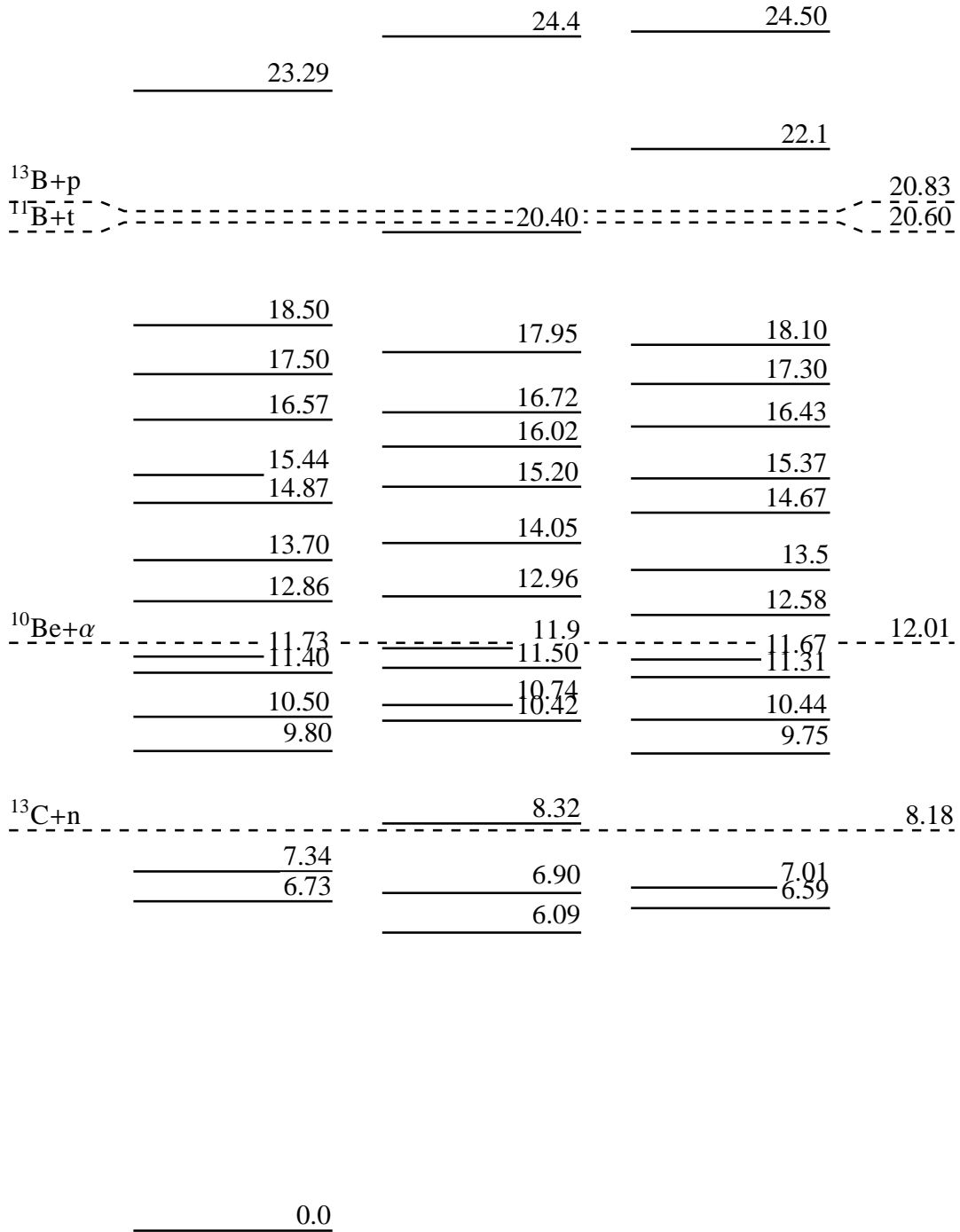


Figure 1.2: **Known Energy Levels of  $^{14}\text{C}$**  The solid lines in this figure are energy levels as compiled by the National Nuclear Data Center [3]. The dashed lines correspond to the decay threshold for different particles. The most relevant part for this work is the  $^{10}\text{Be} + \alpha$  line.

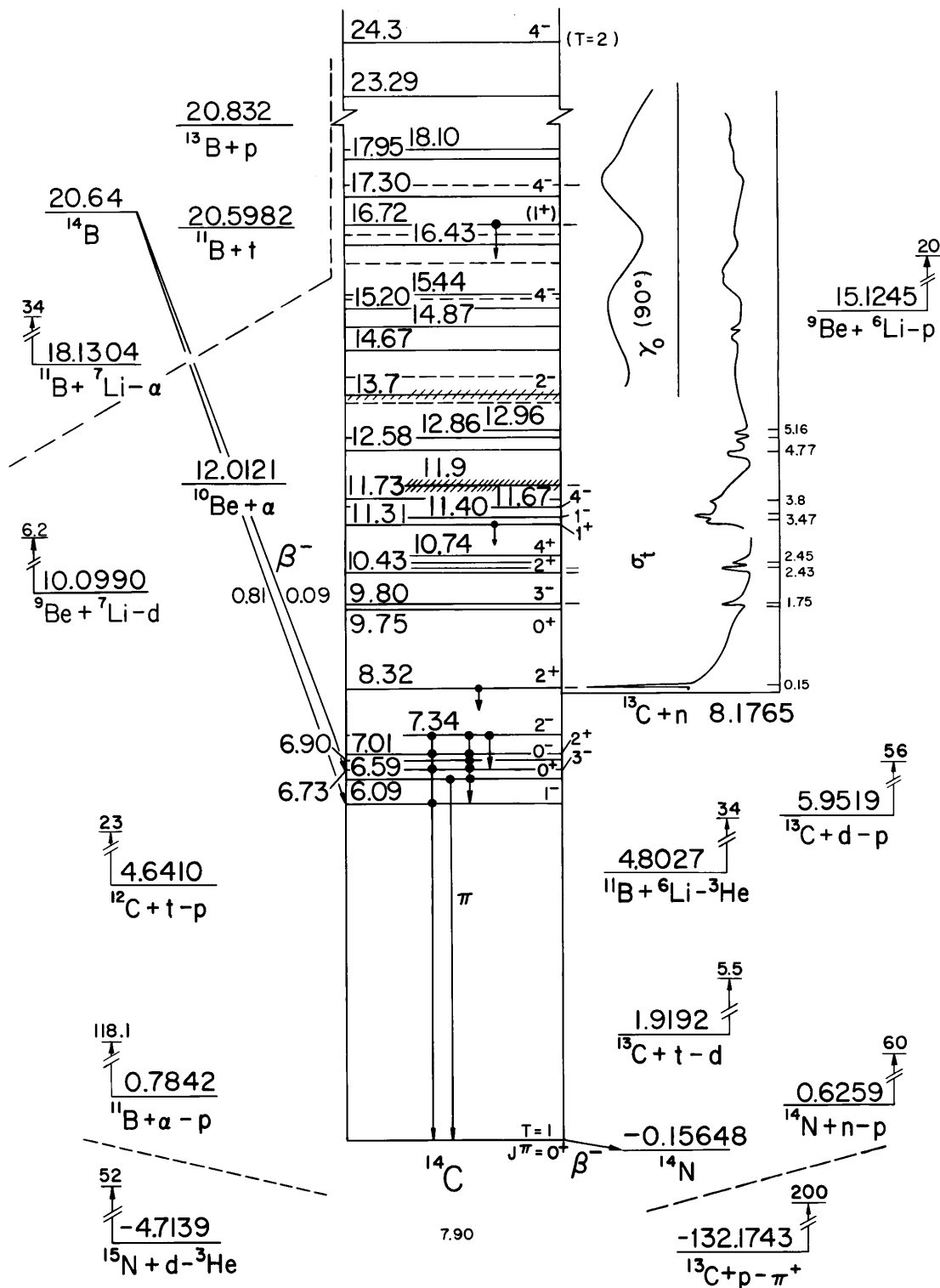


Figure 1.3: **Levels and Decays of  $^{14}\text{C}$**  Image showing energy levels and decay properties of  $^{14}\text{C}$ . Image from the TUNL Nuclear Data Evaluation Project. [4]

that leave a  $^{14}\text{C}$  nucleus in an excited state. If particle decay is experimentally forbidden, the state emits a gamma ray. That gamma ray may correspond to the excited state decaying into either the ground state or another excited state. Using quantum mechanical selection rules and careful analysis, many states can be determined both above and below particle emission thresholds. [3]

The ground state of  $^{14}\text{C}$  is especially interesting to scientists. It is radioactive via  $\beta^-$  decay, with an anomalously long half-life of 5,730 years. This long lifetime makes it useful in radiocarbon dating of biological samples. For nuclear physicists, the interest lies in finding out *why* this lifetime is so long. Recently, an *ab initio* calculation was performed that revealed that this lifetime is a result of unexpectedly strong cancellation between the nuclear three-body force and the nucleon-nucleon interaction. [5] This calculation is described in more detail in Chapter 2.

The present thesis considers the structure of  $^{14}\text{C}$  but from the perspective of clustering and using a unique experimental technique.

## 1.2 Clustering

Clustering theory considers the nucleus as being made up of clusters of nucleons,  $\alpha$  particles, instead of individual protons and neutrons. The  $\alpha$  particle is very strongly bound, and hence can conserve some of its characteristics even inside of a larger nucleus. This approach has been in existence since the early days of nuclear physics [6] and rose to prominence more recently with the Hoyle state of  $^{12}\text{C}$ . [7]

The mean field of the nuclear interaction, which results in more spherical shapes, and the tendency for nuclei to cluster can be viewed as being in competition. In the mean field description, each particle moves freely, while clustering image has the  $\alpha$  exist, necessarily removing some degrees of freedom. [8] The illustration of this competition is found in the so-called Ikeda diagram [9]. In this image, cluster states exist at high excitation energies, at or above the alpha-decay threshold. A modern depiction of the Ikeda diagram is shown in Fig. 1.4. Many non-cluster states also exist in this energy range. One author [10] has described this phenomenon as

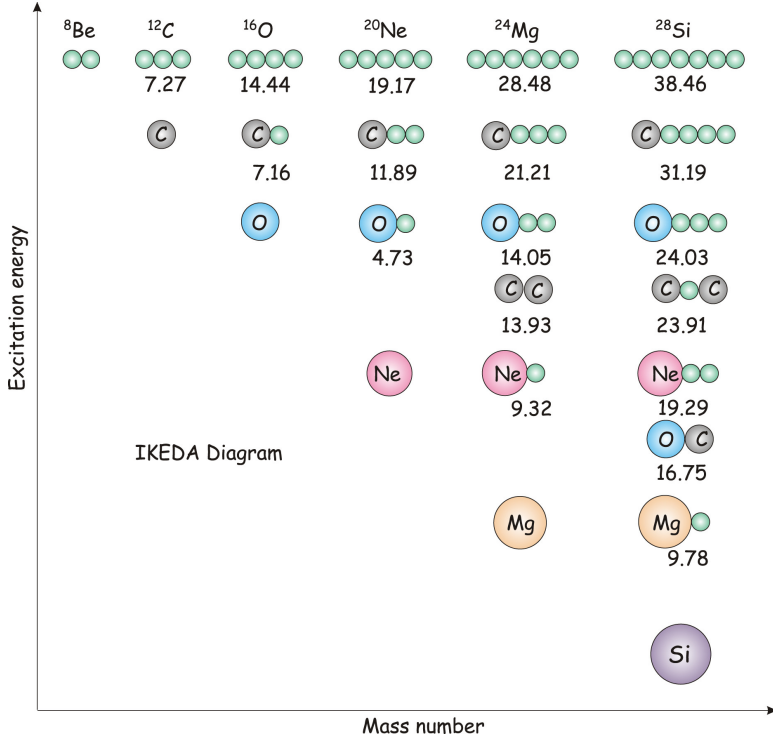


Figure 1.4: **Ikeda Diagram** Diagram first proposed by [9] showing that cluster structures may occur at high excitation energies near the alpha-decay threshold for  $N = Z$  cluster nuclei. For higher-mass nuclei, it can be seen that the  $\alpha$ s clusterize with increasing number as the excitation energy increases. Image from [11].

“cluster states immersed into a bath of non-cluster states.”

$^{14}\text{C}$ , the nucleus of interest in the present work, has more neutrons than protons, so it cannot be broken down into constituent  $\alpha$  particles. Instead, in a clustering view, it consists of three  $\alpha$  particles with two valence neutrons. From the beginning of cluster studies [6], it has been proposed that these non- $\alpha$  nuclei form clusters by making “nuclear molecules” in analogy to more familiar atomic molecules. In this case, the  $\alpha$  particles covalently exchange the valence neutrons compared to atoms in molecules sharing valence electrons.[8]

Research into cluster structures focuses in two areas: their structure and their decay properties. Structure in this case refers to how the clusters are arranged. Examples of these arrangements are shown in Fig. 1.5. Structures include: linear chains, acute triangles, bent arms with obtuse angles, or simple condensates without a well-defined structure.

Because their structure is dominated by  $\alpha$  particles, cluster states typically decay by alpha-

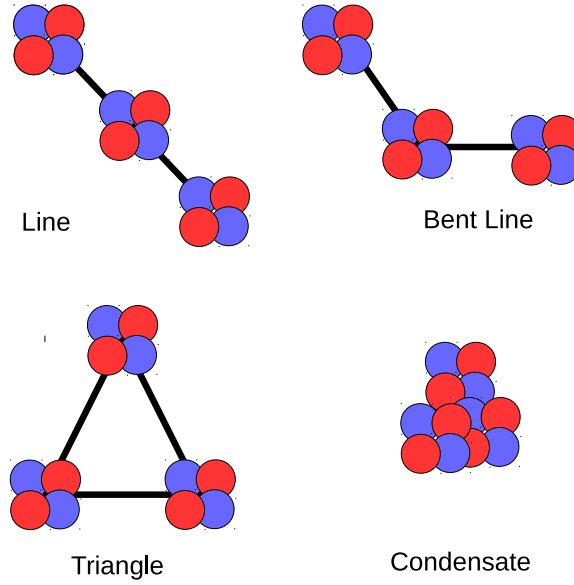


Figure 1.5: **Example Arrangements of Clusters in  $^{12}\text{C}$**  Cartoon showing the different ways that three clusters could arrange themselves in a nucleus. Lines, bent lines, triangles, and condensates are all possibilities. These shapes and many others are discussed in [8].

emission. In a state with multiple clusters, a question can be asked about whether the  $\alpha$  particles are emitted one at a time or simultaneously. These options are referred to as “sequential” and “democratic” decay, respectively. The frequency of the different modes can give insight about the structure of the nucleus. A recent experiment [12] used the  $7\text{-}\alpha$  decay of  $^{28}\text{Si}$  to suggest toroidal resonances.

### 1.3 Previous Work

#### 1.3.1 Hoyle State

The Hoyle state was predicted by Fred Hoyle in 1954. [7] It is an excited, spin-0 state of  $^{12}\text{C}$ . It is required to exist in order to understand the nucleosynthesis of carbon in red giant stars, the amount of carbon in the solar system, and thus the existence of life as we know it.

The structure of the Hoyle state has been proposed to be a bent-arm shape via *ab initio* calculations [13], but this has yet to be confirmed experimentally. Many experiments have tried to access this structure by studying the decay properties of the state [14, 15]. Democratic de-

cay is significantly less likely than sequential decay due to the difficulty of several alpha particles simultaneous tunneling through the Coulomb barrier. The experimental upper limit on the democratic decay of the state is 0.043% of all decays. [15] The theoretical estimation of the democratic contribution [16] is currently at least a factor of 10 below that of experiment.

### 1.3.2 Carbon-14

Unlike the Hoyle state,  $^{14}\text{C}$  is not an  $\alpha$ -nucleus. It consists of three  $\alpha$  particles plus two valence neutrons. Using this nucleus, we can study the evolution of cluster structure and decay patterns in more neutron-rich nuclei.

The current work builds most directly off the work of Fritsch, *et al.* [17]. That experiment studied elastic scattering of  $^{10}\text{Be}$  on  $\alpha$  in a time projection chamber. Several negative parity states were found as well as a  $2^+$  and  $4^+$  state which were proposed to be part of a linear chain rotational band. These states were at excitation energies of 3.0 MeV and 7.0 MeV above the  $^{10}\text{Be} + \alpha$  threshold, respectively. This suggests that there should be a  $0^+$  state to accompany these two states. The evidence for this state would more firmly establish the characteristics of the rotational band.

The work of Freer, *et al.* [18] was, again,  $^{10}\text{Be}$  on  $\alpha$  scattering with the detection system consisting of a series of silicon detectors arranged as shown in Fig. 1.6. This experiment found the  $4^+$  and  $6^+$  at 6.21 and 8.79 MeV which have since been assigned to the same rotational band.

At the time when the experiments in this work were completed, there was a clear motivation for an experiment aimed explicitly at finding the  $0^+$  as the band head of the rotational band. An additional motivation was the fact that no experiment had been done that studied the three-body decay of  $^{14}\text{C}$ . These were the primary goals of the experiments in this work. Based on the energy of the  $2^+$  and  $4^+$  states, the energy of the  $0^+$  can be predicted. In a rotational band, the energy of the state is proportional to  $J(J+1)$ . Thus, based on the Fritsch data [17], the energy of the  $0^+$  should be at 1.2 MeV, while based on the Freer data [18] it should be at 3.87 MeV. A linear fit with all four points places the  $0^+$  at 2.8 MeV.

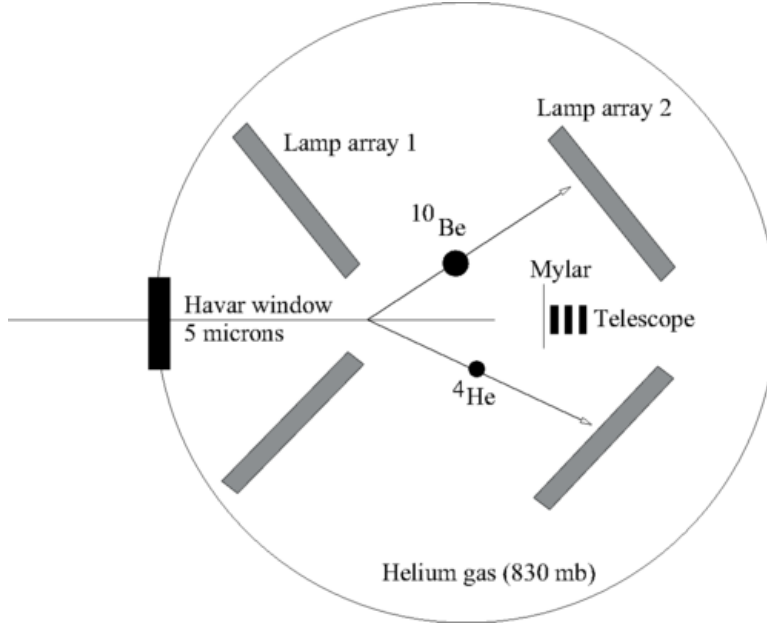
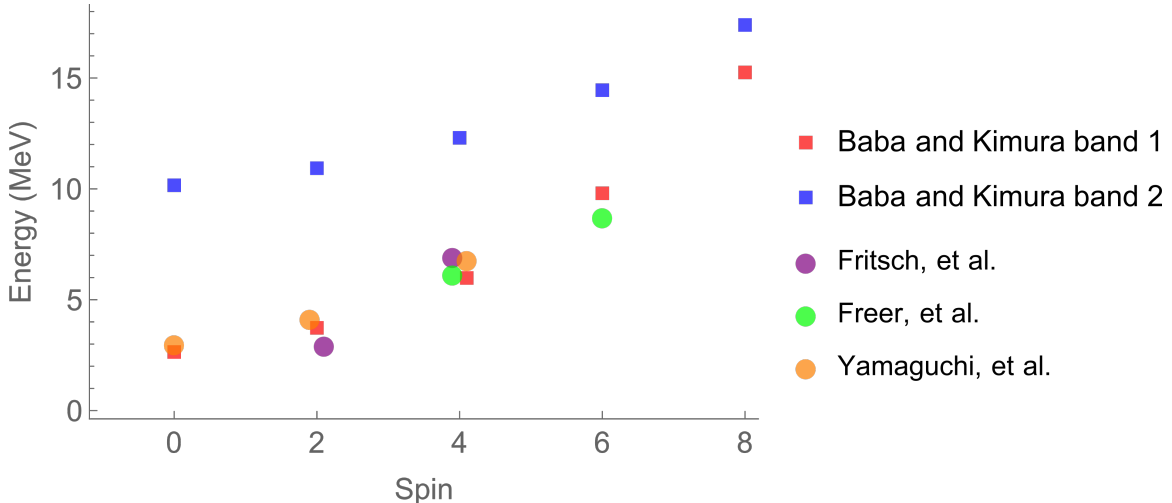


Figure 1.6: **Experimental Setup of [18]** All detectors shown are silicon detectors arranged in either a “telescope” or “lampshade” shape. The  $^{10}\text{Be}$  beam was scattered off  $^4\text{He}$  gas. Figure from [18].

The experimental landscape has changed somewhat since that time. Yamaguchi, *et al.* [19] tentatively located the looked-for  $0^+$  state (at 3.06 MeV) in addition to re-measuring the same  $2^+$  and  $4^+$ . This experiment was another inverse-kinematic scattering experiment, with outgoing particles detected at  $0^\circ$  and  $9^\circ$  from the beam axis. A summary of the experimentally known linear chain rotational states (as well as some theory more deeply discussed in Chapter 2) is shown in Fig. 1.7.

The detailed decay properties are still unknown, and nothing has been experimentally measured of the second predicted rotational band. These are both accessible from the experiments performed in this work.

Many other non-linear chain states have also been predicted or measured in the experimental energy range. Von Oertzen, *et al.* [21] measured states using a variety of different transfer reactions and a magnetic spectrograph. That work measured many states, most of which were below the  $^{10}\text{Be} + \alpha$  threshold. Of those above threshold, some were tentatively assigned to linear chain bands and triangular bands, and several other high-energy states in the range of the



**Figure 1.7: Summary of Linear Chain Cluster States** Linear chain cluster states known so far in two different rotational bands. The round, colored points are experimentally measured cluster states, while the boxes represent the theory discussed in Chapter 2. The  $y$ -axis is in terms of energy above the  ${}^{10}\text{Be} + \alpha$  threshold. The work in this thesis covers from energy 0 to 11 in these units. The  $x$ -axis is jittered slightly to aid in seeing all points – all measurements are at whole-number spin values. Figure adapted from [20].

present work were ambiguously attributed. The shapes that they considered for known structures are shown in Fig. 1.8

The previously-cited works of Fritsch [17], Freer [18], and Yamaguchi [19] also measure other states. A full account of experimentally-known states is shown in Table 1.1.



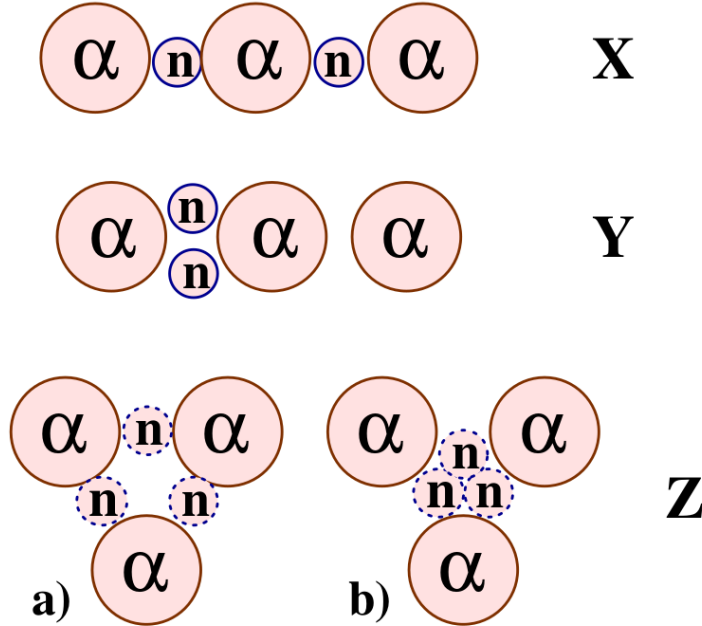


**Figure 1.8: Linear and Triangular Clusters** The four shapes identified by Von Oertzen, *et al.* [21] in  $^{14}\text{C}$ . Both X and Y are linear chain structures. The figure labeled X is rotationally symmetric and has positive parity, while Y is asymmetric and has a parity doublet. The figures labeled Z are triangular shapes with the two neutrons evenly distributed over the three alpha particles, represented as three neutrons with dashed borders. Z(a) has a minimum of neutrons at the center, making the spin-parity  $3^-$ , while Z(b) has a maximum at the center meaning the spin-parity is  $0^+$ . Figure from [21].

Fritsch, <i>et al.</i> [17]		Freer, <i>et al.</i> [18]		Yamaguchi, <i>et al.</i> [19]		Von Oertzen, <i>et al.</i> [21]	
Energy (MeV)	$J^\pi$	Energy (MeV)	$J^\pi$	Energy (MeV)	$J^\pi$	Energy (MeV)	$J^\pi$
3.0	$2^+$	5.29	$3^-$	2.20	$(2^+)$	0.47	$3^-$
4.7	$3^-$	5.98	$2^+$	2.49	$1^-$	2.66	$6^+$
5.6	$5^-$	6.21	$4^+$	3.06	$0^+$	2.86	$5^-$
6.5	$(7^-)$	6.82	$5^-$	4.21	$2^+$	3.18	$5^-$
7.0	$4^+$	7.68	$5^-$	4.36	$(4^+)$	4.42	$6^+$
7.9	$5^-$	8.79	$6^+$	4.92	$(2^+)$	6.03	$(7^-)$
8.7	$5^-$			5.24	$(1^-)$		
				6.01	$(3^-)$		
				6.62	$5^-$		
				6.86	$4^+$		

**Table 1.1: Experimentally Known States** States within experimental energy range of the present work that have been measured by four different experiments. Energy and spin/parity are given for each state measured. Energy is given in terms of energy above the  $^{10}\text{Be} + \alpha$  threshold. The spins and parities are those reported in the cited work.

## CHAPTER 2

### THEORY

Many theoretical approaches combine to aid in the interpretation of the data gathered in this experiment. The two most relevant for the analysis of two body decays are Antisymmetrized Molecular Dynamics for structure and R-Matrix Theory for reaction properties. Additional theories will be discussed in this chapter to bring together a full theoretical picture.

#### **2.1 Antisymmetrized Molecular Dynamics**

The theory that is most relevant to this work is Antisymmetrized Molecular Dynamics, or AMD. [22] AMD predicts molecule-like structures in the nucleus, similarly to how the shell model predicts atom-like structures.

In AMD as formulated by Suhara and Kanada-En'yo, the basic wavefunction of an  $A$ -nucleon system is given as

$$|\Phi\rangle = \frac{1}{\sqrt{A!}} \det\{|\varphi_1\rangle, \dots, |\varphi_A\rangle\} \quad (2.1)$$

which is a Slater determinant of  $|\varphi_i\rangle$ s, which have a spatial Gaussian part plus spin and isospin, e.g.

$$|\varphi_i\rangle = |\phi_i\rangle |\chi_i\rangle |\tau_i\rangle, \quad (2.2)$$

$$\langle \mathbf{r} | \phi_i \rangle = \left( \frac{2\nu}{\pi} \right)^{\frac{3}{4}} \exp \left[ -\nu \left( \mathbf{r} - \frac{\mathbf{Z}_i}{\sqrt{\nu}} \right)^2 + \frac{1}{2} \mathbf{Z}_i^2 \right], \quad (2.3)$$

$$|\chi_i\rangle = \xi_{i\uparrow} |\uparrow\rangle + \xi_{i\downarrow} |\downarrow\rangle, \quad (2.4)$$

and

$$|\tau_i\rangle = |p\rangle \text{ or } |n\rangle. \quad (2.5)$$

In a given  $|\Phi\rangle$ , the wavepacket is centered at  $\mathbf{Z}$  with width  $v$ . The  $\xi$  are the probability amplitudes of each spin orientation. All of these are variational parameters that are determined by energy optimization.

Next, the wavefunctions are projected on to parity eigenstates,

$$|\Phi^\pm\rangle = \hat{P}^\pm |\Phi\rangle \quad (2.6)$$

where

$$\hat{P}^\pm \equiv \frac{1 \pm \hat{P}}{2} \quad (2.7)$$

for the parity operator  $\hat{P}$ .

The calculation used to predict  $^{14}\text{C}$  states was  $\beta-\gamma$  constrained AMD meaning that the variation was carried out with variationally constrained  $\beta$  and  $\gamma$  which are related to the quadrupole deformation of the nucleus and defined in the following way:

$$\beta \cos \gamma \equiv \frac{\sqrt{5\pi}}{3} \frac{2 \langle \hat{z}^2 \rangle - \langle \hat{x}^2 \rangle - \langle \hat{y}^2 \rangle}{R^2}, \quad (2.8)$$

$$\beta \sin \gamma \equiv \sqrt{\frac{5\pi}{3}} \frac{\langle \hat{x}^2 \rangle - \langle \hat{y}^2 \rangle}{R^2}, \quad (2.9)$$

and

$$R^2 \equiv \frac{5}{3} \left( \langle \hat{x}^2 \rangle + \langle \hat{y}^2 \rangle + \langle \hat{z}^2 \rangle \right), \quad (2.10)$$

where the principal axes,  $\hat{x}$ ,  $\hat{y}$ , and  $\hat{z}$ , are chosen such that  $\langle \hat{y}^2 \rangle \leq \langle \hat{x}^2 \rangle \leq \langle \hat{z}^2 \rangle$  and  $\langle \hat{x} \hat{y} \rangle = \langle \hat{y} \hat{z} \rangle = \langle \hat{z} \hat{x} \rangle = 0$ .

The constraint potential used was

$$V_{\text{const}} \equiv \eta_1 \left[ (\beta \cos \gamma - \beta_0 \cos \gamma_0)^2 + (\beta \sin \gamma - \beta_0 \sin \gamma_0)^2 \right] + \eta_2 \left[ \left( \frac{\langle \hat{x} \hat{y} \rangle}{R^2} \right)^2 + \left( \frac{\langle \hat{y} \hat{z} \rangle}{R^2} \right)^2 + \left( \frac{\langle \hat{z} \hat{x} \rangle}{R^2} \right)^2 \right] \quad (2.11)$$

for parameters  $(\beta_0, \gamma_0)$  constrained such that  $\eta_1$  and  $\eta_2$  are sufficiently large. This makes the total energy to be minimized

$$E = \frac{\langle \Phi^\pm | \hat{H} | \Phi^\pm \rangle}{\langle \Phi^\pm | \Phi^\pm \rangle} + V_{\text{const.}} \quad (2.12)$$

The Hamiltonian used has a kinetic term with an effective two body interaction given by the Volkov No. 2 interaction, the spin-orbit interaction, and the Coulomb interaction. (See [22] for details.)

Once the energy has been minimized, the resultant wavefunction is  $|\Phi^\pm(\beta_0, \gamma_0)\rangle$  for each set of parameters. Then, the wavefunctions are projected on to the total angular momentum eigenstates using the angular momentum projection operator,

$$\hat{P}_{MK}^J \equiv \frac{2J+1}{8\pi^2} \int D_{MK}^{J*}(\Omega) \hat{R}(\Omega) d\Omega \quad (2.13)$$

using Wigner's  $D$  function and the rotation operator  $\hat{R}$ .

This projection is critical for the results of this calculation. For an example see Fig. 2.1. They show that the minimum of the energy surface for all positive parity states is at  $(\beta \cos \gamma, \beta \sin \gamma) = (0, 0)$ , which corresponds to a shell-model-like sphere, but after projection the minimum for  $0^+$  is at  $(\beta \cos \gamma, \beta \sin \gamma) = (0.23, 0.04)$  which is triaxially deformed. This holds similarly for negative parity states shown in Fig. 2.2. The minimum point for the combined wavefunction is  $(\beta \cos \gamma, \beta \sin \gamma) = (0.04, 0.08)$  which is nearly spherical while the minimum point for a  $3^-$  state is at  $(\beta \cos \gamma, \beta \sin \gamma) = (0.2, 0.09)$  which has a triaxial deformation.

The final wavefunctions are superpositions of these projected wavefunctions via

$$|\Phi_n^\pm\rangle \sum_K \sum_i f_n(\beta_i, \gamma_i, K) \hat{P}_{MK}^J |\Phi^\pm(\beta_0, \gamma_0)\rangle \quad (2.14)$$

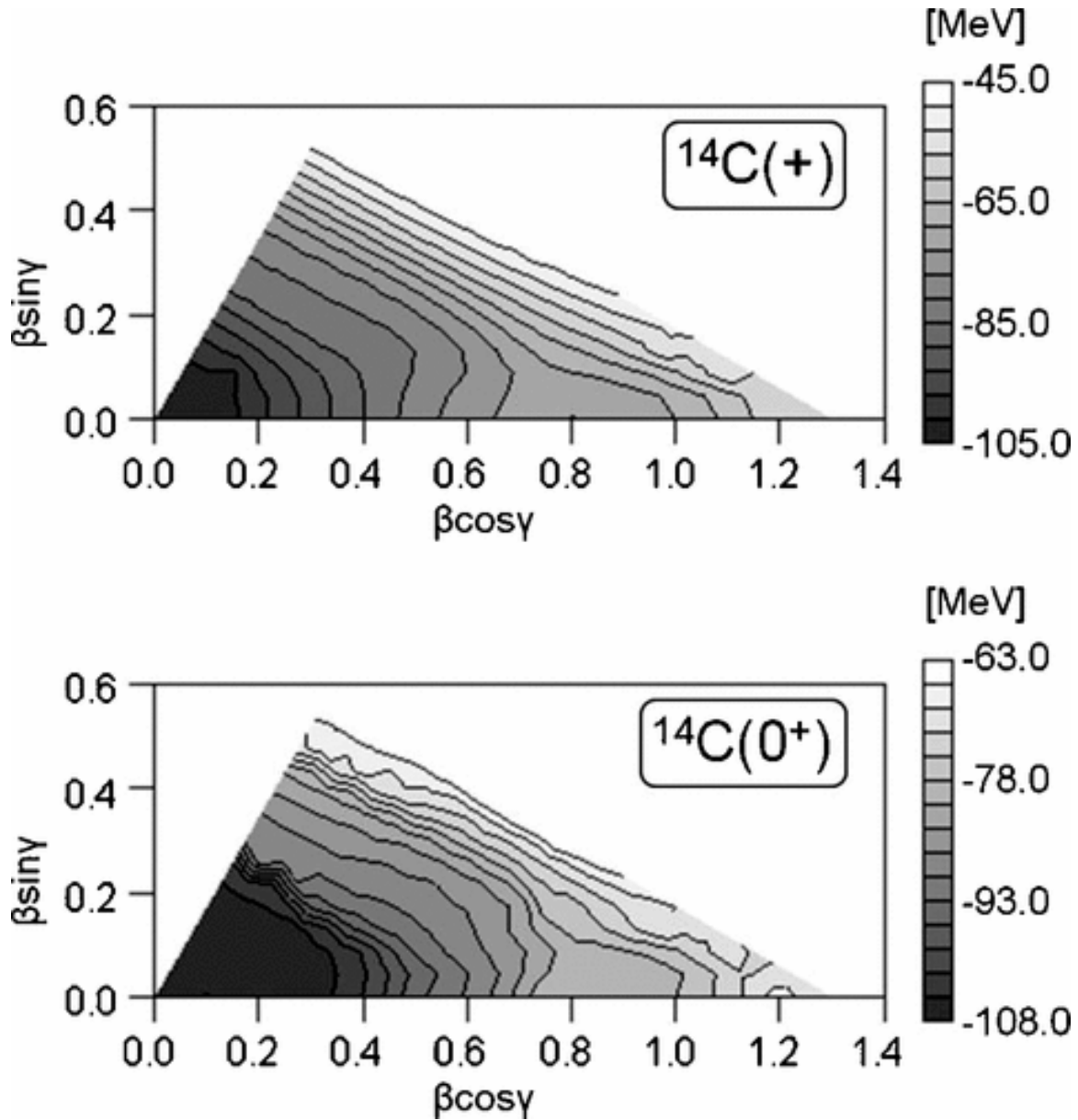


Figure 2.1: **Positive Parity Energy Surfaces** Plots showing the energy as a function of  $\beta$  and  $\gamma$  for (in the top panel) the positive-parity wavefunctions before projection, and the  $0^+$  wavefunctions. Figure from [22].

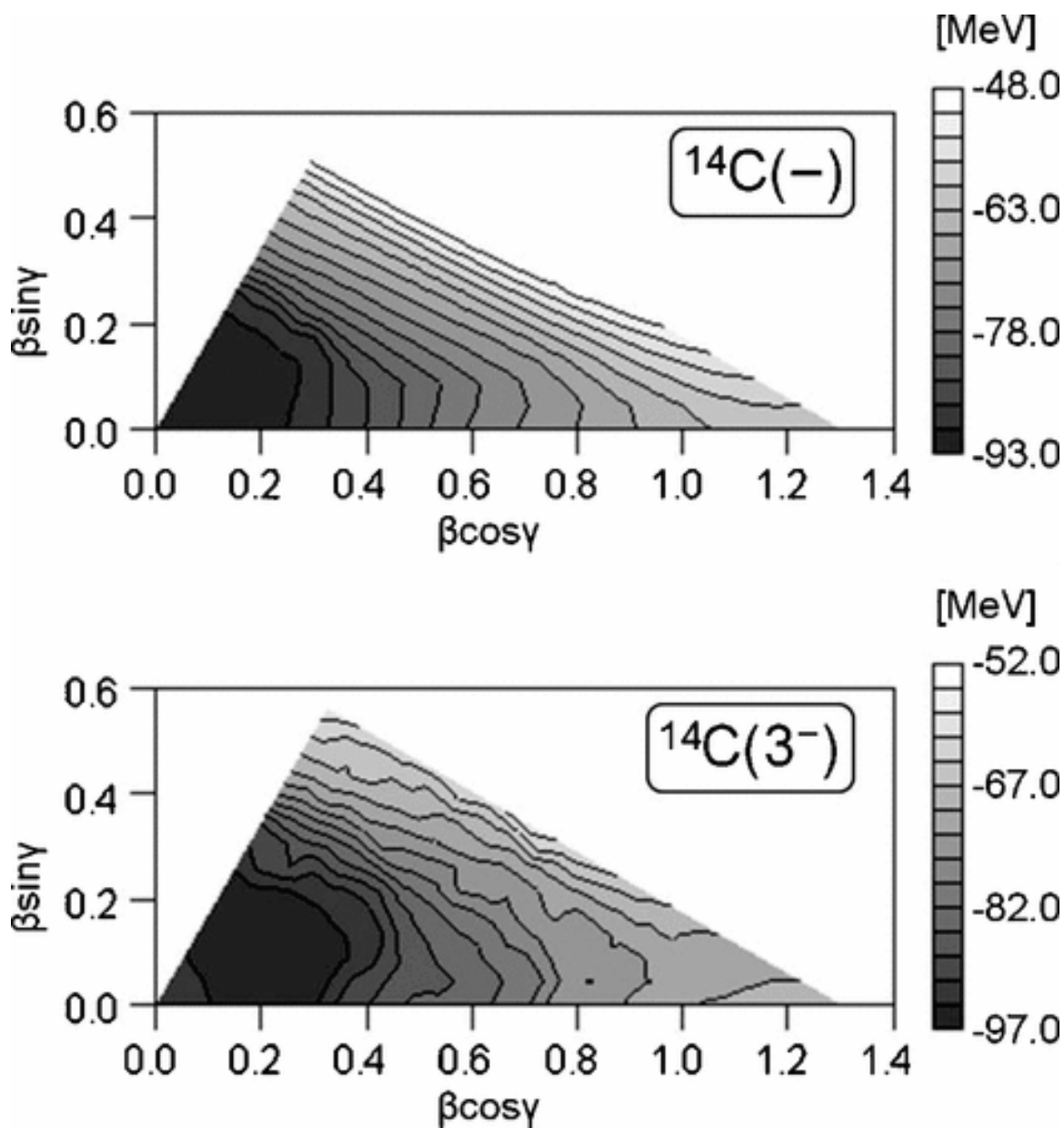


Figure 2.2: **Negative Parity Energy Surfaces** Plots showing the energy as a function of  $\beta$  and  $\gamma$  for (in the top panel) the negative-parity wavefunctions before projection, and the  $3^-$  wavefunctions. Figure from [22].

(a)-(f)	Positive Parity		Negative Parity	
	$\beta \cos \gamma$	$\beta \sin \gamma$	$\beta \cos \gamma$	$\beta \sin \gamma$
(a)	0.00	0.00	0.08	0.04
(b)	0.23	0.04	0.20	0.09
(c)	0.45	0.17	0.25	0.35
(d)	0.25	0.35	0.60	0.17
(e)	0.78	0.22	0.93	0.04
(f)	0.93	0.04		

Table 2.1:  **$\beta$  and  $\gamma$  Values** The letters in the first column correspond to the key letters in Figs. 2.3 and 2.4. These  $\beta$  and  $\gamma$  values correspond to the different shapes as shown.

where the  $f_n$  are solutions to the Hill-Wheeler equation, which is given by [22] as

$$\delta \left( \langle \Phi^{J\pm} | \hat{H} | \Phi^{J\pm} \rangle - E_n \langle \Phi^{J\pm} | \Phi^{J\pm} \rangle \right) = 0. \quad (2.15)$$

Historically [23], this equation was rendered as an integral equation that makes the  $f$  more apparent

$$\int_0^\infty [H_l(s', s) - EN_l(s', s)] f_l s^2 ds = 0 \quad (2.16)$$

where  $H_l(s', s)$  is the matrix element of the Hamiltonian between two state  $\Phi_l(s')$  and  $\Phi_l(s)$  with different parameters,  $s'$  and  $s$ , and  $N_l$  is the overlap matrix between these same two states.

This theory does not presume the existence of clusters. In fact, part of the utility of the theory is that it reveals both shell-type and cluster-type states.

The particle density found for the different wavefunctions is shown in Figs. 2.3 and 2.4 with the  $\beta$  and  $\gamma$  values shown in Table 2.1. These wavefunctions have a variety of forms, from shell-model-like spheres, to clustered triangles and lines. Specific  $J^\pi$  values have energies shown in Fig. 2.5.

This was the first paper to predict a linear chain structure in  $^{14}\text{C}$ . This structure was then suggested experimentally by [17] and others. This lead to further AMD calculations [20] to understand the linear chain predictions and data.

These more recent calculations by Baba and Kimura [20] use the Gogny D1S interaction as the effective two-body Hamiltonian, but otherwise the initial method is very similar to that of

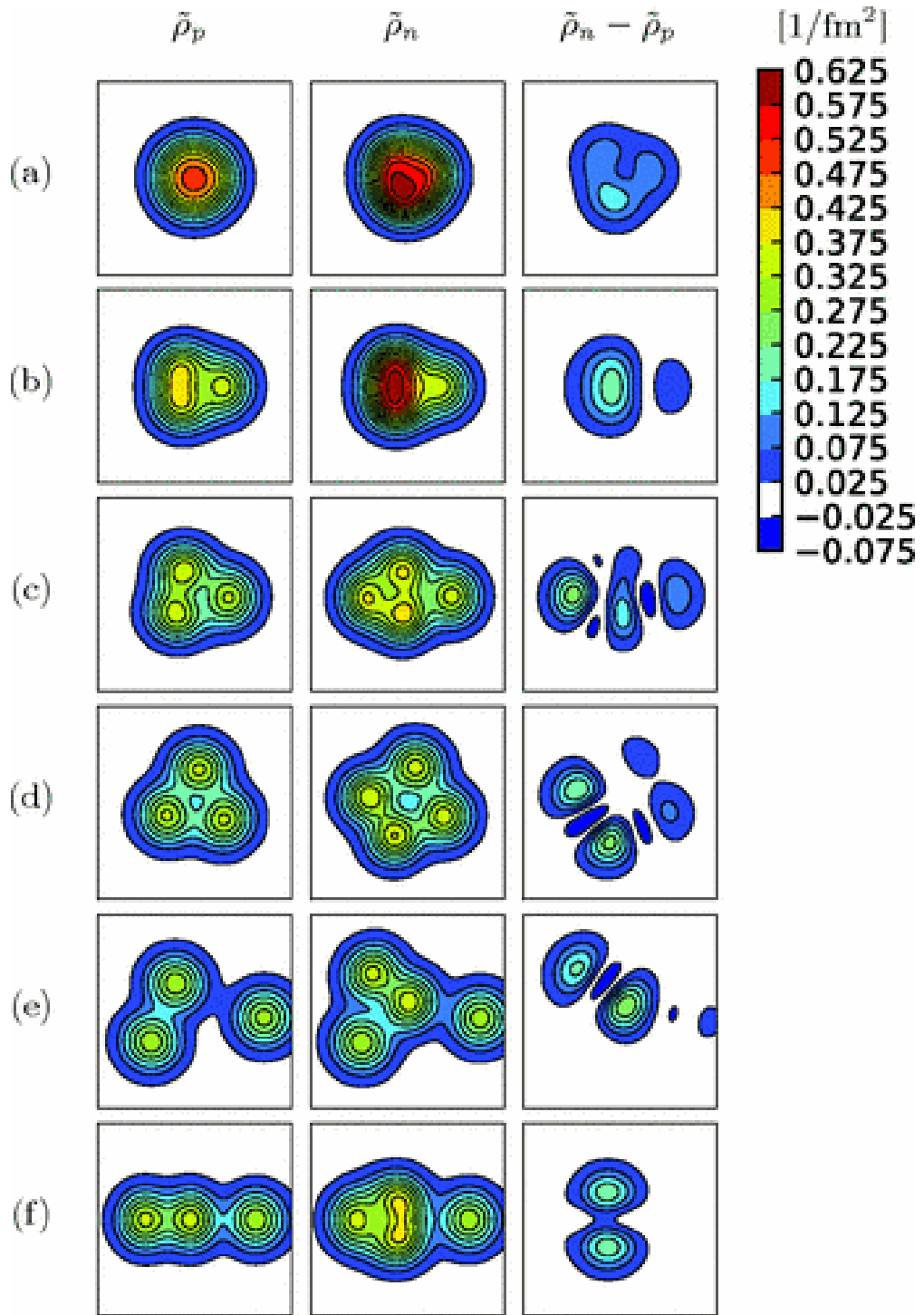


**Figure 2.3: Positive Parity AMD Wavefunctions for  $^{14}\text{C}$**  Each grouping of three pictures (labeled a-f) has a different value of  $\beta$  and  $\gamma$  as shown in Table 2.1. The first column of every grouping is the proton density, the second column is the neutron density, and the third is the difference between them — where the excess neutrons lie. Each box is 10 fm on each side. Images from [22].

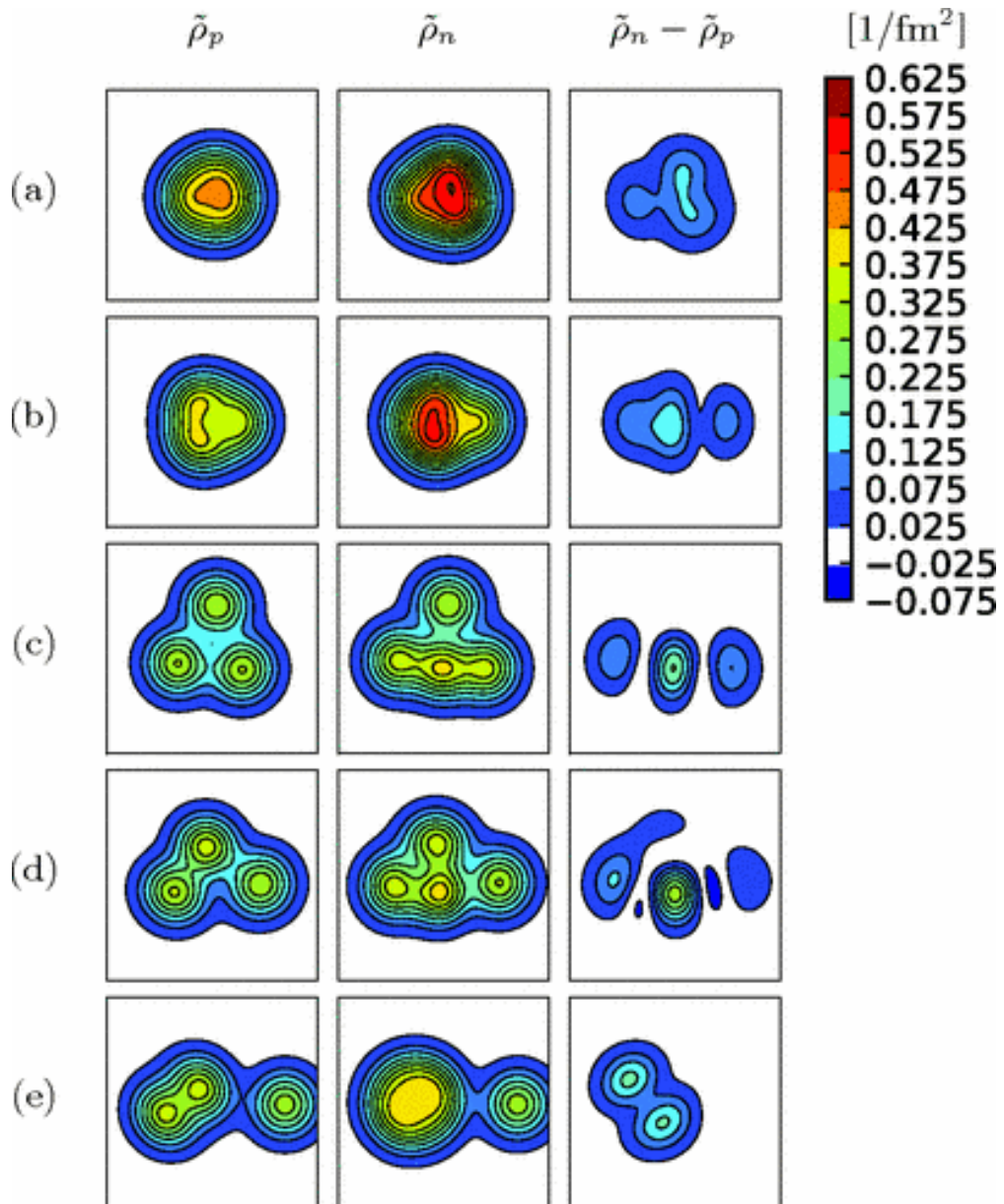


**Figure 2.4: Negative Parity AMD Wavefunctions for  $^{14}\text{C}$**  Each grouping of three pictures (a-e) has a different value of  $\beta$  and  $\gamma$  as shown in Table 2.1. The first column of every grouping is the proton density, the second column is the neutron density, and the third is the difference between them — where the excess neutrons lie. Each box is 10 fm on each side. Images from [22].

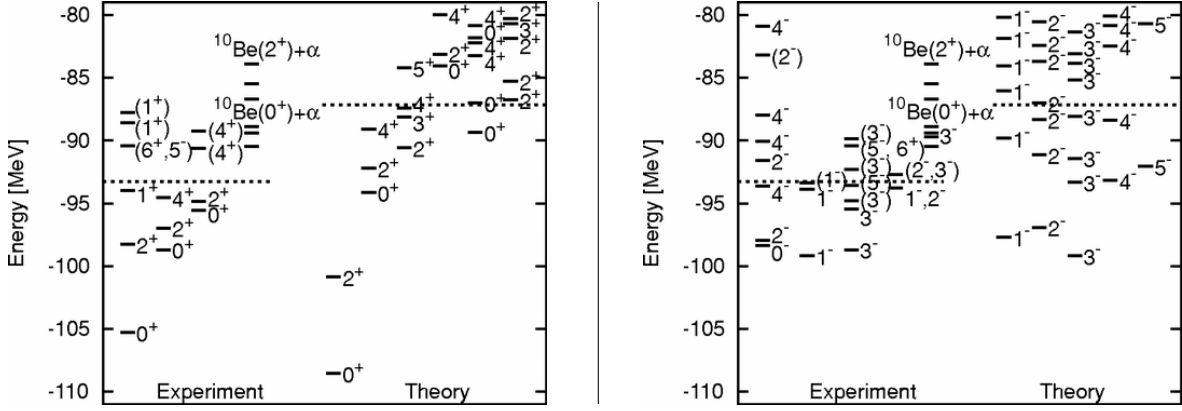


Figure 2.5: **AMD Energy Levels** The experimental and theoretical energy levels where the theory levels are those calculated by [22]. The left and right images show the positive and negative parity states, respectively. Note the energy scale is different than most in this thesis; here it is the total binding energy of the nucleus, whereas in most of this thesis, the energy scale is shifted to have zero at the  $^{10}\text{Be} + \alpha$  threshold. Figure from [22].

Suhara and Kanada-En'yo [22]. This calculation then proceeds to calculate the widths of two different decays:  $\alpha + ^{10}\text{Be}$  and  $^6\text{He} + ^8\text{Be}$ . In this section, the intrinsic wavefunction for the Be cluster is found from a single AMD Slater determinant. The intrinsic wavefunction for the He clusters is given by harmonic oscillator states represented as a sum of infinitesimally shifted Gaussian wavepackets. These clusters are separated by a variational inter-cluster distance.

They obtain clear linear chain structures of  $\alpha$  particles with valence neutrons. Two different rotational band structures are determined in this method, the  $\sigma$ -bond and the  $\pi$ -bond bands. The difference between these is best seen in Fig. 2.6. In the  $\pi$ -bond, there is a more clear  $^{10}\text{Be} + \alpha$  shape, while in the  $\sigma$  bond, the valence neutrons are more evenly distributed over the whole nucleus. As shown,  $\sigma$ -bonded states can only have positive parity, while the  $\pi$ -bond can have either positive or negative parity. This terminology is borrowed from that of covalent chemical bonds.

Based on their calculations, they assign the then-known experimental levels to the  $\pi$ -bond linear chain band, which is the lower energy band shown in Fig. 1.7.

The widths calculated by Baba and Kimura are tabulated in [24]. These widths are the partial widths of the  $\alpha$  decay of  $^{14}\text{C}$  in a specific excited state. This partial decay width  $\gamma$  is related to

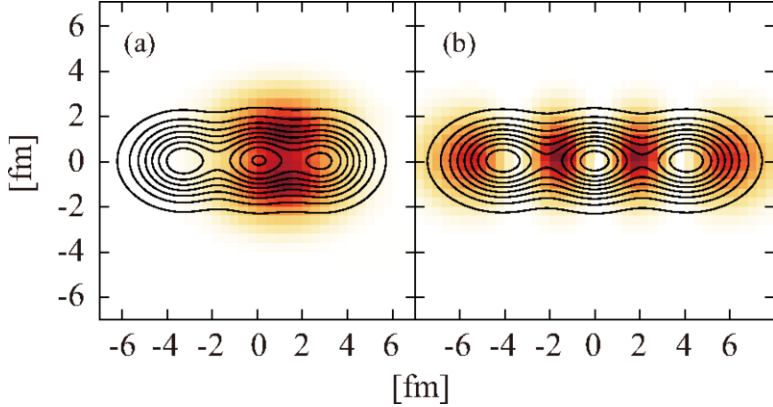


Figure 2.6:  **$\pi$  and  $\sigma$  bonds** (a) is the  $\pi$  bond and (b) is the  $\sigma$  bond. The contours show the proton density distribution, while the color shows single-particle orbit of the most weakly bound neutron. These can be compared with the shapes from Fig. 1.8. Figure from [20].

the width of the excited state  $\Gamma$  by the relation

$$\Gamma = 2P_l(a)\gamma^2 \quad (2.17)$$

where  $P_l$  is the penetration fraction defined as

$$P_l = \frac{ka}{F_l^2(ka) - G_l^2(ka)} \quad (2.18)$$

where  $k$  is related to the reduced mass and Q-value of the decay by

$$k = \sqrt{\frac{2\mu E_Q}{\hbar}} \quad (2.19)$$

and the  $F_l$  and  $G_l$  are the regular and irregular Coulomb functions.

## 2.2 *Ab initio* Calculations



The phrase *ab initio* comes from the Latin meaning “from the beginning”. Calculations that are considered *ab initio* are done based on known nucleon-nucleon interactions. Then the many-body problem is solved exactly using these potentials, instead of assuming an approximate form for the wavefunction. For example, the AMD calculations in the previous section presumed Gaussian wavefunctions, so they are not considered *ab initio*.

The no-core shell model is an example of an *ab initio* theory. In the traditional shell model, the nucleus is presumed to exist in the nuclear mean field given by the Woods-Saxon potential. The particles are non-interacting and occupy single-particle energy levels that separate into “magic number” shell closures similar to electron shells of chemistry. In this model, nucleons occupying states below the highest shell closure are considered a core and states occupying the valence states are allowed to excite to form other states. [25] The shell model requires phenomenological interactions. With the advance of supercomputers and appropriate iteration methods, only considering valence nucleons is no longer strictly required in systems that are sufficiently light. The no-core shell model considers all nucleons as interacting with all other nucleons in the system using two-, three-, and sometimes even four-body interaction terms. These interactions define the Hamiltonian to solve the Schrödinger equation, and are used to find energy the levels.

The calculation [5] done to determine the origin of the anomalous long-lifetime of the ground state of  $^{14}\text{C}$  was a no-core shell model calculation using the two-body interaction alone as well as the combined two- and three-body interactions as defined by chiral perturbation theory. A description of chiral perturbation theory is outside the scope of this thesis. The interaction was calculated to next-to-next-to-next-to leading order (N3LO). With only the two-body force included, the strength of the relevant decay (allowed Gamow-Teller  $\beta$  decay) is too large which causes the lifetime to be under-estimated. By including the three-body force, the strength is reduced and the lifetime obtained is more in line with experimental predictions. The reduction is most evident in the p-shell, where the the reduction of the positive contribution is at least one order of magnitude. However, in higher-lying shells, the negative contribution is also enhanced, as shown in Fig. 2.7. The calculation was performed with two parameter sets which represent a fine-tuning of the calculation. Based on this result, the long lifetime can be attributed to the cancellation between nuclear two-body and three-body force.

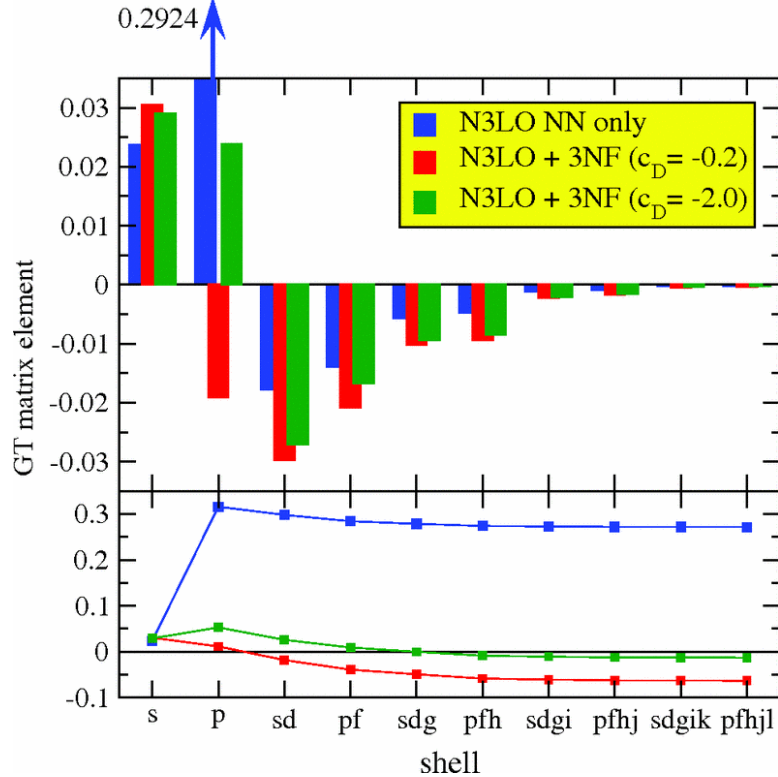


Figure 2.7: **Gamow-Teller Strengths** Calculation with only the two-body interaction, and with a three-body interaction with two different parameter sets (the different  $C_D$  indicated). The upper panel shows the strength inside a given shell while the lower panel gives the running sum. The anomalous long lifetime corresponds to  $|M_{GT}| \approx 2 \times 10^{-3}$ . A small value is only possible with cancellation between the two- and three-body forces. Figure from [5].

## 2.3 R-Matrix Reaction Theory

Nuclear two-body reactions take the form

$$A + B \rightarrow C + D, \quad (2.20)$$

where  $A$  is nucleus incident on nucleus  $B$ , and two nuclei exit the reaction,  $C$  and  $D$ . This same reaction can be represented equivalently as

$$B(A, C)D. \quad (2.21)$$

A special case of this kind of reaction is

$$A + B \rightarrow A + B, \quad (2.22)$$

which is called “elastic scattering”. In this kind of reaction, momentum and kinetic energy are conserved over the reaction. In “inelastic scattering”,



one of the particles leaves in an excited state, represented in the equation by the  $*$ . Since this energy is used to excite the nucleus, kinetic energy is no longer conserved. Relativistically speaking, four-momentum is conserved, as always. In “resonant” scattering, a compound nucleus of  $A + B$  is briefly formed before re-decaying into its component parts. Resonant scattering can be either elastic, by decaying in to  $A + B$ , or inelastic, by decaying in to  $A^* + B$ . Other decay channels could also be available to the resonance, depending on their thresholds energies. The lifetime of the compound state, referred to as a “resonance” is related to the width of the state via the uncertainty relation:

$$\Delta E \Delta t \sim \hbar. \quad (2.24)$$

The theoretical approach to scattering attempts to find the wavefunctions and energies of the particles as they move through the reaction. In the center of mass frame, the wavefunctions and energies of a spin-zero, structure-less nucleus are solutions to the one-dimensional radial Schrödinger equation

$$\left[ -\frac{\hbar^2}{2\mu} \left( \frac{d^2}{dR^2} - \frac{L(L+1)}{R^2} \right) + V(R) - E \right] \chi_L(R) = 0, \quad (2.25)$$

the derivation of which can be found in any elementary quantum mechanics text book.

The  $V$  of this equation is the sum  $V_C + V_n$  where  $V_C$  is the Coulomb force and  $V_n$  nuclear force. The nuclear force does not have a well-defined closed form like gravity or electromagnetism. Interactions between different nuclei are a smeared-out sum of interactions between individual nucleons. This sum is typically represented by a Woods-Saxon shape which is generically given by

$$V_n(r) = -\frac{V_r}{1 + \exp\left(\frac{r-R_r}{a_r}\right)}. \quad (2.26)$$

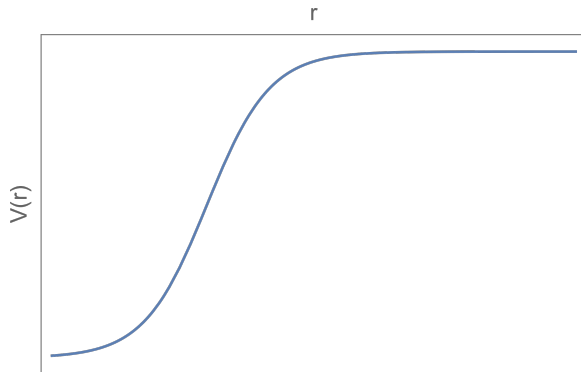


Figure 2.8: **Example Woods-Saxon** Corresponds to Equation 2.27.

This corresponds to an attractive well that looks similar to a flat-bottomed harmonic oscillator (shown in Fig. 2.8) where  $V_r$  is the depth of the well,  $a_r$  is the diffuseness of the well, and  $R_r$  is the size of the nuclear system. In practice, many channels may be open that would need a description by a large number of coupled equations. This is approximated by an imaginary potential that globally accounts for the absorbed flux. This term,

$$W_n(r) = -\frac{i W_r}{1 + \exp\left(\frac{r-R_r}{a_r}\right)}. \quad (2.27)$$

is similar to the  $V_n(r)$  except that  $W_n(r)$  is imaginary. This imaginary term physically corresponds to any nuclear interaction that is not elastic scattering. This includes inelastic scattering and any other reactions that could take place, like fusion or nucleon knockout. There are other terms that must often be added to these models such as surface interaction terms and, for non-spin-zero nuclei, spin-orbit potentials. All of these terms, together, are referred to as an “optical model”. They are referred to this way by analogy with light refracting and being absorbed in a cloudy medium. The optical models are phenomenological models that are fitted to elastic scattering data in order to find values of  $V_r$ ,  $a_r$ ,  $R_r$ , and  $W_r$ . These values vary based on parameters of the experiment like mass and energy of the nuclei involved. Typical values are shown in Table 2.2.[26]

The precise optical models used in analyzing the experiments in this work will be discussed in Chapter 4. For now, their primary importance is to solve Equation 2.25.

Parameter	Typical Value	Units
$V_r$	40-50	MeV
$a_r$	0.6	fm
$R_r$	$1.2A^{1/3}$	fm
$W_r$	10-20	MeV

Table 2.2: **Typical Optical Model Parameters** Typical parameters as compiled by [26].

The R-Matrix method of solving this equation was proposed by Wigner and Eisenbud [27] and popularized by Lane and Thomas [28]. This section follows the pedagogical outline of [26] and [29]. In this method, the solution to this equation is found by a basis expansion of wavefunctions inside of a “channel radius”  $a$  (this  $a$  is unrelated to the  $a_r$  of the optical model). Outside of this channel radius, only the Coulomb force is considered which gives known solutions and can be matched at the channel radius. Let the  $w_i$  represent the elements of the basis set of wavefunctions inside the channel radius for a single-channel reaction. Then, there is a parameter  $\beta$  such that

$$\beta \equiv \left. \frac{w'_i(R)}{w_i(R)} \right|_{R=a} \quad (2.28)$$

and  $w_i(0) = 0$ . That is to say that the logarithmic derivative of the basis is fixed at the channel radius. This fixed logarithmic derivative is what allows us to declare that the  $w_i$  are an orthonormal basis, however it also causes some challenges as shown below.

Because the  $w_i$  form a basis, the  $\chi$  solution can be represented as

$$\chi(R) = \sum_{i=1}^N A_i w_i(R). \quad (2.29)$$

For unknown parameters  $A_i$ . The typical method for solving an equation like this is to set the logarithmic derivative of each side equal to each other to find the  $A_i$ . This is not possible in this case because of the fixed logarithmic derivative. Relatedly, the sum in Equation 2.29 is only convergent on the total wavefunction, not the derivative. The way the  $A_i$  can be determined is by using both a particular  $w_n$  with energy  $\epsilon_n$  in 2.25 as well as  $\chi$  with energy  $E$  in Equation 2.25, multiplying the two equations, and subtracting the opposite product. Recall that wavefunctions

do not generally commute. This operation gives

$$-\frac{\hbar^2}{2\mu} [\chi(a) w'_n(a) - w_n(a) \chi'(a)] + (E - \epsilon_n) A_n = 0. \quad (2.30)$$

Solving for  $A_n$  yields

$$A_n = \frac{\hbar^2}{2\mu} \frac{w_n(a)}{\epsilon_n - E} [\chi'(a) - \beta \chi(a)]. \quad (2.31)$$

Using this in the definition of the basis expansion of  $\chi$  (Equation 2.29) yields

$$\frac{\chi(a)}{\chi'(a) - \beta \chi(a)} = \sum_{i=1}^N \frac{\hbar^2}{2\mu} \frac{w_i(a)^2}{\epsilon_i - E}. \quad (2.32)$$

The generalized **R** matrix is then defined as

$$\mathbf{R} \equiv \frac{1}{a} \frac{\chi(R)}{\chi'(R) - \beta \chi(R)}, \quad (2.33)$$

which is related to the **S** matrix, and therefore the rest of the typical scattering variables by

$$\mathbf{S} \equiv \frac{H^- - a\mathbf{R}(H'^- - \beta H^-)}{H^+ - a\mathbf{R}(H'^+ - \beta H^+)}, \quad (2.34)$$

where  $H$  are the irregular Coulomb functions.

The  $R$  matrix for the problem at hand, which would be applied to Equation 2.34 is

$$\mathbf{R} = \sum_{i=1}^N \frac{\hbar^2}{2\mu a} \frac{w_i(a)^2}{\epsilon_i - E}. \quad (2.35)$$

For each  $i$ , we can define the “reduced width”  $\gamma_i$  as

$$\gamma_i = \sqrt{\frac{\hbar^2}{2\mu a}} w_i(a) \quad (2.36)$$

such that the **R**-matrix takes on the simple form

$$\mathbf{R} = \sum_{i=1}^N \frac{\gamma_i^2}{\epsilon_i - E}. \quad (2.37)$$

Finding the **S** matrix is considered solving the problem in a reaction theory context. The **S** matrix has easy relationships between all other scattering variables including cross section.

Cross section is an expression of the probability of a reaction occurring at a specific energy and the particles exiting at a specific angle, measured in area units. Theoretically, it is given by

$$\frac{d\sigma}{d\Omega}(\theta, \phi) = \frac{1}{N\Delta\Omega} \frac{I_{\text{out}}}{I_{\text{in}}} \quad (2.38)$$

where  $\Omega$  is the solid angle of the target,  $N$  is the areal density of the target particles,  $I_{\text{out}}$  is the number of particles that scatter, and  $I_{\text{in}}$  is the number of incident particles. The experimental considerations for calculating these values are discussed in Chapter 4.

Thus, by using the individual  $w$  along with their energies, but *not* their derivatives, all scattering variables can be found.

If the scattering takes place into a well-defined resonance of the compound nucleus,

$$\mathbf{R} = \frac{\gamma_r^2}{E_r - E} \quad (2.39)$$

where  $\gamma_r$  and  $E_r$  are the true width and energy of the resonance. The observed width and energy  $E_R$  and  $\Gamma_R$  are related to these quantities by

$$\Gamma_R^2 = \frac{\gamma_r^2}{1 + \gamma_r^2 S'_l(E_r)} \quad (2.40)$$

and

$$E_R = E_r - \gamma_r^2 \frac{S_l(E_r)}{1 + \gamma_r^2 S'_l(E_1)} \quad (2.41)$$

where  $S_l$  is the shift factor for the resonance defined by the Coulomb functions and the channel radius. See [29].

In the Lane and Thomas [28] formulation of R-Matrix theory, the cross section is related to the “collision matrix”,  $\mathbf{U}$ . This matrix is defined as the amplitude of the outgoing waves resulting from a unit flux of incoming waves. The collision matrix is found both inside and outside of the channel radius, which in this work is defined to be

$$a = r_c(A_1^{1/2} + A_2^{1/2}) \quad (2.42)$$

where  $r_c$  is between 1.4 and 1.5 femtometers. The Schrödinger equation is solved similarly to above. The wavefunctions for the outer region are represented as a sum of incoming and outgoing waves,  $I_l$  and  $O_l$ .  $L_l$  is the logarithmic derivative of the  $O_l$ , and  $L_l^*$  the logarithmic derivative of the  $I_l$ . In terms of the R-matrix, defined the same as above, the collision matrix is defined as

$$U_l = \frac{I_l}{O_l} \frac{1 - L_l^* R_l}{1 - L_l R_l}. \quad (2.43)$$

Using the Breit-Wigner approximation, which ignores off diagonal terms, the elements of  $\mathbf{U}$  are

$$U_{cc'} = \sqrt{U_{cc}^0 U_{c'c'}^0} \left[ \delta_{cc'} + \frac{i\sqrt{\Gamma_c(E)\Gamma_{c'}(E)}}{E_r - E - \frac{i}{2}\Gamma(E)} \right] \quad (2.44)$$

where  $c$  and  $c'$  are the incoming and outgoing channels,  $\Gamma_c$  and  $\Gamma_{c'}$  are the partial widths,  $E_r$  is the resonance energy and  $\Gamma(E)$  is the elastic width.  $U_{cc}^0$  and  $U_{c'c'}^0$  are the elements of the  $\mathbf{U}$  matrices that describe the non-resonant scattering in channels  $c$  and  $c'$  respectively.

This can then be used to find the cross section

$$\frac{d\sigma}{d\Omega} = \frac{1}{(2I_1+1)(2I_2+1)} \sum_{M_1 M_2} \sum_{M'_1 M'_2} \left| f_C(\Omega) \delta_{M'_1 M_1} \delta_{M'_2 M_2} + f_{c' M'_1 M'_2}^{(c M_1 M_2)}(\Omega) \right|^2 \quad (2.45)$$

where

$$\begin{aligned} f_{c' M'_1 M'_2}^{(c M_1 M_2)}(\Omega) &= i \frac{\sqrt{\pi}}{k} \sum_{J\pi} \sum_{I\ell} \sum_{I'\ell'} \sqrt{2\ell+1} e^{i(\sigma\ell+\sigma\ell')} (I_1 I_2 M_1 M_2 | IM) \\ &\times (I\ell M 0 | JM) (I'_1 I'_2 M'_1 M'_2 | I'M') (I'\ell' M' M - M' | JM) \\ &\times \left( \delta_{c'c} \delta_{I'I} \delta_{\ell'\ell} - U_{c'I'\ell', cI\ell}^{J\pi} \right) Y_{\ell'}^{M-M'}(\Omega), \end{aligned} \quad (2.46)$$

where the  $I_i$  are the spins of the two colliding particles,  $\ell$  is the orbital angular momentum,  $J$  is the total angular momentum,  $M$  is the projection of the total angular momentum, and  $\pi$  is the parity of the system.

For a spin-zero resonance in exactly one reaction channel and exactly one partial wave, this complicated expression simplifies to the Breit-Wigner form given by

$$\frac{d\sigma}{d\Omega}(E, \theta) = \frac{(2L+1)^2}{4k^2} \frac{\Gamma^2}{(E - E_0)^2 + \frac{1}{4}\Gamma^2} P_L^2(\cos\theta), \quad (2.47)$$

where  $L$  is the orbital angular momentum,  $E_0$  is the energy of the resonance,  $\Gamma$  is the width of the resonance,  $k$  is the wave number, and  $P_L$  are the Legendre polynomials. This dependence on the Legendre polynomials is used extensively in the analysis of the experiments in this thesis.

Since the scattering is between two spin-zero particles, the  $L$  is exactly equal to  $J$ , the total angular momentum. Additionally, the parity follows the rule that  $\pi = (-1)^L$ , so even- $J$  states always have positive parity and odd- $J$  states always have negative parity.

## 2.4 Three-Body Theory

The structure and decay of three body states can be interpreted using the Gamow Coupled Cluster method of Wang, *et al.* [30] In this method, the  $^{14}\text{C}$  nucleus is considered as a  $^6\text{He}$  core with two valence  $\alpha$  particles. These clusters (not just  $\alpha$  clusters as in the rest of this thesis) are the basic building blocks of the theory and do not themselves have structure or internal interactions, similar to the basic assumptions of cluster theory in general. These three clusters are governed by the Hamiltonian

$$\hat{H} = \sum_{i=1}^3 \frac{\hat{\mathbf{p}}_i^2}{2m_i} + \sum_{i>j=1}^3 V_{ij}(\mathbf{r}_{ij}) - \hat{T}_{\text{c.m.}}, \quad (2.48)$$

where  $V_{ij}$  is the interaction between the clusters  $i$  and  $j$ , including the central, spin-orbit, and Coulomb forces; and  $\hat{T}_{\text{c.m.}}$  is the kinetic energy of the center of mass of the nucleus.

To ensure that Pauli exclusion is respected, an additional term is added to the Hamiltonian,

$$\hat{Q} = \Lambda \sum_c |\phi^{jcm_c}\rangle \langle \phi^{jcm_c}|, \quad (2.49)$$

where  $\Lambda$  is a constant and  $|\phi^{jcm_c}\rangle$  is a Pauli-forbidden state.

To remove the center of mass motion, the Hamiltonian is expressed in the Jacobi coordinates

$$\begin{aligned} \mathbf{x} &= \sqrt{\mu_{ij}}(\mathbf{r}_i - \mathbf{r}_j), \\ \mathbf{y} &= \sqrt{\mu_{(ij)k}} \left( \mathbf{r}_k - \frac{A_i \mathbf{r}_i + A_j \mathbf{r}_j}{A_i + A_j} \right) \end{aligned} \quad (2.50)$$

where  $\mathbf{r}_i$  is the position vector of the  $i$ th cluster,  $A_i$  is the mass number of the  $i$ th particle and the  $\mu$  are the reduced masses defined as,

$$\begin{aligned}\mu_{ij} &= \frac{A_i A_j}{A_i + A_j}, \\ \mu_{(ij)k} &= \frac{(A_i + A_j) A_k}{A_i + A_j + A_k}.\end{aligned}\tag{2.51}$$

The Jacobi coordinates can represent two different systems, denoted “T” and “Y”, as shown in Fig. 2.9. To move between these two types of coordinates, the hyperspherical coordinates and hyperspherical harmonics are used. These are represented by the hyperradius  $\rho$  and the five-dimensional hyperangle  $\Omega_5$ . In terms of these hypercoordinates, the total wavefunction of the nucleus is given by

$$\Psi^{JM\pi}(\rho, \Omega_5) = \rho^{-5/2} \sum_{\gamma K} \psi_{\gamma K}^{J\pi}(\rho) \mathcal{Y}_{\gamma K}^{J\pi}(\Omega_5),\tag{2.52}$$

where  $K$  is the hyperradial quantum number,  $\gamma$  represents the rest of the quantum numbers (spin and orbital angular momentum),  $\psi$  is the hyperradial wavefunction and  $\mathcal{Y}$  is the hyperspherical harmonic.

This creates a complicated, hyperspherical version of the radial Schrödinger equation which can be solved to give both bound states and decaying resonant states. For these states, the decay width and density of valence clusters are calculated, as well as the inter-cluster distance. The valence cluster density is given by

$$\rho_{nn'}(r, r', \theta) = \langle \Psi | \delta(r_1 - r) \delta(r_2 - r') \delta(\theta_{12} - \theta) | \Psi \rangle\tag{2.53}$$

where  $r_1$ ,  $r_2$ , and  $\theta_{12}$  are defined as in Fig. 2.9. This  $\rho$  can then be integrated over all radii to find the angular density of the valence clusters.

For  $^{14}\text{C}$ , several  $5^-$  states were calculated in the range of this work with cluster-like widths. Their inter-cluster distance distributions as well as valence angular distributions are shown in Figs. 2.10 and 2.11. The first state calculated is below the two-alpha decay threshold and has a triangular shape. The other states exist in a superposition of structures that is triangular or

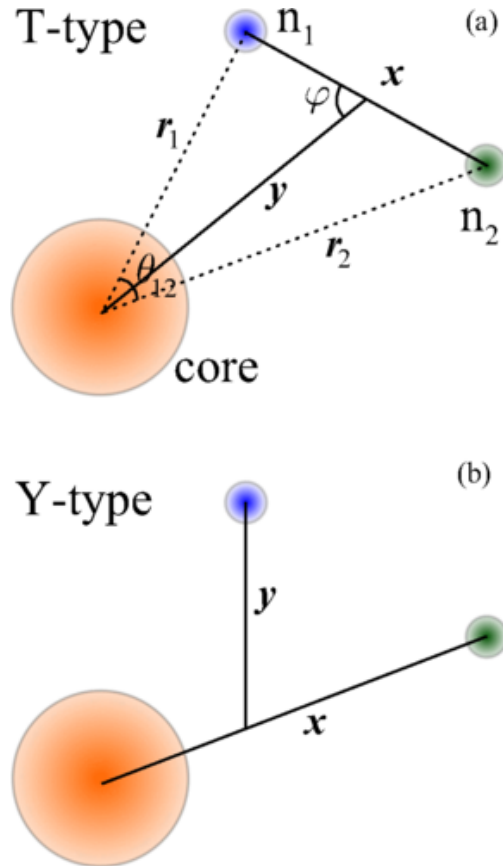


**Figure 2.9: Jacobi T and Y Coordinates** Based on the definition of the Jacobi coordinates in Equation 2.50, there are two different basis sets, the “T” and “Y” sets shown here. These are named because the  $x$  and  $y$  vectors trace paths that look similar to those letters. Figure from [30].

chain-like. The valence angular distributions contain information both about the structure and decay channels. The peak at low angles in Fig. 2.11(b) indicates that there is a strong contribution of sequential decay. For the higher-lying states, there is no similar peak so either a democratic or sequential pattern is possible.

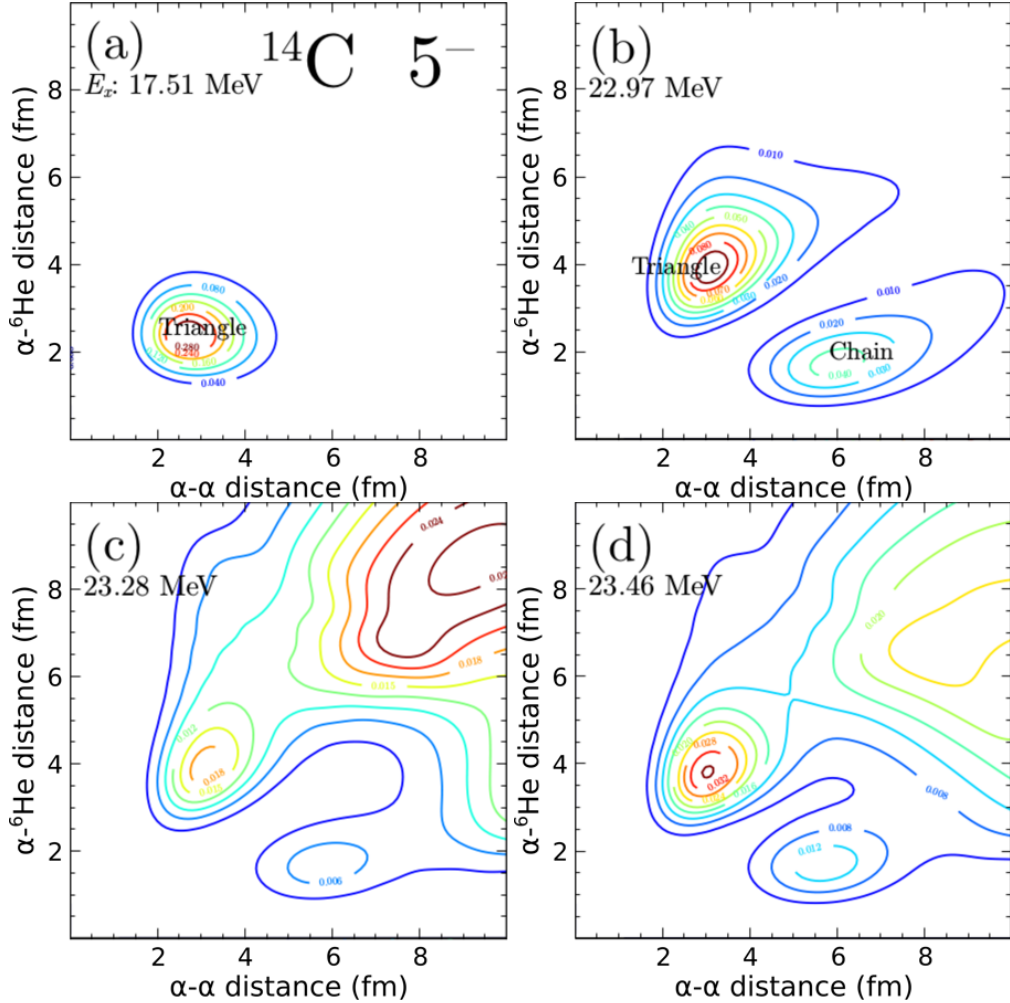


**Figure 2.10: Intercluster Distances** Four  $5^-$  states as calculated by S.M. Wang in the experimental range. States have either chain-like or triangular shapes, as indicated. Excitation energies correspond to those in Fig. 2.11. Figure from [31].

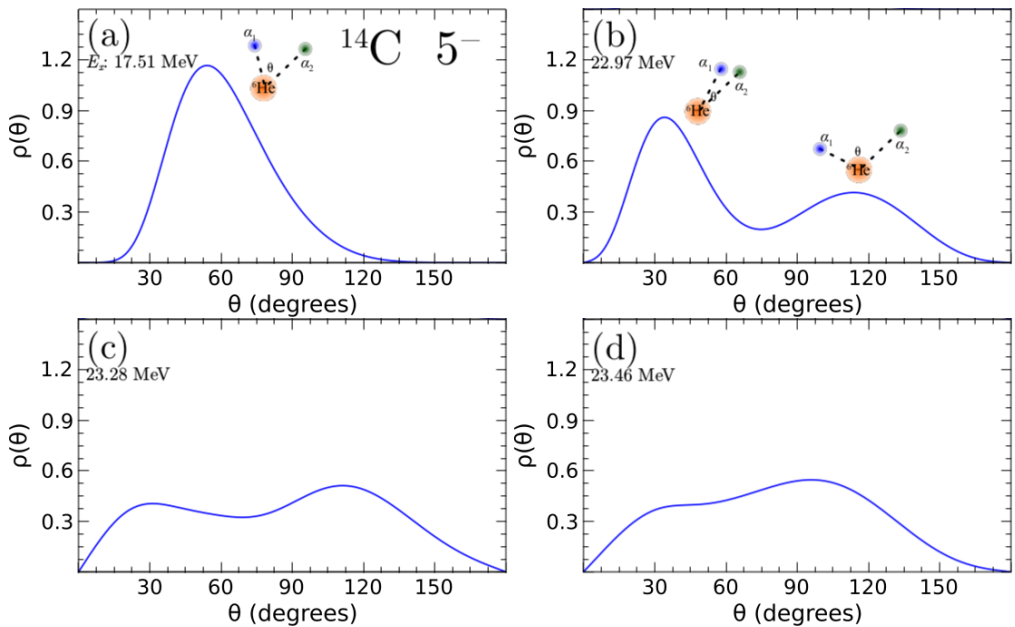


**Figure 2.11: Angular Distributions** Four  $5^-$  states as calculated by S.M. Wang in the experimental range. Figure *b* indicates a strong sequential decay channel. Excitation energies correspond to those in Fig. 2.10. Figure from [31].

## CHAPTER 3

### EXPERIMENT

#### 3.1 pAT-TPC

The Prototype Active Target Time Projection Chamber (pAT-TPC) [32] is the primary detector used in this work.

Externally, the detector is an stainless-steel-enclosed cylinder that is approximately 70 cm long and 40 cm in diameter. Inside of this is a field cage made of G10 glass-reinforced epoxy laminate that is 50 cm long and has an inner diameter of 25 cm. [32]

The field cage is filled with the combined target and tracking gas. In the experiments in this work this active gas was a volumetric mixture of 90% He and 10% CO<sub>2</sub> at 720 torr. The CO<sub>2</sub> serves as a “quench” gas. This is to overcome problems inherent to electron multiplication in a noble gas. If, instead of ionizing the He, the atom simply excites, a photon is released that can subsequently interact with other atoms or the wall of the detector to cause spurious ionization and subsequent discharge. Additionally, these photon-induced effects can have a negative effect on spatial resolution of the detector. The addition of a small amount of polyatomic quench gas acts to reduce these effects by preferentially absorbing these photons. [1]

The beam entrance to this active volume is a 3.7  $\mu\text{m}$  (1.45  $\mu\text{g}/\text{cm}^3$ ) thick para-aramid foil of 2.5 cm diameter. This foil separates the gas in the field cage, which is held near one atmosphere of pressure, from the high vacuum of the beam line.[32]

Near the beam entrance there is a cathode typically held at -40 kV. There is an anode at the far side of the detector, and these are connected by aluminum equipotential rings that are mounted both inside and outside of the field cage. Each ring is separated by a 2 M $\Omega$  resistor. Together, these rings define a uniform electric field inside the detector. The last ring can have an external voltage applied because the spacing between the rings and the anode is not the same as the spacing between rings. This external voltage can be adjusted to ensure field uniformity.

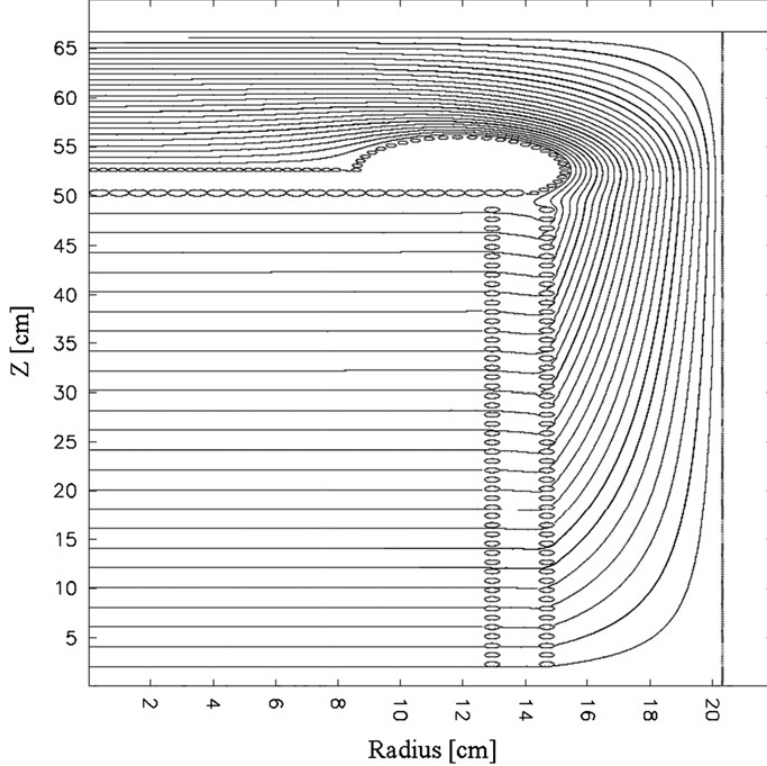


**Figure 3.1: Electric Field Uniformity** Electric field lines are shown in solid lines. Note their constant spacing indicating a uniform field. Equipotential rings are shown at radii 13 and 15 cm, and the cathode at 50 cm. Figure from [32].

This, in principle, results in an electric field non-uniformity of < 1%. A simulation showing this uniformity (from [32]) is shown in Fig. 3.1.

In a gas with an electric field, positively charged ions move in the direction of the field, and negatively charged ions move against it. This motion, along with the random thermal velocity and collisions with gas particles results in a constant drift velocity  $v$  given by

$$v = \frac{\mu E}{P} \quad (3.1)$$

where  $\mu$  is the “mobility” of the gas,  $E$  is the electric field, and  $P$  is the pressure. [1] The drift velocities for electrons in the current work are  $2.5 \text{ cm}/\mu\text{s}$ .

As a charged particle moves through gas, it loses energy and eventually comes to rest by electrical interactions with the atoms in the gas. This energy loss,  $\frac{-dE}{dx}$ , is not a constant for all energies or masses. As the energy of the particle decreases,  $\frac{-dE}{dx}$  increases. For non relativistic

particles,

$$\frac{-dE}{dx} \propto \frac{MZ^2}{E} \propto \frac{Z^2}{v^2} \quad (3.2)$$

for the particle velocity  $v$ . This rise at low velocities creates a characteristic peak in energy loss just before the particle come to rest is referred to as the “Bragg Peak”. [1] Energy losses for ions are tabulated in the program SRIM. [33] This variational energy loss is important in the analysis of the experiments in this work, especially since particles frequently stop inside the gas of the active volume.

The active volume of the pAT-TPC is enclosed in a second, insulating volume that fills the cylindrical shell between the field cage and the outside of the detector. This outer volume is typically filled with nitrogen. This volume serves to electrically insulate the outside of the detector from the high voltage within. The field cage is susceptible to mechanical damage if the two volumes have pressures that differ by too much. A  $70\mu\text{g}/\text{cm}^2$  polypropylene foil is mounted on a bypass between these two volumes. If the pressure differential is greater than approximately 0.1 atm, the foil will break and the pressures will equilibrate.

On the side of the detector opposite that of the beam entrance, there is a position detection pad plane, the Micromegas, that is discussed in more detail in Section 3.1.1. The layout of the detector is shown graphically in Fig. 3.2.

On the outside of the detector, on the same side as the Micromegas, is a flange containing gas inlets and feedthroughs for electronics. This is shown in in Fig. 3.3.

An experiment in the pAT-TPC proceeds as follows (see Fig. 3.4). A beam particle enters the gaseous volume and interacts with the target gas, inside of the active volume. After any reaction occurs, a number of particles leave the interaction region. All charged particles involved in the reaction, including the beam and any outgoing particles, ionize the gas as they travel through it. These newly-freed electrons travel opposite the electric field to the end plane of the detector where their position in  $x$  and  $y$  are recorded along with their time of arrival. This time is used, along with the drift velocity of the target gas, to find the  $z$  coordinate of where the electron was produced.

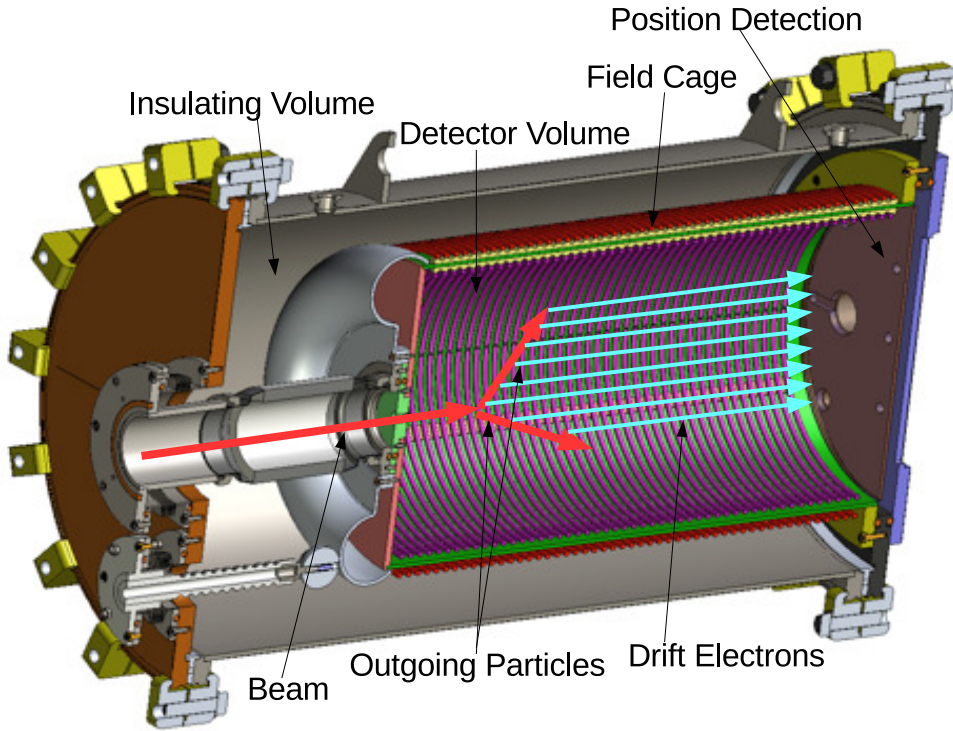


**Figure 3.2: Prototype Active Target Time Projection Chamber** Schematic of the pAT-TPC showing the various parts of the detector.



**Figure 3.3: Photograph of Flange** On the left are the two gas inlets, for the active and insulating volumes (outlets are positioned elsewhere) flanking high voltage feedthroughs for powering the Micromegas and last ring (see text). The long vertical slit is the connector where the GET electronics attach to the detector.

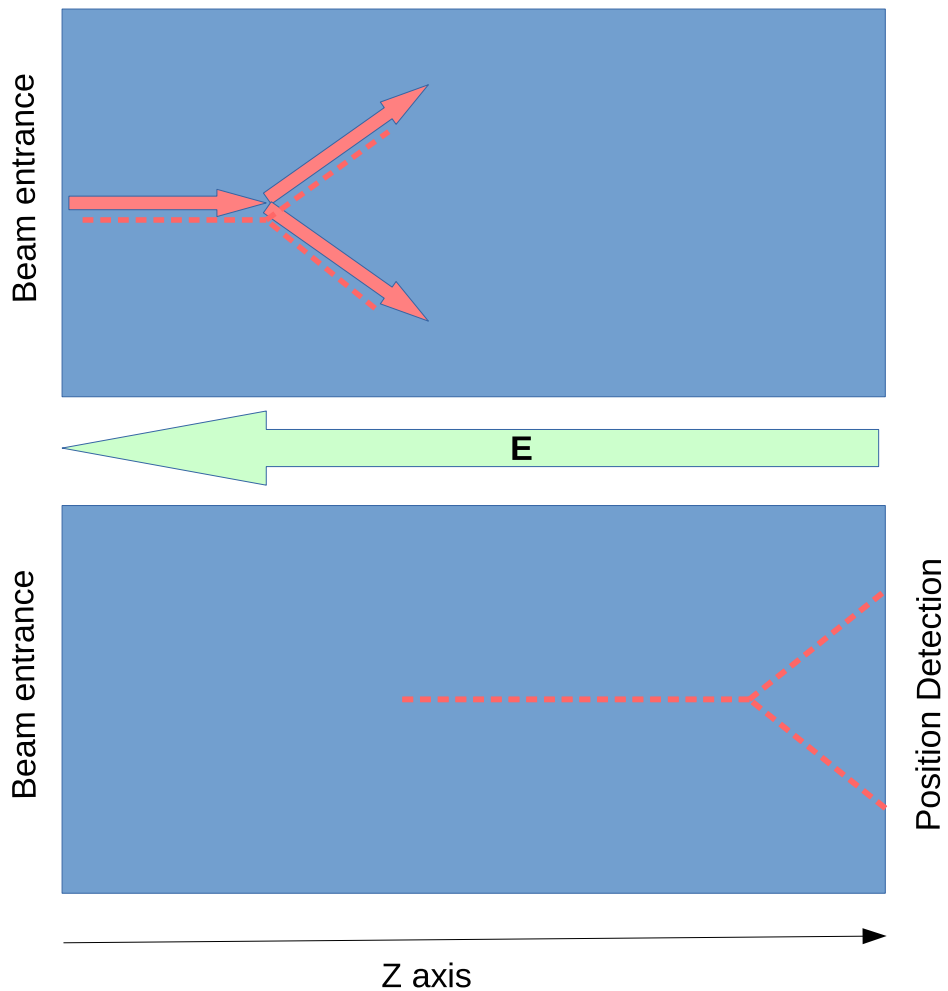


**Figure 3.4: Operation of the pAT-TPC** The two parts of this image are consecutive in time for a single event. While the reaction is taking place, all of the involved particles are ionizing the tracking gas. These electrons then drift to the other side of the detector where their properties are recorded

The detector is referred to as an “active target” because the target and tracking media are the same. This has the advantages of providing a thick target without losing energy resolution as well as the ability to measure reactions at a variety of energies with a single beam energy. The beam loses energy as it travels through the detector and can react at any energy starting at its initially delivered energy down to zero. The detector is a “time projection chamber” because it uses the time of the ionization electrons’ arrival in the position detection plane to project out the third coordinate  $z$  coordinate. Thus, three-dimensional “tracks” showing the position of all the charged particles in a reaction as they travel through the detector are produced.

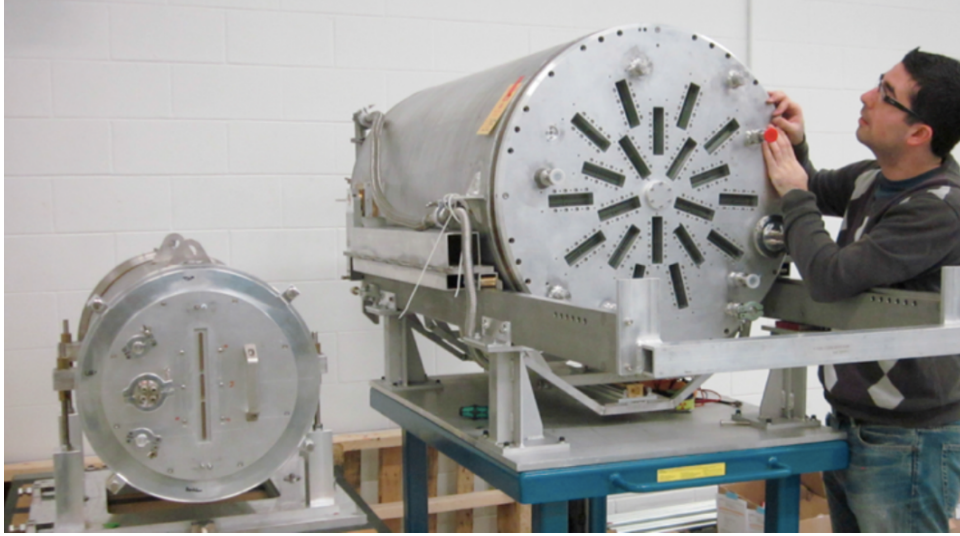


Figure 3.5: **pAT-TPC and AT-TPC** The pAT-TPC is on the left and the AT-TPC is on the right. Note the differences in size and number of slots for mounting electronics.

This detector is the half-scale prototype of the Active Target Time Projection Chamber (AT-TPC). The full-scale AT-TPC has additional improvements like a more granular position detection, the possibility of using a magnetic field, and the ability to tilt the detector on the beam line. A photograph of both detectors is shown in Fig. 3.5. [34]

### 3.1.1 Micromegas

The Micromegas (short for Micro-Mesh Gaseous Structure) [35] is the device used to amplify the ionization electrons and measure the  $x$  and  $y$  positions of the ionized electrons. The Micromegas consists of a micromesh of stainless steel with thickness  $18\ \mu\text{m}$  woven together with a pitch of  $63\ \mu\text{m}$  placed approximately  $100\ \mu\text{m}$  above a grounded, position-sensitive sensor plane. This fine mesh is polarized at  $-350\text{ V}$ . This high negative voltage across a small gap creates a large electric field compared to that in the rest of the detector. This sudden change of electric field causes a multiplication of electrons in the gap by a factor of up to  $\sim 10,000$ . These secondary electrons then arrive at the sensor plane which also serves as the anode for the detector's electrical system. This is shown in Fig. 3.6.

The sensor plane is divided into 256 sectors or “pads” that correspond to position. The pat-

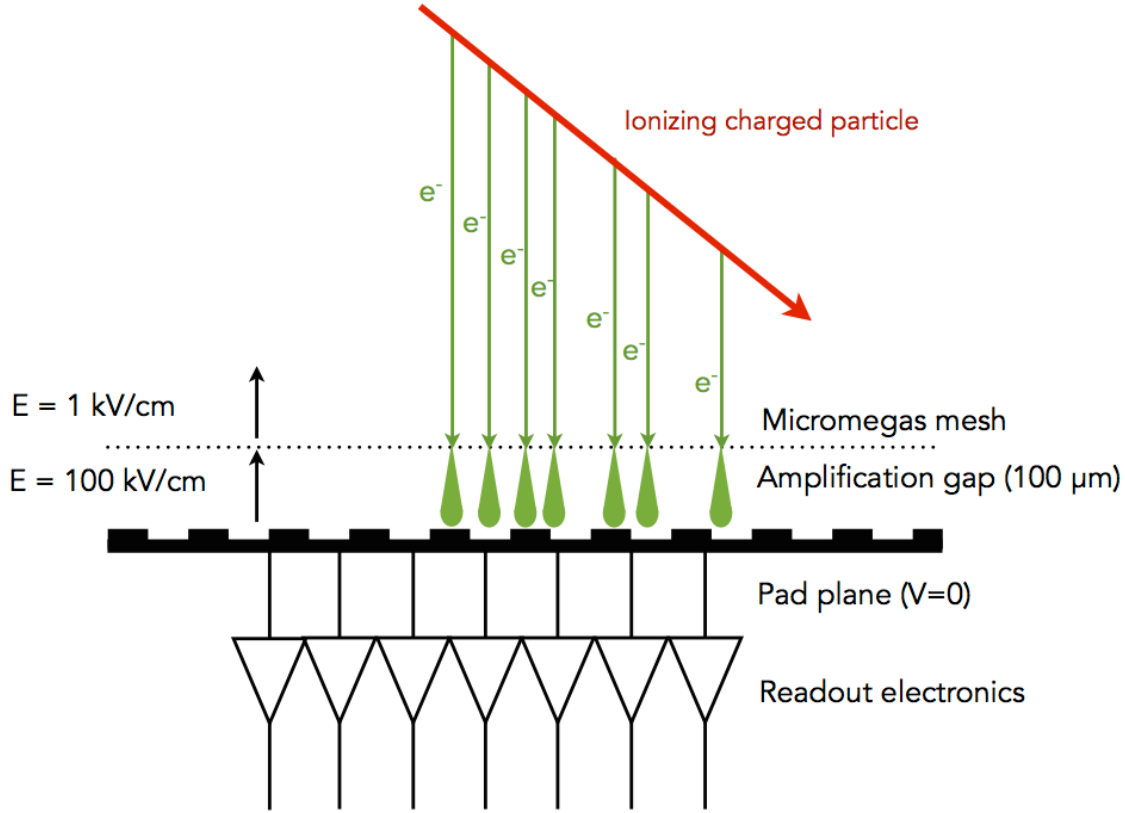


Figure 3.6: **Micromegas Operations** Figure not to scale. Electric field values are approximate and can be adjusted based on voltage supplied to the various pieces of the detector.

tern on this particular plane is a circular backgammon pattern. This means that the circle is first divided into quadrants, then rings, and then the individual rings are further divided into rounded triangles. This is shown in Figs. 3.7 and 3.8. There are several reasons for this design. First, the opposite quadrants can be used as triggers to collect two-body events. In order to conserve energy and momentum in a two-body event, opposite quadrants must be activated. The backgammon structure of interlaced triangles assists with the reconstruction of three-body events. By using the charge division between consecutive triangles, e.g.

$$\frac{Q_1 - Q_2}{Q_1 + Q_2}, \quad (3.3)$$

the  $\varphi$  angle can be calculated for different tracks. The use of the backgammon Micromegas is one major difference in operation between the experiment in the present document and the

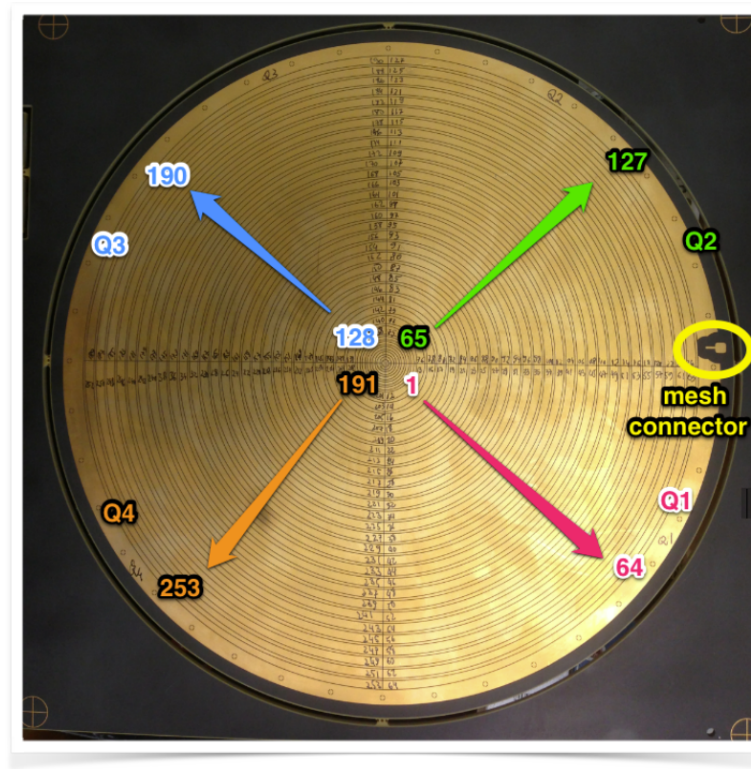


Figure 3.7: **Backgammon Micromegas** Full view of the Micromegas used in these experiments.

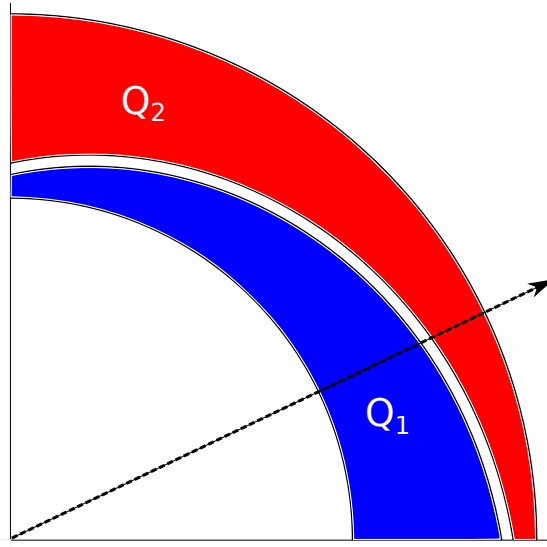


Figure 3.8: **Backgammon Detail View** Detailed view of how two rounded triangular pads come together to form a single strip of the Micromegas. If a track, such as the black line, crosses the pads, differing amounts of charge will be collected by each pad. Using the charge division between these pads, the  $\varphi$  angle can be determined.

one in [17]. In that experiment, a simple ring structure was used, so three-body events were not reconstructed.

### 3.1.2 Electronics

The pAT-TPC uses the General Electronics for Time Projection Chambers (GET) system which was developed by an international collaboration. [36] The GET system is responsible for digitizing and recording the full electronic trace from each pad. The first part of the GET system is an Application Specific Integrated Circuit (ASIC) called the AGET (ASIC for GET). This chip amplifies and stores the signal from the Micromegas in an SCA. Additionally, the AGET delivers a leading-edge discriminator signal (LED). Each AGET can handle up to 64 channels. Four AGETs are mounted together on an AsAd (ASIC Support and Analog to Digital Conversion). The AsAd provides a direct connection to the Micromegas for the AGET by attaching to the electronics slots visible in photographs of the detector. The AsAd transmits the AGET signals to the rest of the system whenever the AsAd receives a trigger signal. For the pAT-TPC, there is exactly one AsAd, but the GET system is highly adaptable and can be used with many more. The digitized signal passes from the AGET through the AsAd to the CoBo (Concentration Board). The CoBo is a microTCA module that takes inputs from up to four AsAds and sends them to the storage disks when the CoBo receives the trigger signal. The CoBo also calculates the multiplicity of LEDs, which can, in turn, be used to create the trigger. The trigger for each experiment is discussed in more detail in Chapter 4.

## 3.2 Beam Facility

The experiments presented here were performed at the Institute for Nuclear Astrophysics (ISNAP) at the University of Notre Dame. A layout of ISNAP can be seen in Fig. 3.9. The primary beam of  $^{11}\text{B}$  was formed by the Multi-Cathode Source of Negative Ions by Cesium Sputtering (MC-SNICS)  $^{11}\text{B}+\text{Ag}$  ion source, accelerated by the FN Tandem Van de Graaff accelerator, and separated by the *TwinSol* separator [37].

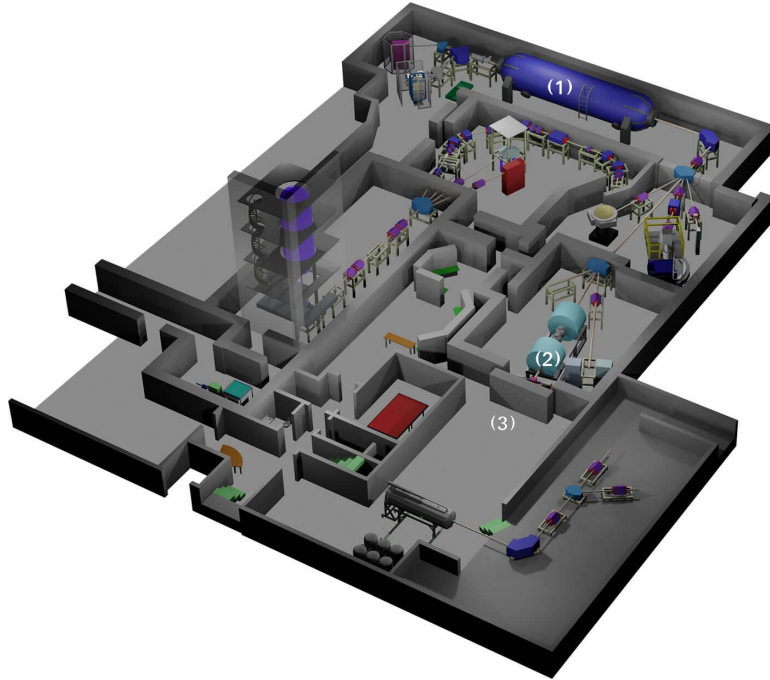


Figure 3.9: **Layout of ISNAP** (1) is the FN Tandem Van de Graaff Accelerator. (2) is *TwinSol*. (3) is where the pAT-TPC is placed during an experiment.

### 3.2.1 Tandem Accelerator

When an ion is extracted from the ion source it has charge state  $-1$  and very low energy. The accelerator used at in these experiments is the FN Tandem Van de Graaff accelerator. At the mid point of the accelerator there is a positive voltage of up to 8 MV. This attracts the negatively charged ions, representing the first acceleration process. When the ions arrive at this mid point, they pass through a stripper foil of  $3 \mu\text{g}/\text{cm}^2$  carbon. This foil removes electrons from the ion. The ions, now positively charged, accelerate away from the midpoint of the accelerator due to its high, positive voltage. At the end of the accelerator, the beam passes through a 90 degree dipole magnet that selects the final charge state and directs it to the target in a beam line.

The  $^{11}\text{B}$  beam is incident on  $^{13}\text{C}$  foils creating a secondary beam of  $^{10}\text{Be}$  with contaminants. This beam enters to the *TwinSol* separator for focusing into the pAT-TPC.

### 3.2.2 TwinSol

*TwinSol* is a twin superconducting solenoid magnet low-energy radioactive nuclear beam apparatus [37]. The magnet is a 6 T magnet consisting of two solenoid apertures through which the beam is focused into the experimental area.

## 3.3 Experimental Setup

The experiment was performed two entirely independent times with similar, but not identical parameters. In both cases, the beam began as a primary beam of  $^{11}\text{B}$  which was accelerated through the tandem accelerator to be incident on  $^{13}\text{C}$  foils. The remnants of this reaction were separated by *TwinSol* to give a beam of  $^{10}\text{Be}$ . The main difference between the experimental runs was the energy of the beam as it enters the pAT-TPC. The “low-energy” experiment had beam incident at 20 MeV total lab energy, and the “high-energy” experiment had beam incident at 38 MeV total lab energy. These delineations are used in the rest of the thesis.

In the case of the high-energy experiment, before the beam entered the pAT-TPC, it went through a micro-channel plate detector (MCP) which gave a timing to the events. An MCP is an electron-multiplication device that gives a fast signal when charged particles interact with it. A photograph showing the experimental setup is shown in Fig. 3.10.

The low-energy experiment was triggered by using the multiplicity of the Micromegas. If the total number of pads hit in the event exceeded a threshold, then the event was recorded. In order to prevent too many triggers from unreacted beam particles, pads very close to the center of the detector were excluded from this multiplicity trigger.

The high-energy experiment was triggered based on a fixed-width coincidence window being opened when the beam passed the MCP. The width of the window was based on the drift velocity of the gas. When the window closes, if there has been signal on the Micromegas later than the initial beam particle, then the event is recorded. The transmission between the MCP and pAT-TPC is approximately 8%.

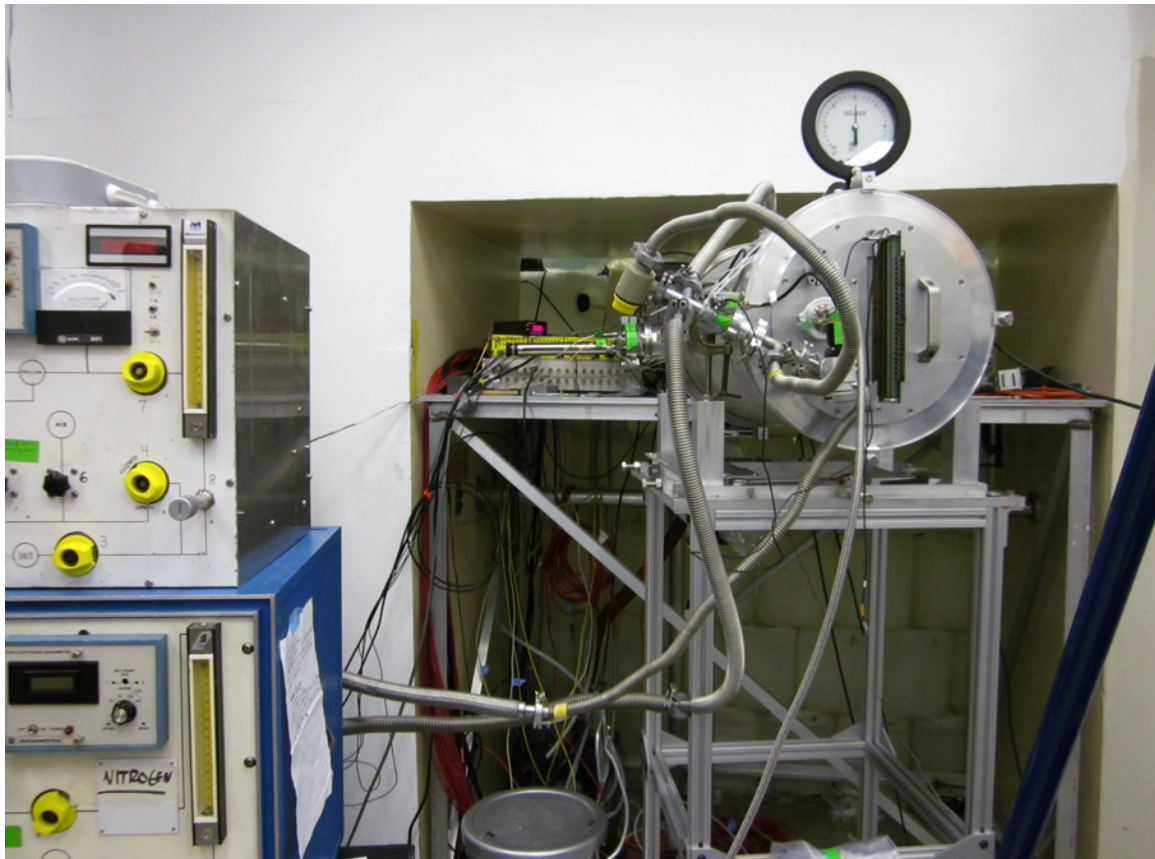


**Figure 3.10: Experiment Setup** The pAT-TPC is set up at the end of the ISNAP beam line. The pressure gauge is visible above the detector. The MCP is placed in the cross upstream of the detector. In the left of the photograph the two gas handling systems, for the He-CO<sub>2</sub> and Nitrogen, are visible.

## CHAPTER 4

### ANALYSIS AND RESULTS

All data analysis for these projects was completed in the ATTPCROOT framework written by Yassid Ayyad.<sup>1</sup> This is an analysis and simulation framework based on FairRoot [38] specifically for the AT-TPC and pAT-TPC.



$$M_C = \frac{\sum_{k=M-5}^{M+5} (kA(k))}{\sum_{k=M-5}^{M+5} A(k)} \quad (4.1)$$

where  $A$  is the amplitude in a certain time bucket. Then, using the width of the time bucket and the drift velocity of the gas, the  $z$  coordinate of the hit is determined from this center of gravity.

The  $x$  and  $y$  coordinates are assumed to be the center of the pad that was hit, meaning that all hits are assumed to be at a  $45^\circ$  angle in  $\varphi$ , in the middle of the quadrant. The backgammon shape of the Micromegas can be used to get the true  $\varphi$  angle of a complete track, if a better precision is necessary.

After this, each event is characterized by a series of points in  $x$ ,  $y$ , and  $z$  called a “hit pattern”. In order to extract physics variables like scattering angle and energy, these points must be reconstructed into lines and interpreted based on the experimental parameters.

#### 4.1 Two-Body Events at Low Energy

##### 4.1.1 Reconstruction

The experiment run at 20 MeV was reconstructed using the Hough transformation method. This is a robust line-finding algorithm that works by transforming points into lines and back again.

The analysis of a potential track starts as a series of points in two-dimensional coordinate

---

<sup>1</sup>Available at <https://github.com/ATTPC/ATTPCROOTv2/>.

space. The coordinates are  $r$ , the radius of the center of the pad in the Micromegas that was hit along with  $z$ , the coordinate along the beam axis of the same hit. There are many lines that could describe any one point, each with a different slope and y-intercept. For example, the point (1,1) is on the line  $y = x$ ,  $y = 0.5x + 0.5$ , and infinitely many other lines. The slopes and intercepts of these lines can be plotted against each other to make a line in the “Hough space”. Transforming from coordinate space to Hough space is called the “Hough transform”. The linear Hough space is in slope-intercept space, not in coordinate space. Every point in coordinate space corresponds to a line in Hough space. These Hough lines intersect at the slope and intercept corresponding to the line that describes all points. Even if not all points exactly fall in a straight line, a the majority that are related to a common straight line will. Because of this, the Hough transform is a robust procedure to find incomplete or otherwise imperfect lines. [39] This is especially useful since some tracks in this experiment had bent ends. This is due to electric field non-uniformity; this problem overcome by the Hough Transform.

In order to prevent infinite slopes, instead of using the typical  $y = mx + b$  form of a line and the Hough space being  $m$  vs  $b$ , the form,

$$r(\theta) = \cos\theta x + \sin\theta y, \quad (4.2)$$

was used where the Hough space is  $r$  vs  $\theta$ , and the  $x$ ,  $y$  are the radius and  $z$  coordinates of Fig. 4.1a. In this formalism, the Hough space consists of curves instead of lines.

An example of this calculation is shown in Fig. 4.1. Even though not every point lies exactly on the same line, the maximum of the Hough space finds the line that best fits most of the points. This is the primary advantage of using Hough space over a traditional linear fit. However, after the initial guess is found by using the Hough transform, a linear fit is performed on all points that are considered “close” to the Hough line. This eliminates the problem of digitization from the Hough histogram. An example showing the robustness of the fit compared to a linear fit is shown in Fig. 4.2.

For two-body events, each quadrant of the pAT-TPC has at most one track, so each quadrant

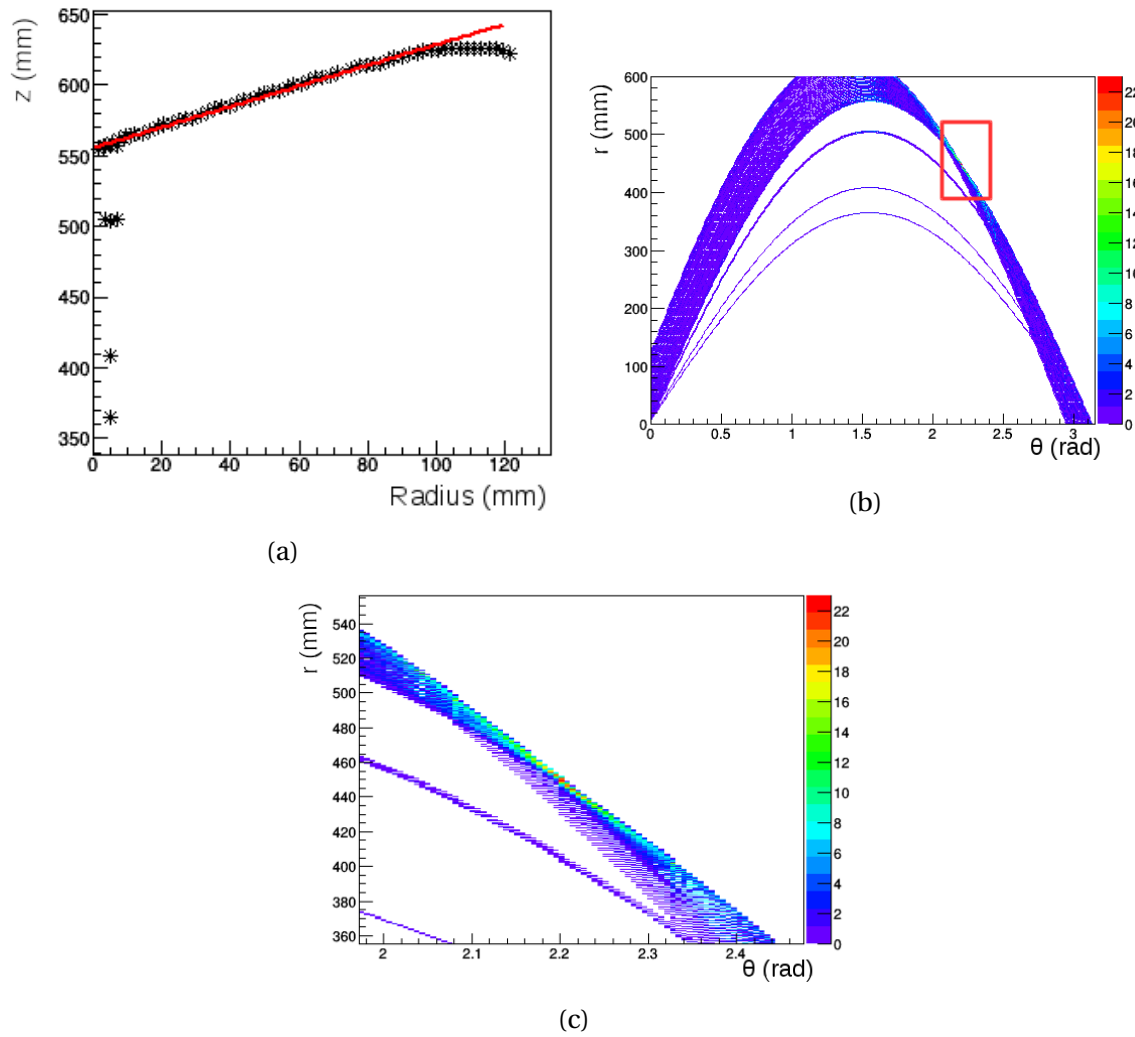


**Figure 4.1: Hough Space Example** (a) displays the points that constitute the track in coordinate space of radius and  $z$  (e.g, the hit pattern). In the (b), every point in coordinate space has been transformed to a curve in the Hough space in  $r$  and  $\theta$ . Note that this is not the same as the scattering angle  $\theta$ . (c) shows the peak in the Hough space, zoomed in to the red square from (b). This peak describes the red line in the first image. Note that the bent end of the track does not disturb the fit.

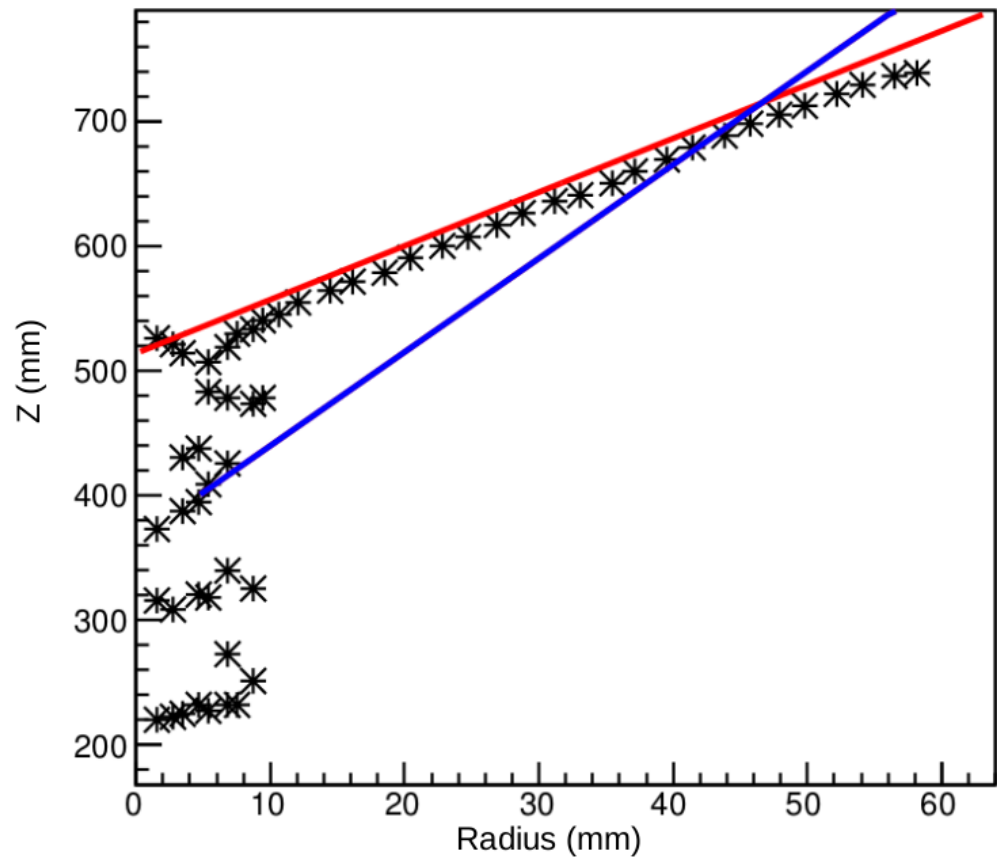
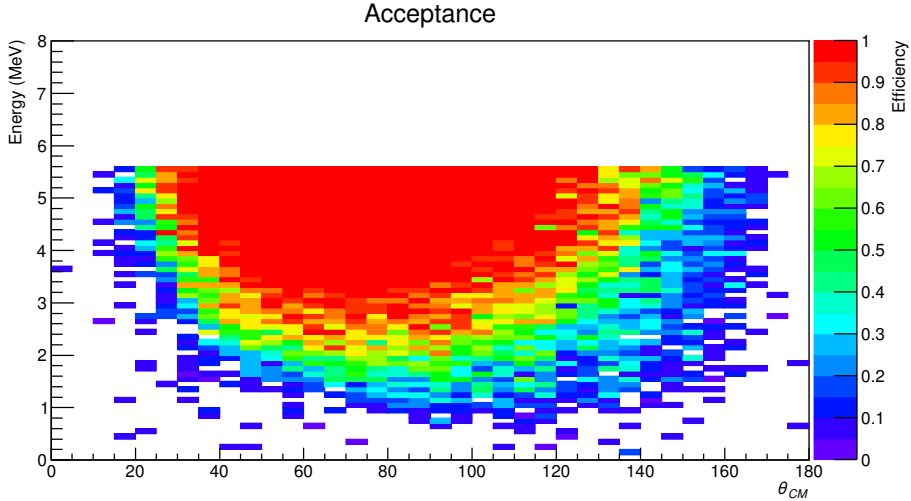


Figure 4.2: **Hough vs Linear Fit** In this figure, the black stars are the hit pattern in a single quadrant from a real, experimental event. The blue line is a standard linear fit while the red line is the result of the Hough transform. The points at small radii are from beam-induced signals, not those of the outgoing particle.

is analyzed independently. Every track in a particular event was found and checked if these tracks are in opposite quadrants, as required by kinematics. Occasionally, there are two sets of tracks that are in opposite quadrants. This case occurs either because the beam is poorly centered causing the track to start in one quadrant and end in the other, or because the particle track ran parallel to the division between two quadrants. To resolve this, the set with a lower reduced  $\chi^2$  per degree of freedom was used to continue with the analysis, where the  $\chi^2$  is that of the linear fit performed after the Hough transform in the reconstruction step.

#### 4.1.2 Simulation

To understand the efficiency of the detection system, a GEANT4 simulation was performed. A kinematic simulation of elastic scattering was used to create events at all physically possible angles and energies. This means that the  $^{10}\text{Be}$  enters the reaction with between 0 and 20 MeV and a random outgoing scattering angle is selected in an unbiased way within the physically possible domain. Based on those two parameters, the rest of the reaction variables are determined. Then, these simulated events were passed through a simulated version of the detector, including a simulation of the trigger. The output of this simulated detector is the same format as the output of the real detector, so the events can be analyzed using the same analysis program. By calculating the number of events for which the analysis process returns a valid angle and energy and by dividing by the number of simulated events that had those same parameters, the overall efficiency of the detection system was calculated. This two-dimensional efficiency is shown in Fig. 4.3. Losses are most evident for two classes: low energy, and extreme angle. For a low energy event, the outgoing particles do not have sufficient energy to hit many pads, thus the multiplicity threshold is not met. Similarly for large or very small center of mass angles. If one of the particles is pointed very forward in the lab, very few pads will be struck, thus the multiplicity threshold will not be met.



**Figure 4.3: Low-Energy Detector Acceptance** This simulation accounts for the trigger conditions and the geometry of the detector. The color axis is the probability that an event that occurs with the parameters indicated on the  $x$ - and  $y$ - axes will be recorded.

#### 4.1.3 Analysis

The Hough space analysis of the track gives the angle with respect to the beam axis of the detector for each track. These are plotted against each other as shown in Fig. 4.4. In the detector it is not known *a priori* which quadrant is being hit by which particle. Quadrant 1 and Quadrant 2 are arbitrary designations. In order to separate the particles, the plot is “folded” along the line  $y = x$ . Then,  $\theta_1$  corresponds to the lower-mass particle, the  $\alpha$  in the reaction of interest.

Since the beam is radioactive beam, it is not 100% pure. Contamination of the beam is evident in the kinematics plot, especially along the  $\alpha - \alpha$  elastic scattering line. To continue the analysis, the events that correspond to the elastic reaction (outlined in red in Fig. 4.4) are selected. These events are placed into what is referred to as an excitation function which gives the cross section for various reaction states. This has three items to be calculated: the center of mass angle, the center of mass energy, and the cross section.

For an elastic reaction at non-relativistic energies, the center-of-mass angle is the simplest of the three quantities.

$$\theta_{CM} = 2(90^\circ - \theta_1) \quad (4.3)$$

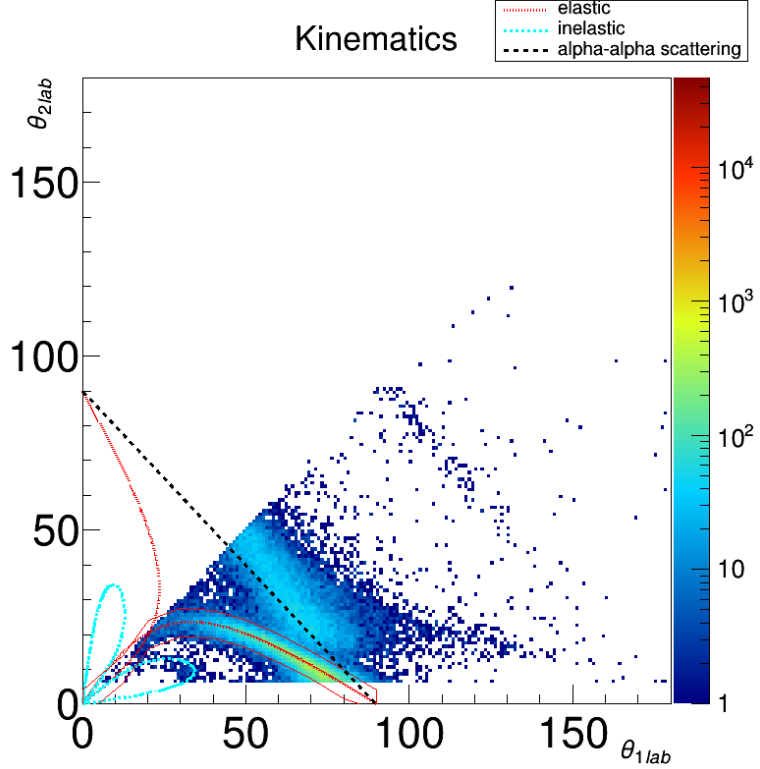


Figure 4.4: **Low Energy Two-Body Kinematics**  $\theta_1$  compared to  $\theta_2$  for the low-energy experiment. This plot is “folded” along the line  $y = x$  and shows several theoretical curves. The red dotted line is for the  $^{10}\text{Be}$  on  $\alpha$  elastic reaction. The blue dotted line is for the inelastic reaction of  $^{10}\text{Be}$  exiting in its first excited state, assuming that the reaction happened at the entrance to the detector. The red outline is the cut made to select elastic events.

where  $\theta_1$  is the lab angle of the  $\alpha$  particle.

The center-of-mass energy is slightly more complicated. There are two methods that were explored in making this determination. The first method is called the vertex method. As discussed in 3.1, the pAT-TPC provides a determination of the  $z$  coordinate at which the reaction took place, the vertex. Using the SRIM [33] energy loss tables, this  $z$  coordinate can be converted to an energy, since the energy at which the beam entered the detector is known. This lab energy is converted to center of mass energy by multiplying by the mass ratio

$$\frac{M_\alpha}{M_\alpha + M_{^{10}\text{Be}}} = \frac{2}{7}. \quad (4.4)$$

The other option is called the quadrant method. It relies on the length of the two outgoing scat-

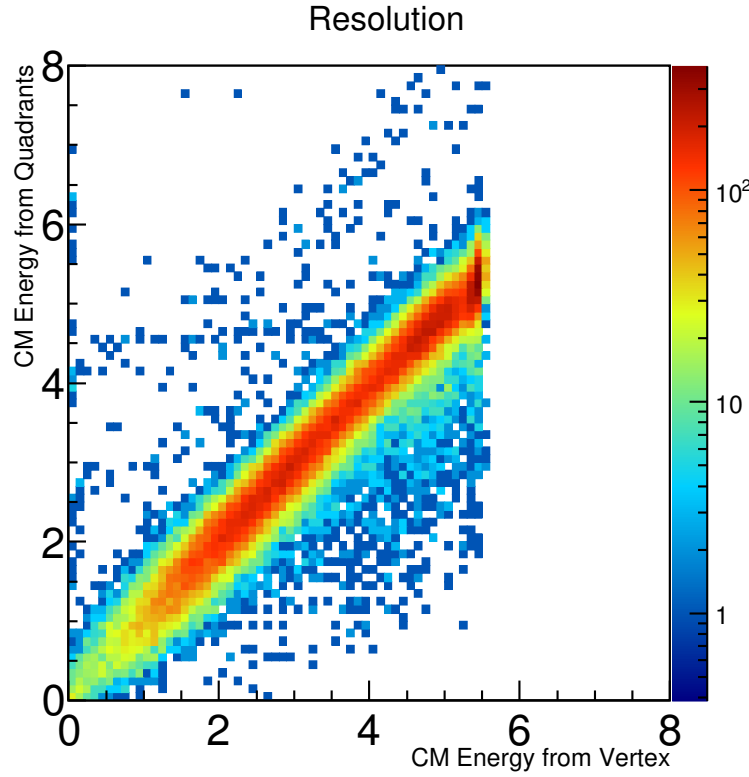


**Figure 4.5: Energy Resolution** Comparison between energy calculation methods. This plot has a full-width at half-maximum of 0.7 MeV. Based on this plot and the known full-width at half-maximum of the beam energy, the vertex method is chosen.

tered particle tracks. From this length, the energy of these outgoing particles is determined, which then sum to the energy of the beam at the reaction vertex since this is elastic scattering. This must, again, be converted to the center of mass. A comparison between these methods in Fig. 4.5. The comparison has a full-width at half-maximum (FWHM) of 0.7 MeV in the center of mass. The vertex method requires knowing the energy of the beam, while the quadrant method requires knowing the track length. The incoming beam had an energy of  $19.5 \pm 1.2$  MeV in the lab, or  $5.57 \pm 0.34$  MeV in the center of mass. Since this is lower than the resolution of the comparison plot, the vertex method is the method that was used in the analysis. This method has a firm cutoff at the beam energy, but the resolution is significantly better than the tracks method.

From the kinematics plot, the number of reactions that fall into each energy and angle bin

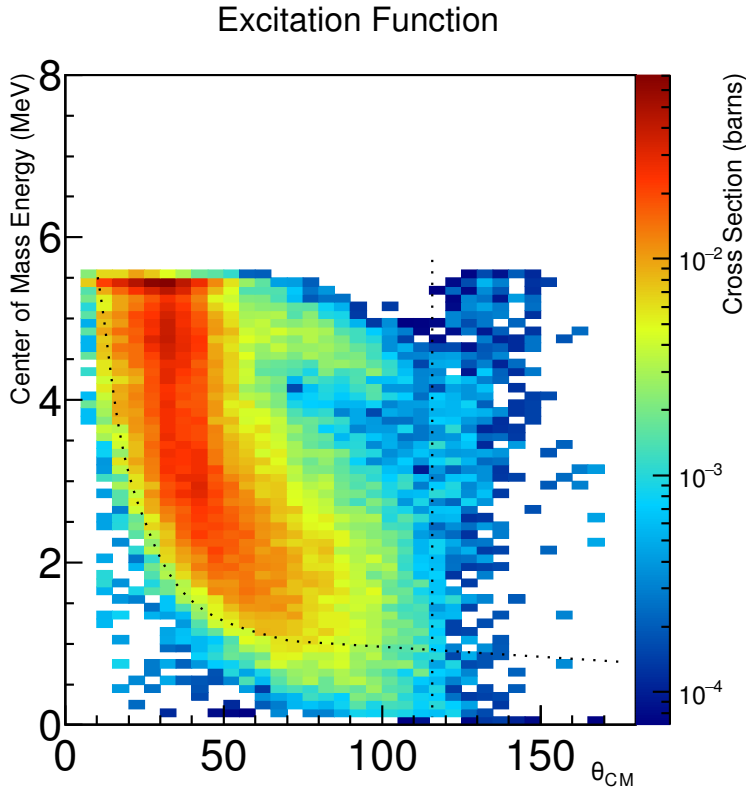


**Figure 4.6: Low-Energy Excitation Function** Note the cutoff behavior at low angles and energies as well as at high angles. The dotted line delineates the reliable region.

is known. This number of counts must then be converted to a cross section.

$$\frac{d\sigma}{d\Omega} = \frac{N}{\epsilon N_{inc} n_t \sin\theta d\theta d\phi} \quad (4.5)$$

where  $N$  is the number of counts in the bin,  $\epsilon$  is the efficiency of the detector,  $N_{inc}$  is the total number of incident particles,  $n_t$  is the number of target nuclei in the bin,  $\sin\theta$  is the sine of the angle at the center of the bin,  $d\theta$  is the width of the bin in  $\theta$  and  $d\phi$  is the width in  $\phi$ . The efficiency of the detector is calculated by the GEANT4 simulation shown in Fig. 4.3 and described above.  $n_t$  is different for every bin because a different amount of energy is deposited at each  $z$  coordinate – energy loss is not a constant.  $d\theta$  is five degrees, and  $d\phi$  is  $2\pi$  radians.

Combining the angle, energy, and cross section gives the final excitation function.

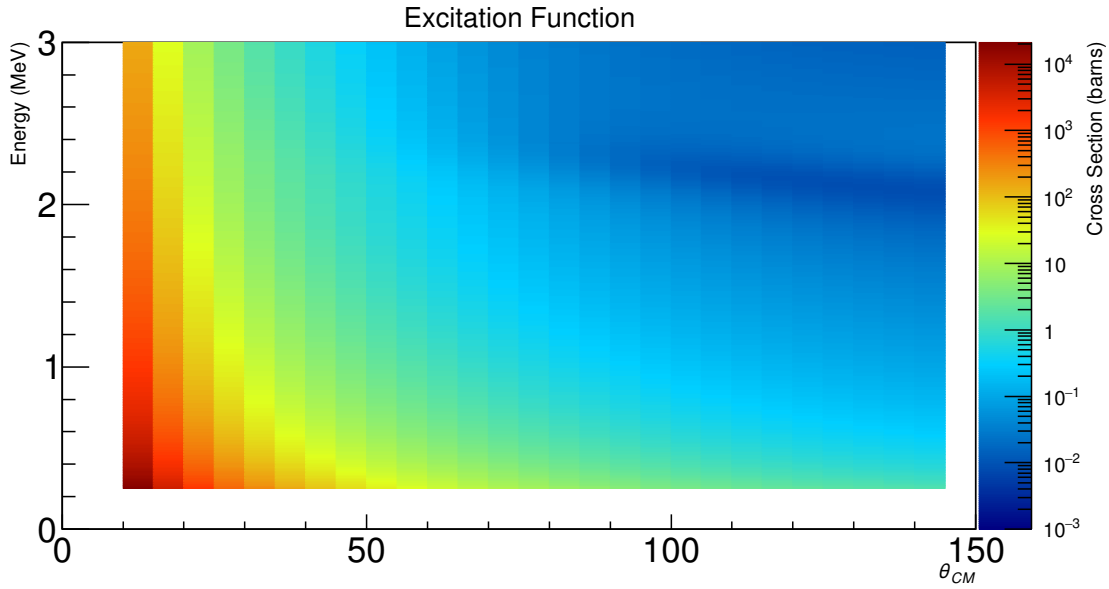


**Figure 4.7: Low-Energy R-Matrix Calculation** Theoretical cross section for a  $0^+$  state at 2.3 MeV. Note the “downward” peak above  $80^\circ$ . The calculation was performed using DSIGMAIV written by Wang Hong-Wei.

#### 4.1.4 Results and Discussion

The result of these calculations is Fig. 4.6. Most of what is visible is clearly potential scattering, or scattering that does not populate a specific resonance in  $^{14}\text{C}$  but non-resonant elastic scattering. There is a very strong cutoff at angles greater than  $150^\circ$ . This is due to the trigger conditions that exclude the central pads from the multiplicity trigger. This makes sense to prevent the beam from causing triggers, but does remove these high angles. This cutoff is visible in the acceptance calculation above. The more gentle fall off at low angles and energies and angles above  $120^\circ$  is not well-reproduced by the acceptance calculation, otherwise it would not appear in the final excitation function. This is likely a result of the trigger multiplicity being poorly calibrated.

There is a structure centered at  $(90^\circ, 4.7 \text{ MeV})$  that is consistent with the previously measured [17]  $3^-$  state. Measuring the properties of this state was not the goal of the present experiment since they were well-resolved in the previous work [17].

As discussed in Section 1.3, the expected energy for the  $0^+$  resonance was predicted to be

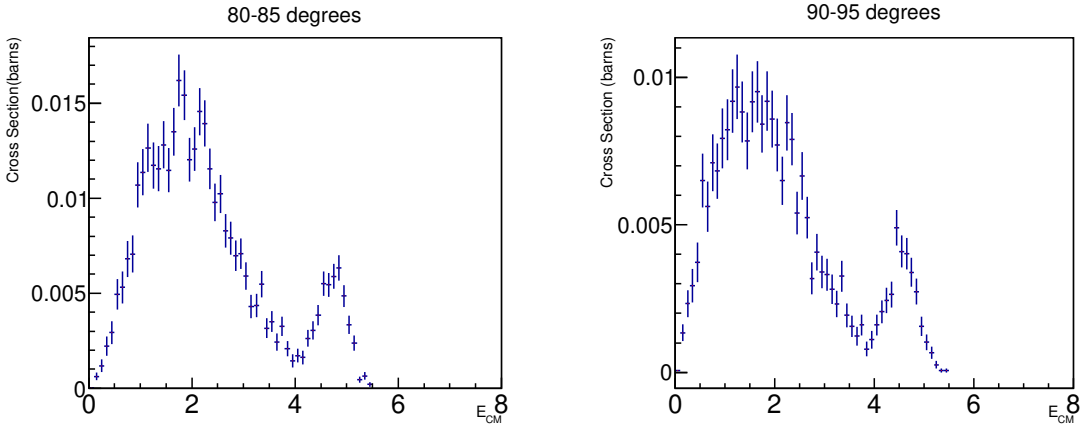


**Figure 4.8: Low-Energy Excitation Function Projections** Two angular cuts on the excitation function.

between 1.2 MeV and 3.87 MeV depending on the experiment referenced. An R-Matrix calculation assuming a resonance energy of 2.3 MeV and a spectroscopic factor of 0.5 was performed. The results of this calculation are in Fig. 4.7. The resonance behavior is evident, and begins to show at  $80^\circ$ . As shown in Fig. 4.8 there are no statistically significant changes in this excitation function as a function of angle.

The results here are in disagreement with those of Yamaguchi, *et al.* [19]. The 760 keV wide,  $0^+$  at 3.06 MeV that they measured is excluded. In the article [19], an alternative hypothesis is proposed that this state is instead a  $1^-$ . This hypothesis is neglected as it is considered a less-good fit to their data, but the present data would support this hypothesis instead, as the first Legendre polynomial has no contribution at  $90^\circ$ .

If the  $0^+$  is at the lowest-predicted energy, 1.2 MeV, its width would be 88 eV, which is below the experimental resolution of 300 keV and below the energy cutoff of this experiment.

There are only a few inelastic scattering events in this data set so they were not pursued for further analysis.

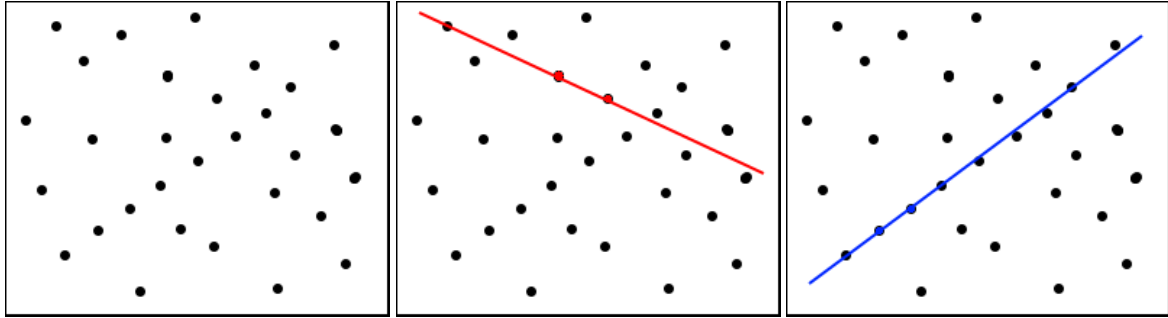


Figure 4.9: **RANSAC method** The first image shows a field of random points with a line overlaid. This is a cartoon with much more noise than would be expected from physics data. As described in the text, RANSAC chooses two points randomly. In the second picture, it chose points that do not correspond to a line through the rest of the data. Thus it can re-try until it selects points, such as those in the third image, that do correspond to a line for many points.

## 4.2 Two-body Events at High Energy

### 4.2.1 Reconstruction

In the high-energy experiment, there are both two- and three-body events. Part of the challenge of reconstructing the events from this experiment is to distinguish between these two classes of events. When there is a three-body event, it is likely that two of the tracks appear in the same quadrant of the Micromegas. Thus, the Hough space analysis from the previous section is insufficient. Instead, method called Random Sample Consensus (RANSAC) was used. [40]

RANSAC is used to find patterns within a random background. The pattern it searched for in this data was lines in three-dimensional space, but it can also be used to find planes, circles, and other geometric shapes. In order to find a line, RANSAC first randomly selects two points from all of the points available in the image. Two points is the minimum number of points to describe a line. The line that is described by these points is tested for goodness-of-fit to the rest of the points of the input. If enough of the points fit well enough to the proposed line, those points are considered to be part of that line and all of the well-fitting points are eliminated from consideration in finding future lines. If an insufficient number of points fit the described line, two more random points are chosen and the process repeats. The process ends when a given fraction of the points have been assigned to lines. An example of this process is shown in

Fig. 4.9.

As should be clear from the description, there are many parameters to optimize in implementing RANSAC effectively, namely the minimum number of points in a line, how close to a proposed line a point must be to be considered part of it, and how many points should be left after lines have been found. In this experiment the parameters were as follows: at least 3 points to be considered a line, a line must be within 1 mm of a point for that point to be associated to that line, and the calculation ends when only 1% of the initial points are left. These parameters create lots of lines that can be very close to each other. The list is first truncated to the first five lines because lines are found in order of decreasing number of points and there are at most four (beam plus three outgoing particles) tracks. This list is further reduced by applying physical constraints. It was required that all lines intersect near each other to indicate the reaction vertex, no line had an angle less than five degrees which corresponds to a beam-like track, and no line had most of its points issued exactly simultaneously (that is, with the same  $z$  value) which corresponds to a spark event.

An example event of each two- and three-body events are shown in Fig. 4.10. Each outgoing particle track is accurately reconstructed, without requiring the input of whether the event is two- or three-body.

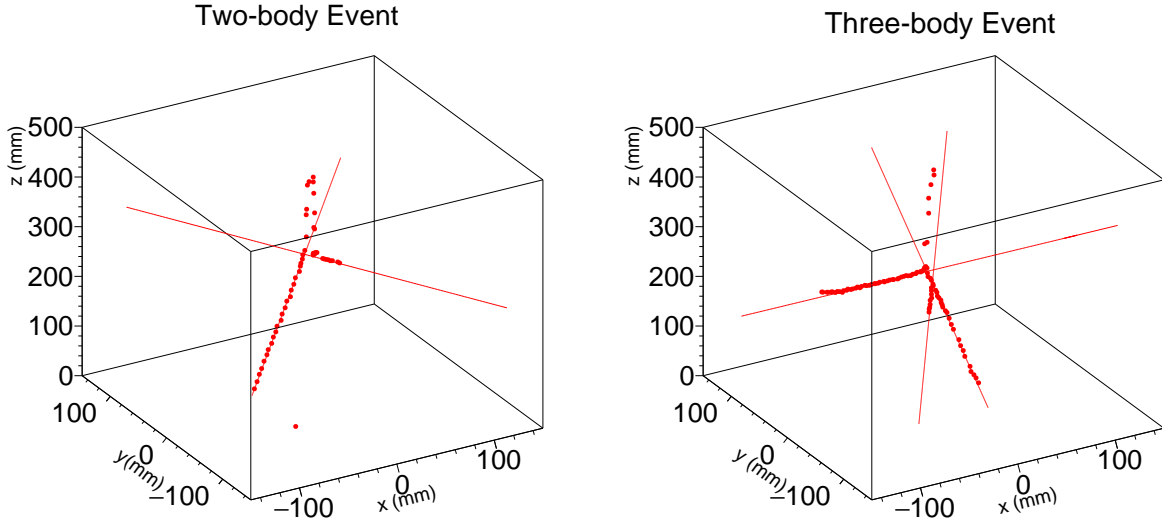


**Figure 4.10: Example RANSAC Reconstructions** Two real, reconstructed events. Points are the hit pattern collected by the TPC and the lines are the tracks reconstructed by RANSAC. The beam enters from  $z = 500$  mm and reacts. In both cases, two particles come out of the initial reaction. In the three-body case, one particle further decays. All outgoing particle tracks are reconstructed without knowing initially how many tracks there would be.

#### 4.2.2 Analysis

Similarly to the low energy experiment, once the events have been reconstructed, they are placed into an excitation function which shows the cross section for all angles and energies. This is shown in Fig. 4.11.

In this experiment, there were also a number of inelastic scattering events that could be analyzed. Making the excitation function for inelastic scattering is slightly more difficult than for elastic scattering because the center of mass angle is not as easily determined.  $\theta_{CM}$ , the center of mass scattering angle, is given by

$$\tan \theta_{CM} = \begin{cases} \alpha, & \text{if } \alpha \geq 0 \\ \pi - \alpha, & \text{otherwise} \end{cases} \quad (4.6)$$

for

$$\alpha = \frac{P_3 \sin \theta_3}{\gamma \left( P_3 \cos \theta_3 - \beta \sqrt{m_3^2 + P_3^2} \right)} \quad (4.7)$$

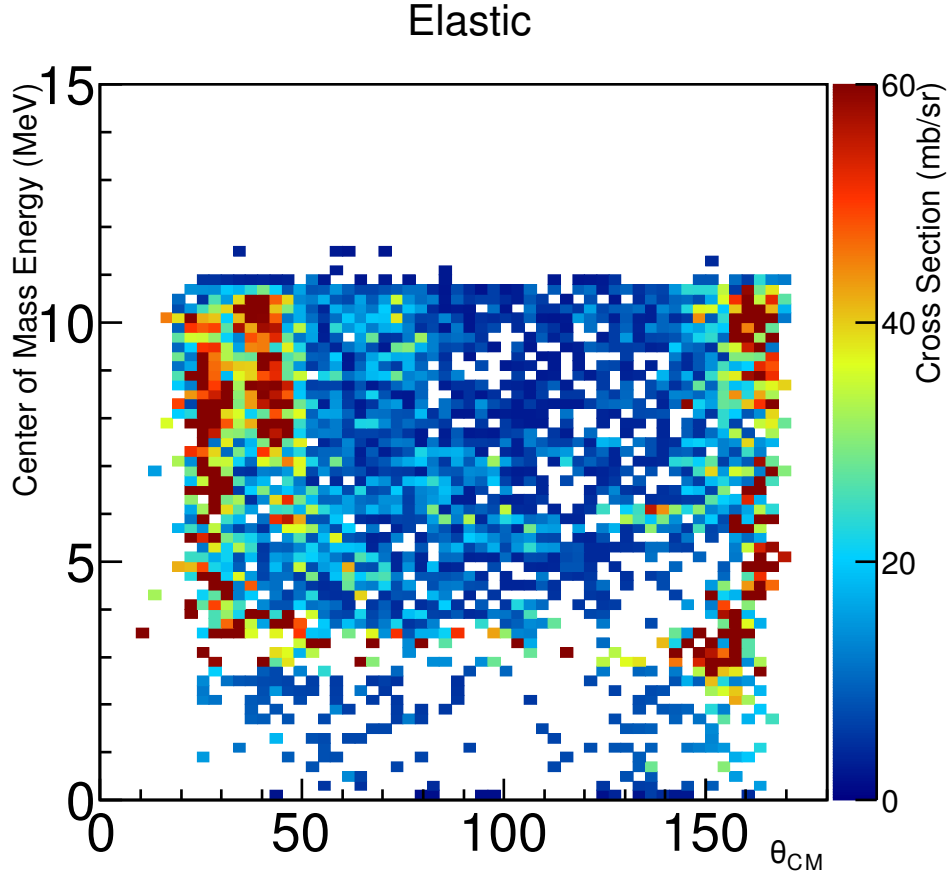


**Figure 4.11: High Energy Excitation Function** Experimental excitation function for the elastic events at high energy. The Top cut-off is at the beam energy. Angular cutoffs are due to considering all particles with angle less than  $5^\circ$  to be beam tracks.

where

$$\begin{aligned} \beta &= \frac{\sqrt{E_{\text{Lab}}^2 + 2m_1 E_{\text{Lab}}}}{m_1 + m_2 + E_{\text{Lab}}}, \\ \gamma &= \frac{1}{\sqrt{1 - \beta^2}}, \text{ and} \\ P_3 &= \frac{\sin \theta_4 \sqrt{E_{\text{Lab}}^2 + 2m_1 E_{\text{Lab}}}}{\sin(\theta_3 + \theta_4)}. \end{aligned} \quad (4.8)$$

In these equations,  $E_{\text{Lab}}$  is the lab energy of the beam particle at the time of the reaction, the  $m_i$  are the masses, and the  $\theta_i$  are the lab angles. The particles are numbered, in order from 1-4, incident  $^{10}\text{Be}$  particle, the target  $\alpha$  particle, the recoil  $\alpha$ , and ejectile  $^{10}\text{Be}$ . These equations are

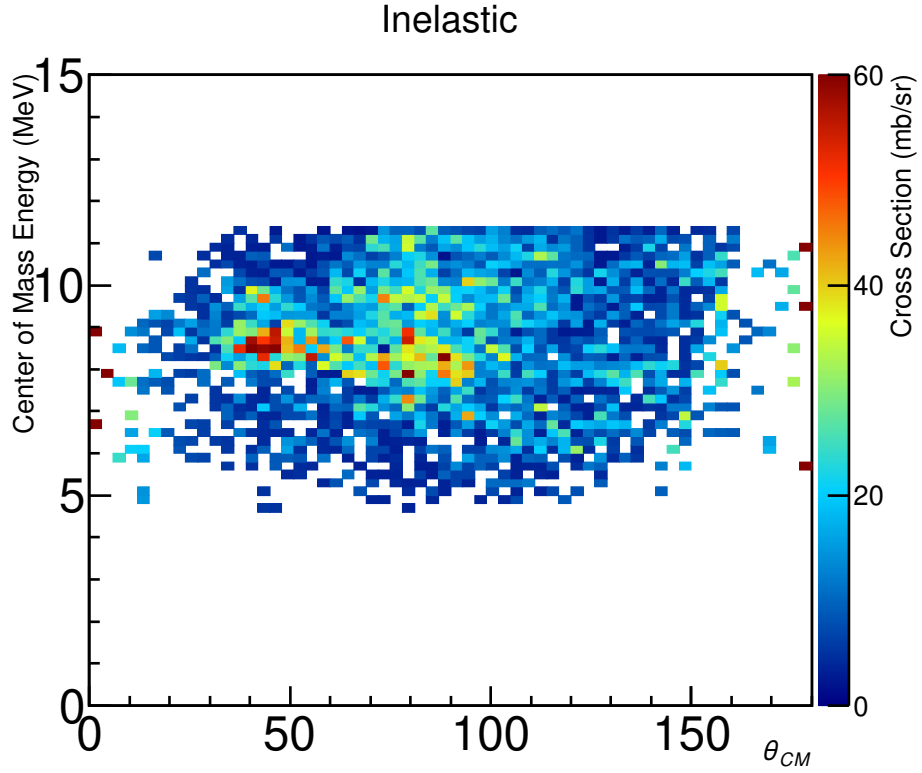


**Figure 4.12: Inelastic Scattering Excitation Function** Experimental excitation function for the inelastic events at high energy.

in natural units where  $\hbar = c = 1$ . These equations simplify to the simple expression in equation 4.3 in the case of elastic scattering because of the close relationships between energy and angle. The center of mass energy and cross section are calculated in the same way as for the elastic cases, and an excitation function is formed. The inelastic excitation function is shown in Fig. 4.12. This inelastic excitation function was functionally identical to that found by Fritsch, *et al.* [17], so no further analysis was pursued.

The elastic scattering excitation function is interpreted using an R-Matrix calculation. This calculation was performed using DSIGMAIV. DSIGMAIV takes as input the reaction parameters such as the optical model. There are a variety of optical models that can be used to describe the behavior in this experimental region. The one with the best fit to the data was chosen, which has the parameters shown in Table 4.1 and taken from [41].

$V$ (MeV)	$r$ (fm)	$a$ (fm)	$W_{vol}$ (Mev)
185.0	0.52	1.4	25.0

**Table 4.1: Optical Model Parameters** Parameters as calculated by [41], the imaginary width and radius are the same as the real ones. There is no surface or spin-orbit term.

The bare optical model does not describe the full experiment, one must add the resonant behavior to the calculation. Even if the optical model were a perfect, global fit, this would still be necessary, because in this energy domain there are states that cannot be described by simple potential scattering. Thus, DSIGMAIV also takes as input parameters energies, spins, parities, and spectroscopic factors of proposed resonances. The code then calculates the widths of these resonances and the cross section at all angles and energies, taking into account interference between the many states and the optical model potential scattering. The code was initially written by Wang Hong-Wei and updated by Wolfgang Mittig. It is designed to follow the R-Matrix method as described by Lane and Thomas [28].

The experimental excitation function was examined to find areas where the peaks and valleys correspond to the Legendre polynomials squared. As explained in section 2.3, This applies exactly for a  $0^+$  particle scattering through a single spin-parity resonance without potential scattering. This first guess is then used for a complete calculation using DSIGMAIV, including potential scattering. The DSIGMAIV calculation is repeated with a variety of energies and spectroscopic factors to find the best fit to the data. Based on these input parameters, DSIGMAIV calculates the width of the resonance and the total cross section as a function of energy and angle. This cross section can be then directly compared to the experimental excitation function from Fig 4.11. The best resonance parameters are shown in Table 4.2 and the calculated excitation function is shown in Fig 4.13.

The calculated and experimental results are more easily compared in projected slices of the excitation function. These comparisons are shown in Figs. 4.14 and 4.15.

$E_{CM}$ (MeV)	$E_{ex}$ (MeV)	$J^\pi$	$\Gamma$ (keV)	S.F.
3.0	15.0	$2^+$	290	0.3
4.7	16.7	$3^-$	270	0.2
5.6	17.6	$5^-$	100	0.4
5.9	17.9	$4^+$	210	0.2
6.5	18.5	$5^-$	200	0.4
7.0	19.0	$4^+$	340	0.2
<b>7.5</b>	19.5	( $3^-$ )	320	0.1
8.9	20.9	$5^-$	230	0.15
<b>9.5</b>	21.5	$5^-$	180	0.1
<b>10.3</b>	22.3	$5^-$	450	0.2

Table 4.2: **Calculated resonance parameters** Resonance parameters as calculated by DSIGMAIV. The resonances with bolded energies are new resonances from this work. The uncertainty in spectroscopic factor is  $\pm 0.1$  and the uncertainty in energy is  $\pm 0.2$  MeV.

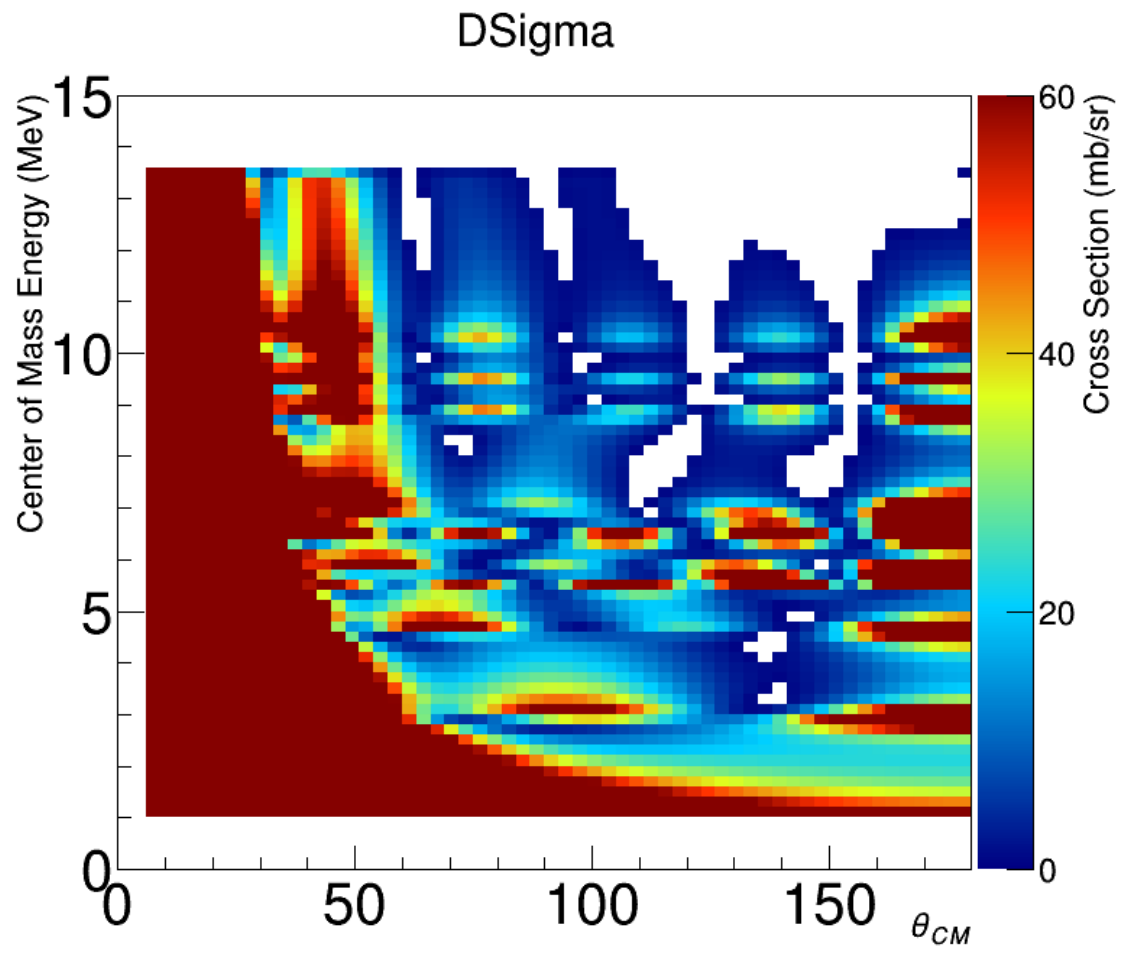
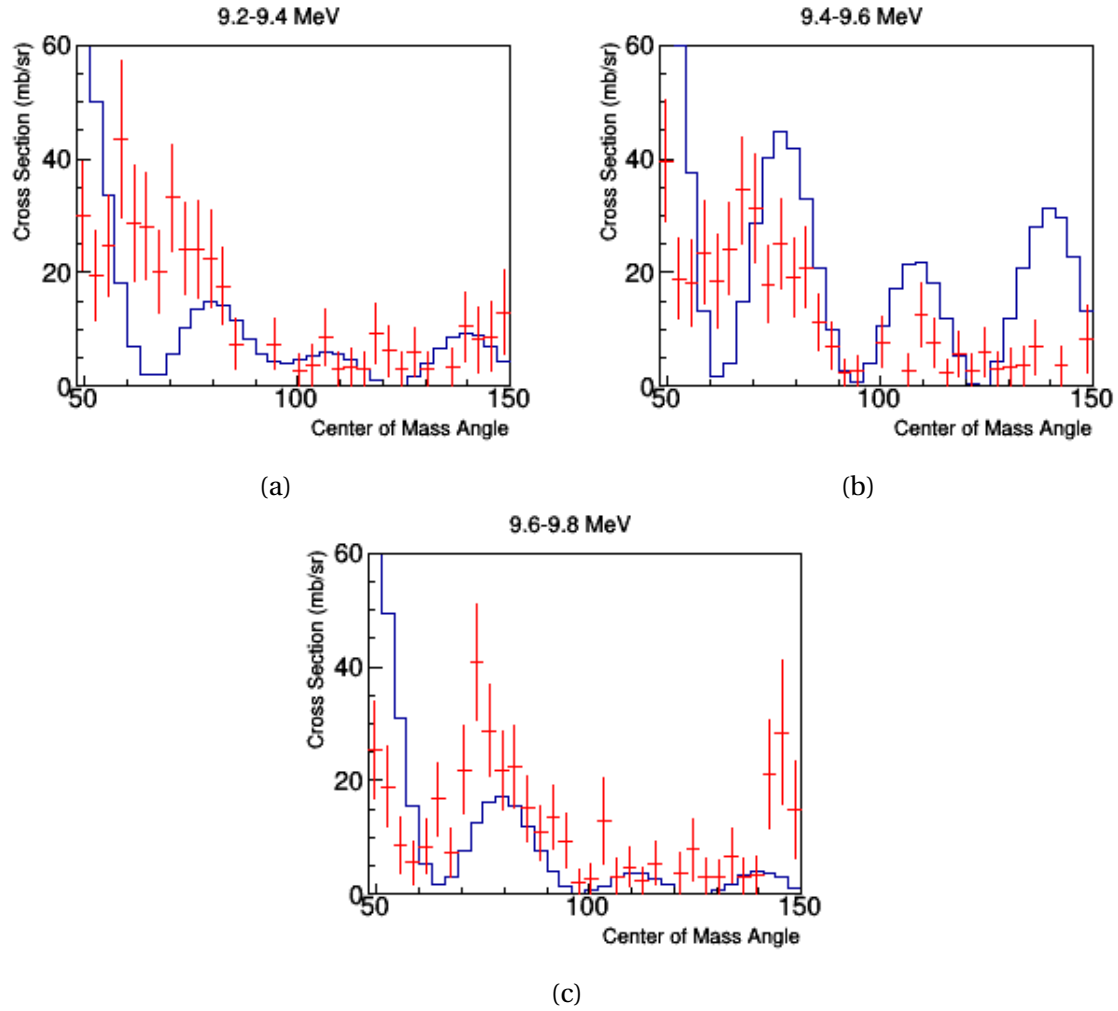
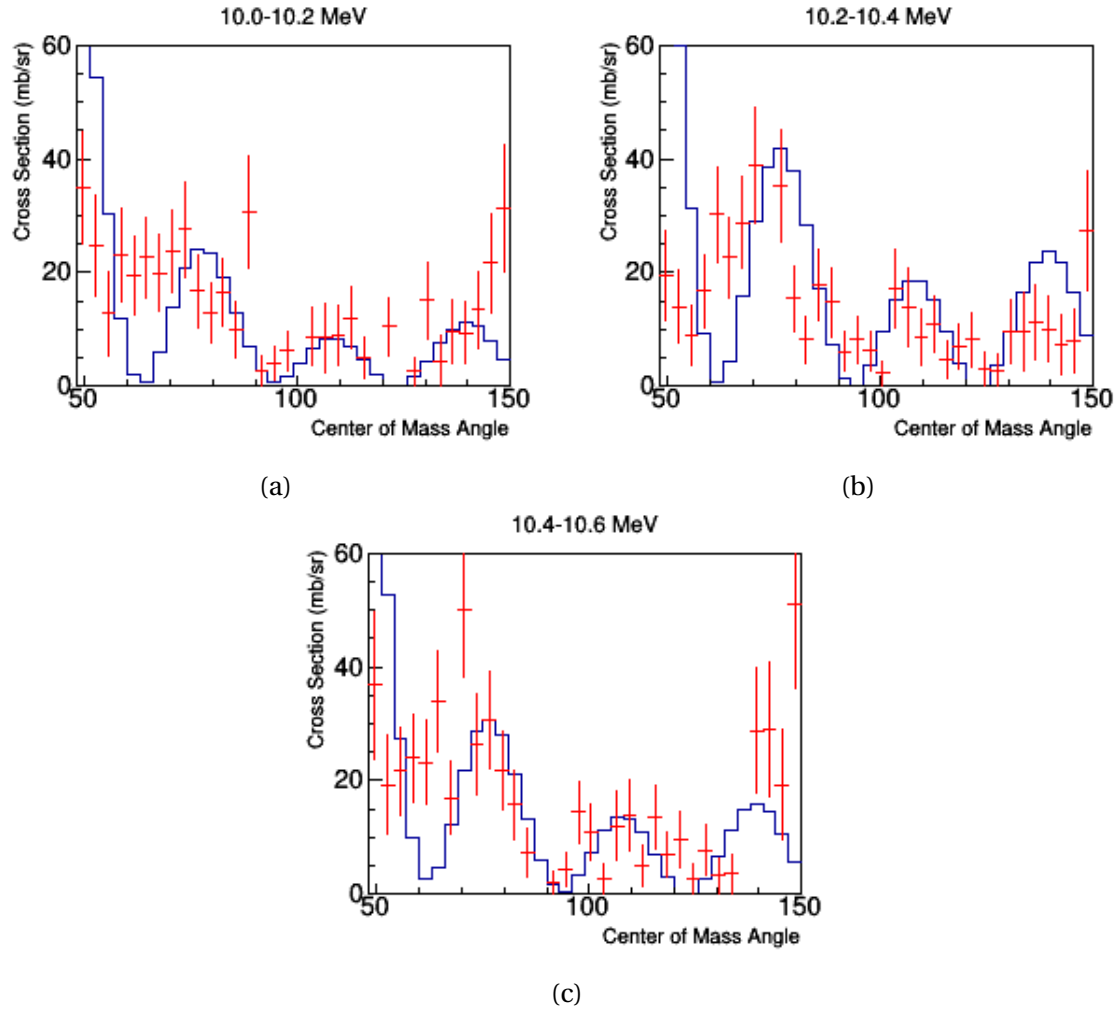


Figure 4.13: **Calculated excitation function** Excitation function calculated by DSIGMAIV, corresponding to parameters in Table 4.2.



**Figure 4.14: Comparison of Calculation and Experiment near 9.5 MeV** The DSIGMAIV calculation is shown in blue and the experimental results in red. (b) is centered on 9.5 MeV which is the location of the resonance. (a) and (b) show interference effects between the resonance and the optical model at nearby energies. A good match between calculation and experiment is seen at each energy.



**Figure 4.15: Comparison of Calculation and Experiment near 10.3 MeV** The DSIGMAIV calculation is shown in blue and the experimental results in red. (b) is centered on 10.3 MeV which is the location of the resonance. (a) and (b) show interference effects between the resonance and the optical model at nearby energies. A good match between calculation and experiment is seen at each energy.

### 4.2.3 Interpretation

The states that are well-identified are two  $5^-$  states at  $9.5 \pm 0.2$  MeV and  $10.3 \pm 0.2$  MeV. These are not part of the previously discussed linear-chain rotational bands, as those bands correspond to positive-parity states only. However, the currently accepted nuclear data [3] has states with unknown widths and  $J^\pi$  at 9.4 MeV and 10.3 MeV. The energy of these states correspond to the states that have been identified here.

In [24], a  $5^-$  state is calculated using AMD to be at 10.6 MeV with a calculated width of 29 keV. This width is much smaller than the width found in this experiment. The theoretical widths in this paper are consistently lower than those of experiment, though, so this state could be the same one. A structure for this state is not assigned in this work [24], other than to say that it does not seem to be a linear chain state, and that further theoretical study is needed. A summary of the results is shown in Fig. 4.16.

In [42], several types of two-neutron transfer are performed with the intention of finding cluster states. These transfer reactions were  $^{16}\text{O}$ ,  $^{14}\text{N}$ , and  $^{15}\text{N}$  projectiles all incident on  $^{12}\text{C}$ . They[42] find states at 9.4(2) MeV and 10.5(3) MeV. For the lower energy state, they[42] attribute

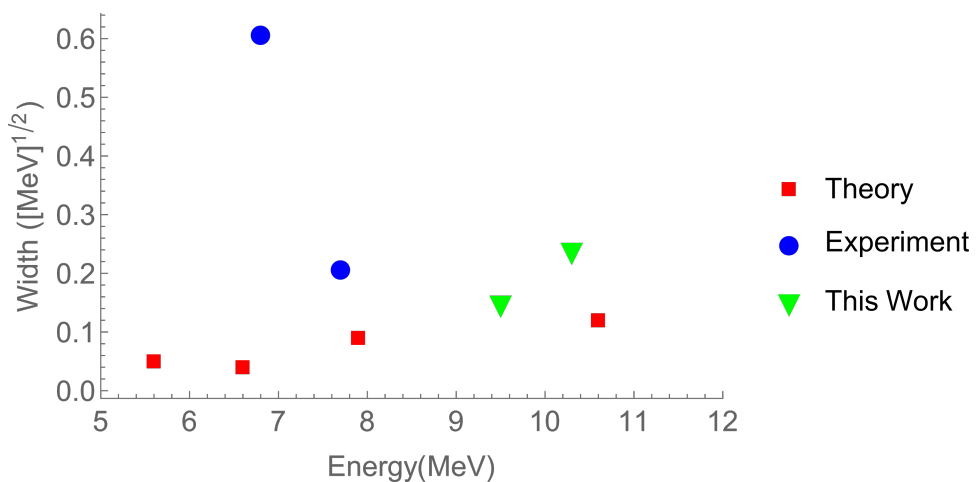


**Figure 4.16: 5<sup>-</sup> Summary** Figure adapted from [24] that shows the width of the calculated and experimental  $5^-$  states as a function of energy. Previous experiment is shown in the blue circles, theory in the red squares, and the present work in green triangles. The  $x$ -axis is the energy above the  $^{10}\text{Be} + \alpha$  threshold, and the  $y$ -axis is the  $\alpha$ -decay reduced widths, which are related to the widths calculated above by Equation 2.17.

a spin between  $2^-$  and  $7^-$ , and are uncertain whether this area represents a single state or many states nearby. For the higher-energy state, no spin assignment is given. Widths are not calculated for either state, other than to say that they are below the experimental resolution of 0.5 MeV. They [42], again, leave the further description of these states to future work.

The Gamow Shell Model calculations of Wang predict cluster states near these experimental levels. The widths are calculated as a sum between single- and multiple- $\alpha$  decays, with no branching ratio, so they are not directly comparable to those in the experiment, but are qualitatively compatible. These states primarily exist as a superposition between triangular and chain-like structures. [31]

With this in mind, the results in this section represent a step forward towards understanding these states. By assigning a spin-parity and widths to these previously-known states, the structure and decay properties in these high-lying states is very much constrained.

A resonance at 7.5 MeV is tentatively proposed. A tentatively-assigned  $2^+$  state is populated nearby in the experiments of Von Oertzen [21], but, since both assignments are tentative, a structure cannot be assigned.

The remaining states that are included in the R-Matrix calculation are consistent with previously measured states, as shown in Table 4.3. This shows that the calculation and experiment are reliable.

#### 4.2.4 Comparisons to Shell Model

This thesis focused primarily on the cluster model of the nucleus, an alternative view (which is decidedly more mainstream in the rest of nuclear physics) would be to consider these states within the shell model. The program NuShellX [43] can be used to calculate spins and parities of a nucleus using the standard shell model. In this calculation,  $^{14}\text{C}$  was considered as a  $^{10}\text{Be}$  core with excitations allowed by the two protons and two neutrons in order best reproduce the  $\alpha$ -like excitations expected by cluster structure. This is a very tight constraint. It reduces the validity of results, but allows the calculation to finish in a reasonable amount of time. For consistency

Previous Work[17–19, 21]		This Work	
Energy (MeV)	$J^\pi$	Energy (MeV)	$J^\pi$
0.47	$3^-$		
2.20	$(2^+)$		
2.49	$1^-$		
2.66	$6^+$		
2.86	$5^-$		
3.0	$2^+$	3.0	$2^+$
3.06	$0^+$		
3.18	$5^-$		
4.21	$2^+$		
4.36	$(4^+)$		
4.42	$6^+$		
4.7	$3^-$	4.7	$3^-$
4.92	$(2^+)$		
5.24	$(1^-)$		
5.29	$3^-$		
5.6	$5^-$	5.6	$5^-$
5.98	$2^+$		
6.01	$(3^-)$		
6.03	$(7^-)$		
6.21	$4^+$		
6.5	$(7^-)$	6.5	$4^+$
6.62	$5^-$		
6.82	$5^-$		
6.86	$4^+$		
7.0	$4^+$	7.0	$4^+$
7.68	$5^-$	7.5	$(3^-)$
7.9	$5^-$		
8.7	$5^-$		
8.79	$6^+$	8.9	$5^-$
		9.5	$5^-$
		10.3	$5^-$

Table 4.3: **Comparison With Previous Work** Combination of Tables 1.1 and 4.2 showing previously measured states and the states of the current work. Only states with an at-least tentative spin-parity are listed.

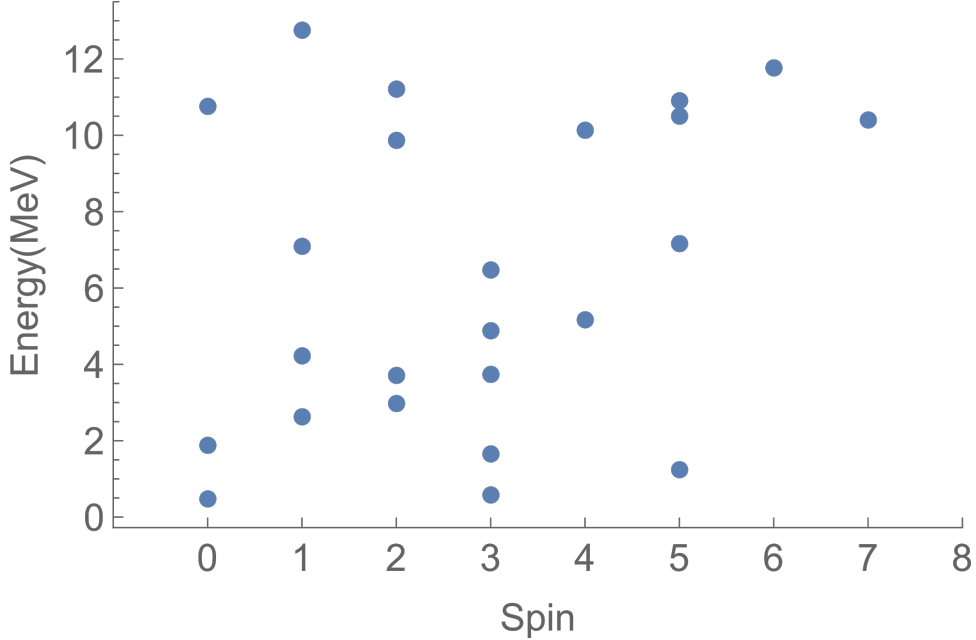


Figure 4.17: **NuShellX Calculation** Energy (above the  $^{10}\text{Be} + \alpha$  threshold) as a function of spin for levels as calculated by NuShellX. All parities for these states are  $(-1)^J$ .

with experiment, only natural-parity states were allowed, and the calculation was truncated at  $J = 10$ . The results are shown in Fig. 4.17.

The states that were calculated as being nearest the two new states from this work were  $5^-$  states at 10.5 and 10.9 MeV compared with the  $5^-$  states found in the present work at 9.5 and 10.3 MeV. For the uncertain state at 7.5 MeV, NuShellX finds a  $5^-$  at 7.2 MeV. These calculations are in general agreement with the present experimental results, showing a possible correspondence. A closer analysis of the wavefunctions would have to be undertaken to understand the possible cluster structure.

### 4.3 Three-Body Events

The three-body events that were found from RANSAC are analyzed completely independently of the two-body events. The goal of this analysis is to study the nature of the three-body decay. Recall that  $^{14}\text{C}$  is not an alpha nucleus. The three bodies in the three-body decay of  $^{14}\text{C}$  are  $\alpha$ ,  $\alpha$ , and  $^6\text{He}$ . Therefore, in  $^{14}\text{C}$  there are two types of sequential decay, “ $\alpha$ -first”, and “ $^6\text{He}$ -first”. This denotes which particle decays first from the excited  $^{14}\text{C}$ . Then, the remaining Be

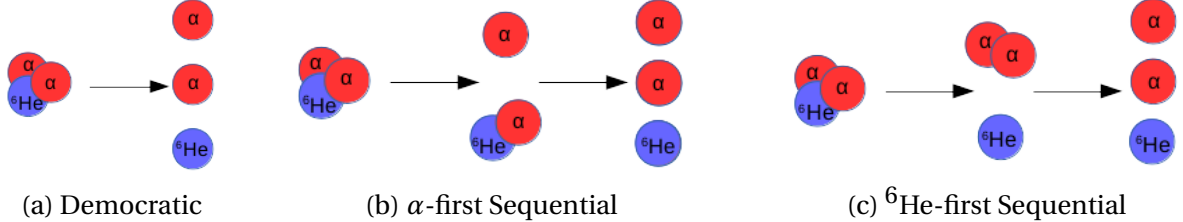


Figure 4.18: **Three-Body Channels** Cartoon showing the difference between sequential and democratic decays.

nucleus that is left decays to give the other two particles. A democratic decay corresponds to simultaneous emission of all three particles. A cartoon showing these three options is shown in Fig. 4.18 This creates differences in phase space which can be found via simulation of the different options using the GEANT4 simulation package.

### 4.3.1 Simulations

For democratic decay, the simulation proceeds as follows. A  $^{10}\text{Be}$  particle enters the detector and combines with a stationary  $\alpha$  particle in the detector gas. Their four-momenta are simply summed, so the amount of excitation energy in the resultant  $^{14}\text{C}$  depends on the depth that the  $^{10}\text{Be}$  penetrated before the interaction. This is by design. The  $^{14}\text{C}$  is not in any particular excited state, instead the full continuum is examined simultaneously. Immediately once the  $^{14}\text{C}$  has formed, a random outgoing phase space of  $\alpha$ ,  $\alpha$ , and  $^6\text{He}$  is generated via the TGenPhaseSpace method in ROOT [44]. This phase space conserves the four-momentum of the total system; the individual particles are not pairwise-correlated to each other. The trajectories of these outgoing particles are digitized to make them appear as they would in the real pAT-TPC then analyzed using the full analysis system and reconstructed using RANSAC. Then, they can be interpreted using the method described below.

In  $\alpha$ -first sequential decay, the simulation begins similarly to the simulations of scattering. The incident  $^{10}\text{Be}$  interacts with an  $\alpha$  particle, which scatters off. This time, however, the scattered  $^{10}\text{Be}$  is taken to be in an excited state that has sufficient energy to subsequently decay to  $\alpha + ^6\text{He}$ . The  $\alpha$ -decay threshold in  $^{10}\text{Be}$  is 7.409 MeV. There is an excited state at 7.542 MeV

which the outgoing  $^{10}\text{Be}$  is required to be in. This state was chosen in order to have the highest possible energy acceptance of the simulation. This maximizes the excitation energy of  $^{14}\text{C}$  that can be explored. It should also be the most probable decay path, as it is the one with the largest penetrability and phase space. Once the  $^{10}\text{Be}^*$  is created, it decays as allowed into  $\alpha + ^6\text{He}$ . Again, this outgoing phase space is generated using TGenPhaseSpace in ROOT [44]. These two particles are restricted in phase space to conserve the energy and momentum of the  $^{10}\text{Be}^*$ . This phase-space restriction is the primary distinction between sequential and democratic decay. The  $\alpha + ^6\text{He}$  particles, along with the initial outgoing  $\alpha$  are analyzed. Once the particles are generated, the digitization and analysis process is the same as for democratic decay.

In  $^6\text{He}$ -first sequential decay, the first particle to leave the reaction is not an  $\alpha$ , but a  $^6\text{He}$ . The threshold energy for this process is 26 MeV in the lab, so it is allowed at the 38 MeV beam energy in use in this experiment. In contrast to  $\alpha$ -first, the ground state of  $^8\text{Be}$  is  $\alpha$ -unbound, so there was no need to simulate that it was in an excited state. This also leaves open the possibility that the initial  $^6\text{He}$  can be simulated in its first excited state. This is less likely than the ground state emission, but as many possibilities as feasible were included in the analysis in order to test sensitivities of different assumptions.

The last option that was explored is elastic scattering. This is a two- as opposed to three-body interaction, but in choosing three-body events from the experiments, thresholds must be chosen to maximize acceptance of three-body events. This can leave open the possibility of two-body events being mis-interpreted as three-body events. Estimating the level of contamination is important.

The relative energies of all relevant energy levels is shown in Fig. 4.19.

### 4.3.2 Dalitz Plots

A “Dalitz plot” is a two-dimensional, triangular plot that is used to represent three-body decays. These plots have seen wide use in interpreting three-body decays of the Hoyle state [14, 15], as well as hadron decays in high-energy physics [45]. In nuclear physics, the axes of the plot are

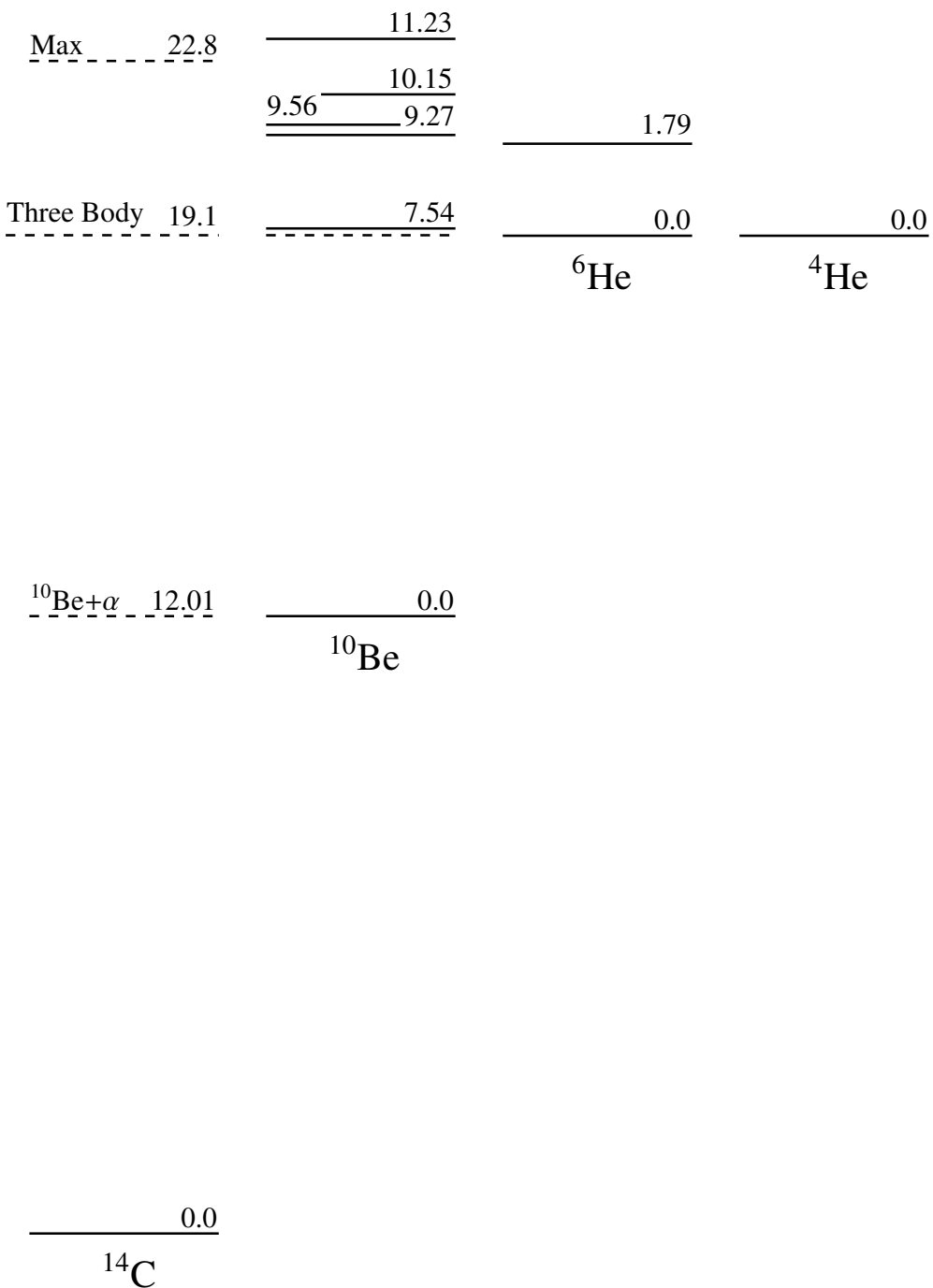


Figure 4.19: **Three-Body Decay Energy Levels** Relevant energy levels for all nuclei that can be involved in a three-body decay. The three-body decay threshold is shown as well as the maximum energy achievable in this experiment. The  $^6\text{He}$  and  $^4\text{He}$  are shown beginning at the three-body threshold, not their individual thresholds in  $^{14}\text{C}$ .

usually

$$\begin{aligned} x &= \frac{\sqrt{3}}{2} (\epsilon_2 - \epsilon_1) \\ y &= \frac{1}{2} (2\epsilon_3 - \epsilon_1 - \epsilon_2), \end{aligned} \tag{4.9}$$

where

$$\epsilon_i = \frac{E_i}{E_1 + E_2 + E_3} \tag{4.10}$$

where  $E$  is the energy of a particle and the numbering of the particles is arbitrary. This creates an equilateral triangular plot with three axes of symmetry, going from each point of the triangle to the center of the opposite side.

For the experiments here, it is not possible to reliably distinguish between an outgoing  $\alpha$  and outgoing  ${}^6\text{He}$  since their energy loss profiles are very similar. Thus, instead of using the fractional energy, the fractional range of the particles was used. This is well-correlated to energy, but is explicitly not the same thing. For simplicity, this class of plots will continue to be called Dalitz plots through the rest of this thesis.

Two examples of Dalitz plots that were created in this analysis are shown in Fig. 4.20. These plots are taking into account the experimental range resolution and reconstruction uncertainty. Several effects contribute to the uncertainty individual range measurement in the pAT-TPC: the shape and width of the pads; the ends of tracks not always being found in the reconstruction, especially where tracks have been bent due to electric field aberrations; and vertex uncertainty. With these uncertainties, both pictured channels have large central peaks with slow decays. These are the channels that should be most identifiable but are similar enough on a bin-by-bin basis, that a fitter could not easily discriminate between them.

### 4.3.3 Angular Correlation Plot

In order to find a more clear separation, instead of using a traditional Dalitz plot, an angular correlation plot was used. In these plots, the axes are  $\sin(\theta_i - \theta_j)$  for all combinations of  $i = 1, 2, 3$  and  $j = 1, 2, 3$  on each axis. This is 12 total combinations for each event. These plots are

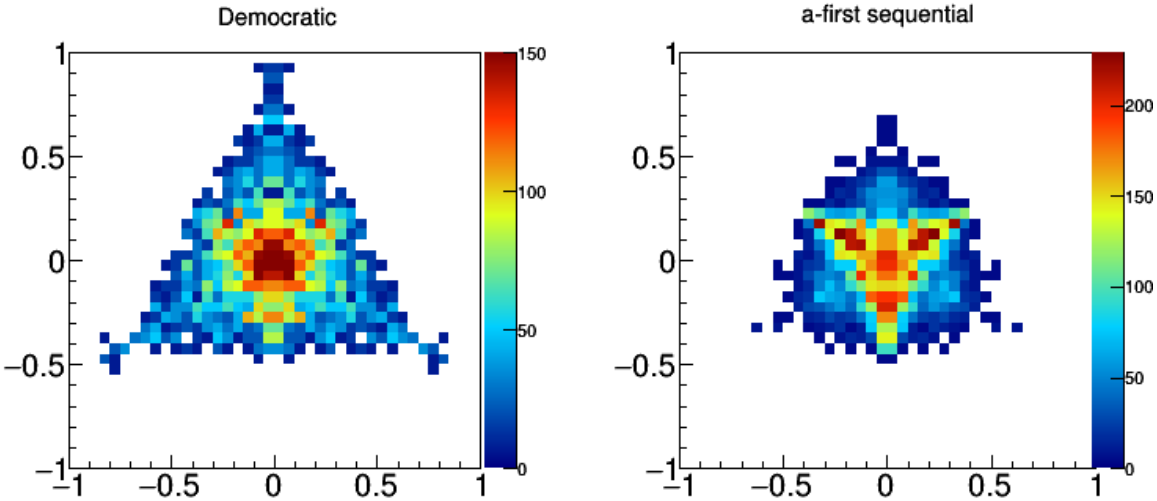


Figure 4.20: **Dalitz Plots** Dalitz plots for  $\alpha$ -first sequential and democratic decays, including experimental resolution and reconstruction.

significantly better for use in this experiment than the traditional Dalitz plot since the pAT-TPC gives a more precise measurement of angle than range, and the differences in channels are much more immediately obvious..

Based on the design of the backgammon Micromegas, it was planned to use the  $\varphi$  angle of the individual tracks to help discriminate between two- and three-body events. The  $\varphi$  angle was calculated based on the charge division between the two slices of the backgammon, as described in Section 3.1.1. This gives a different  $\varphi$  angle for each pair of pads, which should, in principle be the same, so the mean of these values is the figure of merit. For the smallest pads near the center of the detector, the difference in charges was too small to be meaningful, always reporting a very small angle, so those were excluded. Also, near the very end of the track, the amount of charge that was deposited changed rapidly due to energy loss considerations, not  $\varphi$ , so the last few points at the end of the track were also excluded from the calculation of the mean. The resolution of these calculations can be checked using elastic scattering events. The coordinate system is defined such that each quadrant starts at  $0^\circ$  and ends at  $90^\circ$  as the circle was traversed counter-clockwise. This way, tracks that are part of the same two-body elastic scattering event should have the same  $\varphi$  angle. This was tested with a selection of two-body

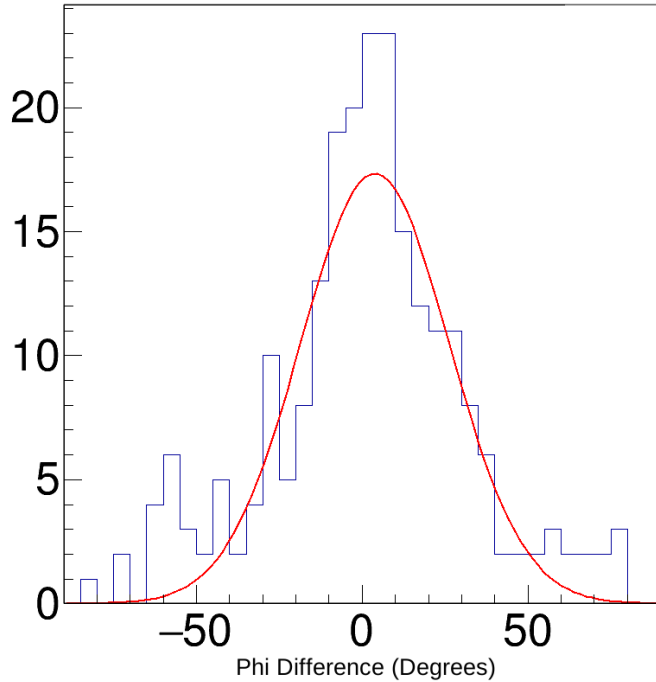


Figure 4.21:  **$\varphi$  Resolution** Histogram of the difference between the measured  $\varphi$  angle for two tracks of known two-body events. The blue line is the data and the red line is a Gaussian fit, which has a  $\sigma$  of  $22.3^\circ$ .

events as shown in Fig. 4.21. The difference in phi angle was fit with a Gaussian which had a  $\sigma$  of  $22.3^\circ$ . This can be cut in half, since one would usually use the absolute value of the difference between the two measurements, but even a resolution of  $11^\circ$  is insufficient to be used as a an experimentally measured significant variable.

A strong acceptance limitation is observed in the simulated angular correlation plots. In order to obtain a match between simulation and experiments, many cuts were included in the simulation that were necessarily present in experiment. Events which had at least one track that was very small were eliminated. These tracks would have fewer than three hit points. These tracks are too short to be reconstructed. Events were removed based on angle considerations in two distinct classes: those that had tracks with very small scattering angles that could not be distinguished from the beam, and those that had two or more tracks with very similar scattering angle which would taken as the same track. Since the  $\varphi$  angle was not usable as discrimination

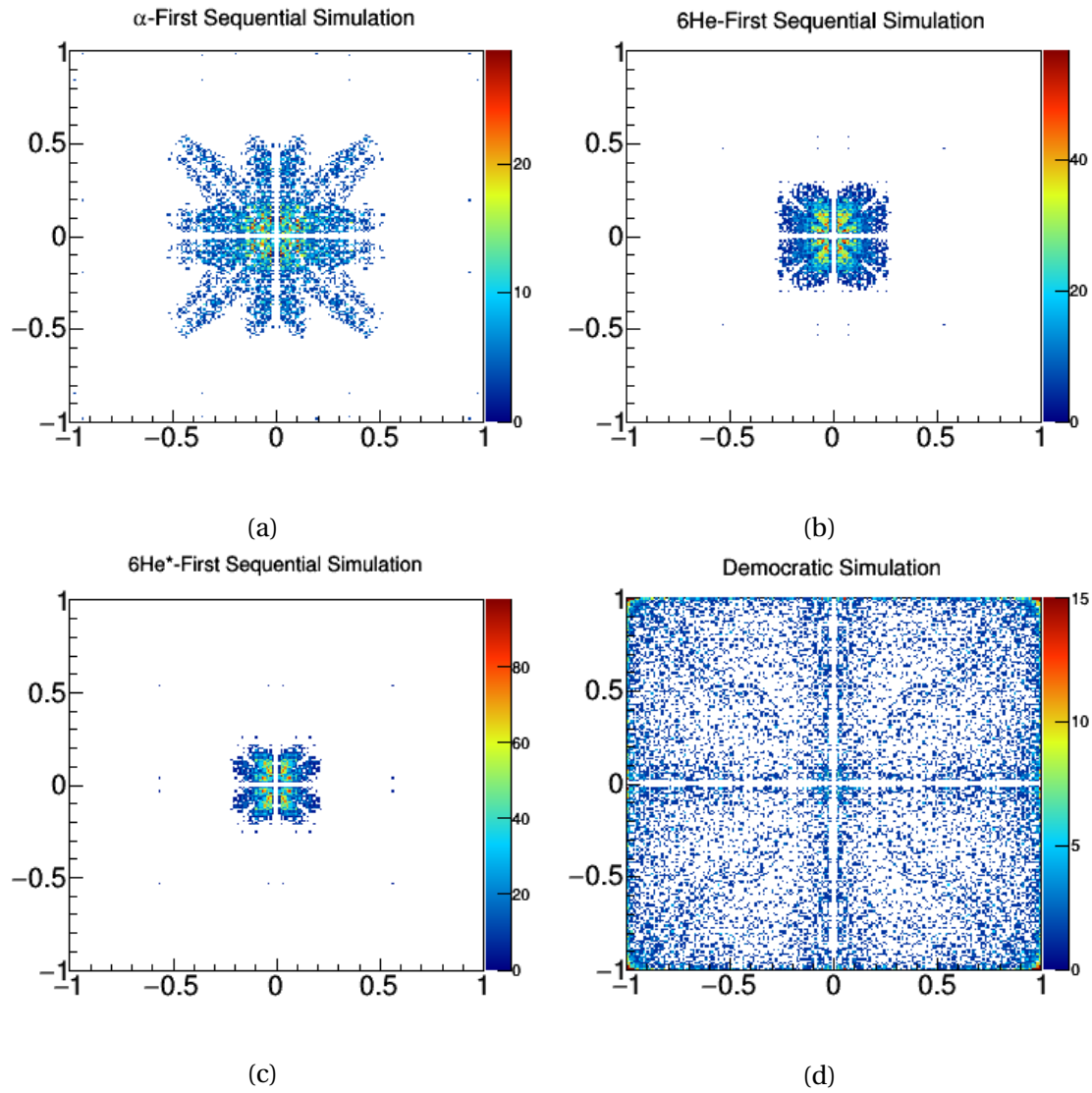
Lab Energy (MeV)	28-30	30-32	32-34	34-36	36-38
democratic	0.40	0.31	0.24	0.28	0.16
$\alpha$ -first	0.36	0.29	0.23	0.14	0.13
${}^6\text{He}$ -first	0.33	0.34	0.21	0.21	0.10
${}^6\text{He}^*$ -first	0.14	0.31	0.17	0.29	0.21

Table 4.4: **Three-Body Acceptance** Acceptance of three-body decays as a function of energy.

between two- and three-body events, total charge deposited was used. This is a useful consideration because the binding energy, that is not turned into kinetic energy and therefore not part of the energy deposited by the particles in the reaction, is greater in the three-body case. In order to have a meaningfully determined total charge deposited, only events for which no track leaves the detector were analyzed. The final acceptance also includes the reconstruction efficiency. Taken all together, these cuts are quite important. The number of analyzable events was approximately 25% of the total number of simulated events. A full account of acceptance both in total and in energy slices is show in Table 4.4.

There is at least 60% acceptance loss due to short, small angle, or same angle tracks. The additional losses, like removing tracks that leave the detector or fail to reconstruct are comparatively smaller.

One advantage of these sharp cuts is that only 0.2% of simulated two-body events were able to pass the conditions. Since the total number of three body events is approximately 10% as large as the number of two-body events, this is a total contribution of approximately 2%. This level is well below the statistical reach of the present experiment, so further analysis neglected this contribution. Additionally, the angular correlation plot for the democratic channel where all out-going particles are in their ground state and the democratic channel where the  ${}^6\text{He}$  is in its first excited state were identical. Thus, the four remaining channels to be fit across are:  $\alpha$ -first sequential decay,  ${}^6\text{He}$ -first sequential decay,  ${}^6\text{He}^*$ -first sequential decay, and democratic decay. The angular correlation plots for these channels is shown in Fig. 4.22 and the experimental plot is shown in Fig. 4.23.



**Figure 4.22: Simulated Angular Correlation Plots** Angular correlation plots for all simulated channels. The axes are  $\sin(\theta_i - \theta_j)$  for all combinations of particle number  $i$  and  $j$  over the full energy range.

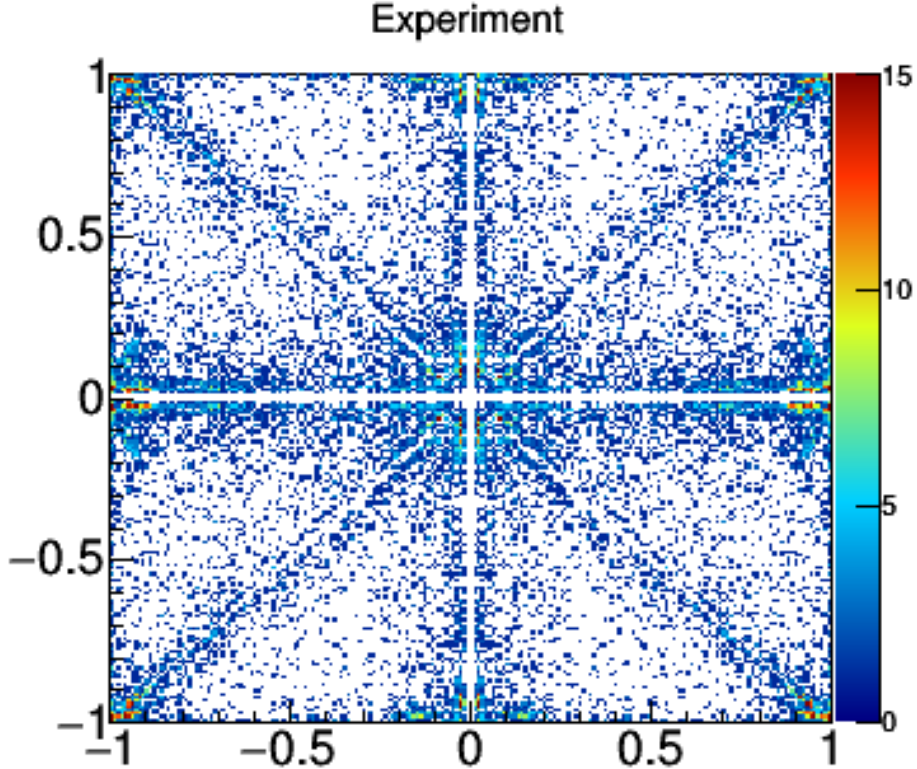


Figure 4.23: **Experimental Angular Correlation Plot** Angular correlation plot for experimental events. The axes are  $\sin(\theta_i - \theta_j)$  for all combinations of particle number  $i$  and  $j$ .

#### 4.3.4 Analysis and Results

The experimental angular correlation plot is then fitted by the simulated ones. The fit function used was of the form

$$f(x, y) = k_1 g_1(x, y) + k_2 g_2(x, y) + k_3 g_3(x, y) + (1 - (k_1 + k_2 + k_3)) g_4(x, y) \quad (4.11)$$

where the  $k_i$  are the variational fit parameters that are constrained between 0 and 1 and the  $g_i$  are the simulated histograms shown in Fig 4.22. The most important thing to note from this equation is that the fit is not directly varying the parameters for  $g_4$ , which was the  ${}^6\text{He}^*$ -first sequential decay. Because of this, the error estimates on the fraction of events which correspond to this are dependent on the other three parameters. The fit performed using a log-likelihood fitter from MINUIT as built in to ROOT and the Minos method of error estimation [44].

Lab Energy (MeV)	28-30	30-32	32-34	34-36	36-38
democratic	0.12	0.17	0.11	0.19	0.41
$\alpha$ -first	0.15	0.22	0.22	0.13	0.15
${}^6\text{He}$ -first	0.19	0.41	0.36	0.39	0.22
${}^6\text{He}^*$ -first	0.51	0.19	0.29	0.27	0.21

**Table 4.5: Three-Body Fit Results** The fitted fraction of events in each energy bin that correspond to each type of three-body decay. The error on these values is discussed in the text.

The fit was first performed with an equal number of simulated points for all energies from the threshold of 26 MeV up to the experimental limit of 38 MeV total lab energy. This does not take into account the energy dependence of the relative probabilities. The fit was therefore also performed in bins of 2 MeV to allow for different population probabilities at different energy levels. This limit was chosen to keep a reasonable number of experimental statistics in each bin. Despite that, the fit was non-convergent for the 26-28 MeV bin. The results of the fit, after acceptance correction are shown in Table 4.5.

The statistical error from the fit was at most 0.02, and the Poisson uncertainty in the number of experimental points in each bin was at most 0.02. These statistical errors are dwarfed by the systematic error as caused by the acceptance effects described above. The value of this systematic error is difficult to quantify. The fit was completed with a variety of cuts and over different domains, from which the systematic error is estimated at 0.1. All together, these errors mean that discriminating between the classes of sequential decay is not statistically meaningful. The primary question is still, however, whether there is any democratic decay. For energy values below 34 MeV, the amount of democratic decay is consistent with zero. However, for higher energy bins, there is a statistical significant amount of democratic decay. This is a unique result as compared with the Hoyle State which, as discussed in Section 1.3.1, has a very small to near-zero fraction of democratic decays.

This result is the consistent with the one given by the Gamow Shell Model calculations of Wang where the sequential was much more strongly populated at low energies. [31] See the discussion in Section 2.4 for more details.

## CHAPTER 5

## CONCLUSIONS

### 5.1 Future Work

The AT-TPC project is continuously evolving, both in terms of the detector itself and the group's ability to analyze events from this class of detector. As mentioned previously in this thesis, the full scale AT-TPC has been in operation for several years now operating a parallel experimental program to that of the pAT-TPC. Both detectors are benefiting from current and future improvements in both classes.

#### 5.1.1 Detector Improvements

This work was resolution-limited in several ways. The two-body cases had resolution limits based on the uncertainty in the energy of the beam. This is difficult to overcome in the *TwinSol* facility, but is greatly improved if re-accelerated beams are used, such as in TRIUMF-ISAC or ReA3 at NSCL/FRIB. Other resolution challenges, such as position resolution of tracks and outgoing particle identification can be helped, primarily by improving the detection system. The Micromegas as used in these experiments with 256 channels, while good, does not have sufficient resolving power to take advantage of the full power of the detection system. To that end, a new Micromegas for the pAT-TPC is was recently developed. This new detection plane has 2048 small, triangular pixels instead of the wide backgammon stripes. With this pad plane, the  $\varphi$  angle will be evident for all particles, and the energy deposited will be more well-localize. An image of this new pad plane is shown in Fig 5.1.

Additional resolution improvements have come from improving the amplification device to reduce the need for a quench gas. In the experiments in this work, the Micromegas was used alone as a gas amplifier. The AT-TPC group has been exploring other amplification schemes mostly relying on Thick GEM amplifiers. THGEMs, as they are often called, consist of a G-10

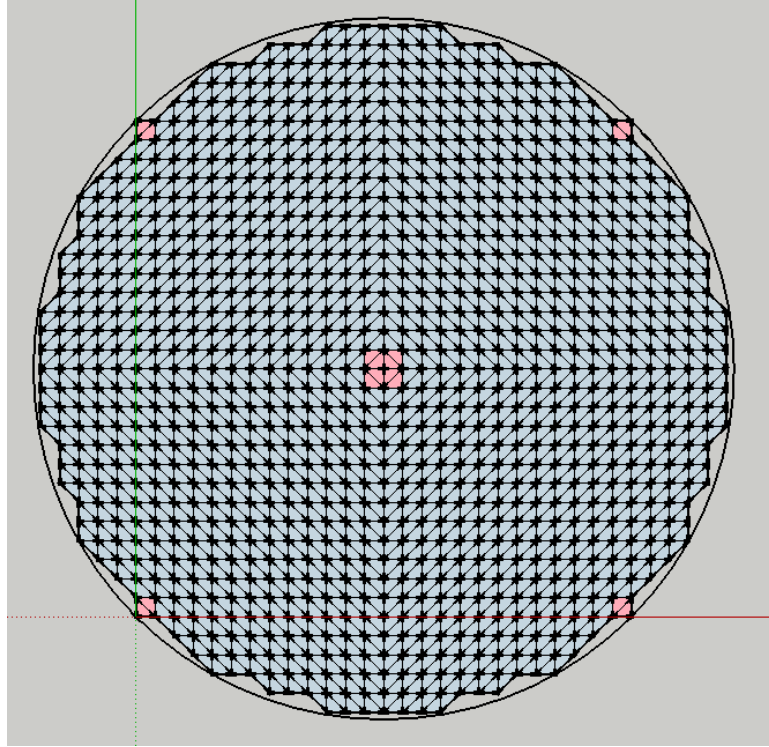


Figure 5.1: **New Micromegas Design** Improved design that with greater granularity.

plate coated in copper that has holes of diameter  $\sim 0.7$  mm drilled with pitch between 1.5 and 4 mm depending on the particular device. A voltage is applied between the top and bottom surface of the THGEM causing an electron avalanche inside of the hole as the primary electrons pass through. [46] Several THGEMs can be used simultaneously to give even more amplification. Alternatively, a multi-layer THGEM, which can have two or three layers of G-10 separated by copper, can act alone to give similar amplification as several independent THGEMs in a single device. [47] This is an area of ongoing improvement for the detector system. Currently, the pAT-TPC has two single-layer THGEMs which can be installed together, which has allowed operation with pure Helium gas in recent experiments.

Both of these improvements were operational in a recent experiment performed at TRIUMF with the pAT-TPC for which analysis is ongoing.

The final detector improvement is actually an entirely new detector being planned as a collaboration between the AT-TPC group at the NSCL and the HELIOS group from Argonne National Lab. This new detector, called SOLARIS, will be used in the forthcoming ReA6 accelerator

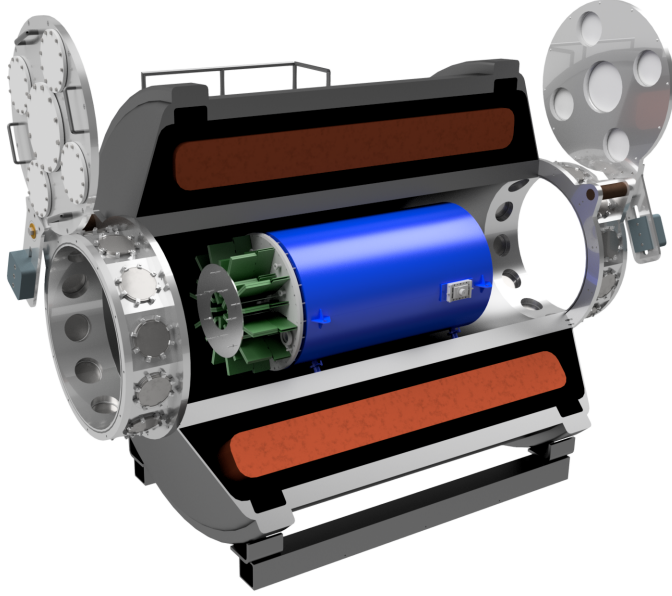


Figure 5.2: **SOLARIS** AT-TPC as mounted inside the SOLARIS solenoid.

at both the NSCL and FRIB. A design image is shown in Fig. 5.2. It consists of a 4 T solenoid magnet in which the AT-TPC can be mounted. This is a factor of two improvement of magnetic field compared to the current solenoid for the AT-TPC. This detector will be able to take full advantage of the rare, weak beams that will result from FRIB and ReA6. [48]

### 5.1.2 Analysis Improvements

The other prong of future work is improving analysis efficiency. One method of doing this is using machine learning to classify events instead of the heuristics and fitters that were used in this work. Kuchera, *et al.* [49] have been working on implementing a machine learning algorithm to apply to tracks in the full scale AT-TPC. The algorithm in question is of a convolutional neural network that has been trained to 100% efficiency on simulated data. This same network is then used in a transfer learning task, meaning that even though it was trained on simulated data, it can be applied on experimental data. Currently, when used to analyze experiment e13306b from the AT-TPC, the algorithm has a precision of 90%. At present, this algorithm is only a classifier and some kind of fitting or clustering on the classified track would still be necessary in

order to recover physics variables.

Pattern recognition and machine learning are broad, active areas of research which the AT-TPC group will continue to benefit from and contribute to in order to select data of interest from noisy environments and fit to find quantifiable, physically-meaningful information.

## 5.2 Conclusion

The experiments in this work were built upon a rich history of many cluster studies in a variety of nuclei. Recent AMD Calculations predicted a variety of cluster states in  $^{14}\text{C}$  which merited experimental exploration. These experiments used the pAT-TPC detector which has a thick target, large angular acceptance, and can explore the full excitation function at a single beam energy. This makes it a particularly well-suited detector to this kind of study with radioactive beams.

There are two primary results from this thesis. First, there are two states with newly measured spin and parity of  $5^-$  at 9.5 and 10.3 MeV above the  $^{10}\text{Be} + \alpha$  threshold. The structure of these states was discussed and explored with a variety of calculations, theoretical methods, and comparisons to previous experimental results. Based on a three-body Gamow Shell Model calculation, these states have a unique cluster structure that exists in a superposition of linear chain and triangular shapes. Future work is needed to clearly elucidate these structures.

The other result is that there is an increasing amount of democratic decay at high excitation energy in  $^{14}\text{C}$ . This result was found by simulating possible three-body decay models and comparing those to experimental results using a modified Dalitz method. This was interpreted according to and found consistent with the predictions of the Gamow Shell Model calculation. Future experiments should be planned that include measuring the three-body decay contributions from individual states instead of the continuum. The upgraded pAT-TPC is well-adapted to such studies.

The experiments in this work did not confirm the properties of the  $0^+$  rotational band head that is expected a few MeV above the  $^{10}\text{Be} + \alpha$  threshold. This work disagreed with a previous

study that attributed a  $0^+$  to a state at 3.06 MeV. Instead, our results are compatible with their alternative hypothesis of a  $1^-$  state. Future experiments should be performed that reach lower energies with high resolution to find this state that is important for the cluster structure.

The experiments in this work fit nicely into the tapestry of current theoretical and experimental research, and suggest future pathways for exploration. Future cluster studies will continue to enhance our knowledge and understanding of the nuclear force and the structure of all nuclei.

## **BIBLIOGRAPHY**

## BIBLIOGRAPHY

- [1] G. F. Knoll, *Radiation detection and measurement* (John Wiley, 2000).
- [2] K. S. Krane and D. Halliday, *Introductory nuclear physics* (Wiley, 1988).
- [3] F. Ajzenberg-Selove, “Energy levels of light nuclei  $A = 13\text{--}15$ ”, Nuclear Physics A **523**, 1–196 (1991).
- [4] TUNL Nuclear Data Evaluation Project, *Energy Level Diagram, 14C*, Available at [http://www.tunl.duke.edu/nucldata/figures/14figs/14\\_06\\_1991.pdf](http://www.tunl.duke.edu/nucldata/figures/14figs/14_06_1991.pdf), 1991.
- [5] P. Maris, J. P. Vary, P. Navrátil, W. E. Ormand, H. Nam, and D. J. Dean, “Origin of the anomalous long lifetime of  $^{14}\text{C}$ .”, Physical Review Letters **106**, 202502 (2011).
- [6] L. R. Hafstad and E. Teller, “The Alpha-Particle Model of the Nucleus”, Physical Review **54**, 681–692 (1938).
- [7] F. Hoyle and F., “On Nuclear Reactions Occuring in Very Hot STARS.I. the Synthesis of Elements from Carbon to Nickel.”, The Astrophysical Journal Supplement Series **1**, 121 (1954).
- [8] M. Freer, “The clustered nucleus—cluster structures in stable and unstable nuclei”, Reports on Progress in Physics **70**, 2149–2210 (2007).
- [9] K. Ikeda, N. Takigawa, and H. Horiuchi, “The Systematic Structure-Change into the Molecule-like Structures in the Self-Conjugate  $4n$  Nuclei”, Progress of Theoretical Physics Supplement **E68**, 464–475 (1968).
- [10] R. Bijker and F. Iachello, “Evidence for Tetrahedral Symmetry in  $O_{16}$ ”, Physical Review Letters **112**, 152501 (2014).
- [11] M. Freer and H. Fynbo, “The Hoyle state in  $^{12}\text{C}$ ”, Progress in Particle and Nuclear Physics **78**, 1–23 (2014).
- [12] X. G. Cao, E. J. Kim, K. Schmidt, K. Hagel, M. Barbui, J. Gauthier, S. Wuenschel, G. Giuliani, M. R. D. Rodriguez, S. Kowalski, H. Zheng, M. Huang, A. Bonasera, R. Wada, N. Blando, G. Q. Zhang, C. Y. Wong, A. Staszczak, Z. X. Ren, Y. K. Wang, S. Q. Zhang, J. Meng, and J. B. Natowitz, “Examination of evidence for resonances at high excitation energy in the  $7\alpha$  disassembly of  $\text{Si } 28$ ”, Physical Review C **99**, 014606 (2019).
- [13] E. Epelbaum, H. Krebs, T. A. Lähde, D. Lee, and U.-G. Meißner, “Structure and rotations of the Hoyle state.”, Physical Review Letters **109**, 252501 (2012).

- [14] R. Smith, T. Kokalova, C. Wheldon, J. E. Bishop, M. Freer, N. Curtis, and D. J. Parker, “New Measurement of the Direct  $3\alpha$  Decay from the C 12 Hoyle State”, *Physical Review Letters* **119**, 132502 (2017).
- [15] D. Dell’Aquila, I. Lombardo, G. Verde, M. Vigilante, L. Acosta, C. Agodi, F. Cappuzzello, D. Carbone, M. Cavallaro, S. Cherubini, A. Cvetinovic, G. D’Agata, L. Francalanza, G. L. Guardo, M. Gulino, I. Indelicato, M. La Cognata, L. Lamia, A. Ordine, R. G. Pizzone, S. M. R. Puglia, G. G. Rapisarda, S. Romano, G. Santagati, R. Spartà, G. Spadaccini, C. Spitaleri, and A. Tumino, “High-Precision Probe of the Fully Sequential Decay Width of the Hoyle State in C 12”, *Physical Review Letters* **119**, 132501 (2017).
- [16] H. Zheng, A. Bonasera, M. Huang, and S. Zhang, “Decay modes of the Hoyle state in C12”, *Physics Letters B* **779**, 460–463 (2018).
- [17] A. Fritsch, S. Beceiro-Novo, D. Suzuki, W. Mittig, J. J. Kolata, T. Ahn, D. Bazin, F. D. Beccetti, B. Bucher, Z. Chajecki, X. Fang, M. Febbraro, A. M. Howard, Y. Kanada-En’yo, W. G. Lynch, A. J. Mitchell, M. Ojaruega, A. M. Rogers, A. Shore, T. Suhara, X. D. Tang, R. Torres-Isea, and H. Wang, “One-dimensionality in atomic nuclei: A candidate for linear-chain  $\alpha$  clustering in C 14”, *Physical Review C* **93**, 014321 (2016).
- [18] M. Freer, J. D. Malcolm, N. L. Achouri, N. I. Ashwood, D. W. Bardayan, S. M. Brown, W. N. Catford, K. A. Chipps, J. Cizewski, N. Curtis, K. L. Jones, T. Munoz-Britton, S. D. Pain, N. Soić, C. Wheldon, G. L. Wilson, and V. A. Ziman, “Resonances in  $^{14}\text{C}$  observed in the  $^{4}\text{He}(^{10}\text{Be},\alpha)^{10}\text{Be}$  reaction”, *Physical Review C* **90**, 054324 (2014).
- [19] H. Yamaguchi, D. Kahl, S. Hayakawa, Y. Sakaguchi, K. Abe, T. Nakao, T. Suhara, N. Iwasa, A. Kim, D. H. Kim, S. M. Cha, M. S. Kwag, J. H. Lee, E. J. Lee, K. Y. Chae, Y. Wakabayashi, N. Imai, N. Kitamura, P. Lee, J. Y. Moon, K. B. Lee, C. Akers, H. S. Jung, N. N. Duy, L. H. Khiem, and C. S. Lee, “Experimental investigation of a linear-chain structure in the nucleus  $^{14}\text{C}$ ”, *Physics Letters, Section B: Nuclear, Elementary Particle and High-Energy Physics* **766**, 11–16 (2017).
- [20] T. Baba and M. Kimura, “Three-body decay of linear-chain states in C 14”, *Physical Review C* **95**, 064318 (2017).
- [21] W. von Oertzen, H. G. Bohlen, M. Milin, T. Kokalova, S. Thummerer, A. Tumino, R. Kalpakchieva, T. N. Massey, Y. Eisermann, G. Graw, T. Faestermann, R. Hertenberger, and H.-F. Wirth, “Search for cluster structure of excited states in  $^{14}\text{C}$ ”, *The European Physical Journal A* **21**, 193–215 (2004).
- [22] T. Suhara and Y. Kanada-En’yo, “Cluster structures of excited states in C 14”, *Physical Review C* **82**, 044301 (2010).
- [23] N. B. de Takacsy, “Direct Solution of the Hill-Wheeler Equation for Alpha-Alpha Scattering”, *Physical Review C* **5**, 1883–1888 (1972).

- [24] T. Baba and M. Kimura, “Structure and decay pattern of the linear-chain state in C 14”, Physical Review C **94**, 044303 (2016).
- [25] J. Suhonen, *From Nucleons to Nucleus: Concepts of Microscopic Nuclear Theory* (Springer, 2007).
- [26] I. J. Thompson and F. Nunes, *Nuclear reactions for astrophysics : principles, calculation and applications of low-energy reactions* (Cambridge University Press, 2009).
- [27] E. P. Wigner and L. Eisenbud, “Higher Angular Momenta and Long Range Interaction in Resonance Reactions”, Physical Review **72**, 29–41 (1947).
- [28] A. M. Lane and R. G. Thomas, “R-Matrix Theory of Nuclear Reactions”, Reviews of Modern Physics **30**, 257–353 (1958).
- [29] P. Descouvemont and D. Baye, “The R-matrix theory”, (2010).
- [30] S. M. Wang, N. Michel, W. Nazarewicz, and F. R. Xu, “Structure and decays of nuclear three-body systems: The Gamow coupled-channel method in Jacobi coordinates”, Physical Review C **96**, 044307 (2017).
- [31] S. M. Wang, Private Communication, 2019.
- [32] D. Suzuki, M. Ford, D. Bazin, W. Mittig, W. Lynch, T. Ahn, S. Aune, E. Galyaev, A. Fritsch, J. Gilbert, F. Montes, A. Shore, J. Yurkon, J. Kolata, J. Browne, A. Howard, A. Roberts, and X. Tang, “Prototype AT-TPC: Toward a new generation active target time projection chamber for radioactive beam experiments”, Nuclear Instruments and Methods in Physics Research Section A: Accelerators, Spectrometers, Detectors and Associated Equipment **691**, 39–54 (2012).
- [33] J. F. Ziegler, M. Ziegler, and J. Biersack, “SRIM – The stopping and range of ions in matter (2010)”, Nuclear Instruments and Methods in Physics Research Section B: Beam Interactions with Materials and Atoms **268**, 1818–1823 (2010).
- [34] J. Bradt, D. Bazin, F. Abu-Nimeh, T. Ahn, Y. Ayyad, S. Beceiro Novo, L. Carpenter, M. Cortesi, M. Kuchera, W. Lynch, W. Mittig, S. Rost, N. Watwood, and J. Yurkon, “Commissioning of the Active-Target Time Projection Chamber”, Nuclear Instruments and Methods in Physics Research Section A: Accelerators, Spectrometers, Detectors and Associated Equipment **875**, 65–79 (2017).
- [35] Y. Giomataris, P. Reboursgeard, J. Robert, and G. Charpak, “MICROMEGAS: a high-granularity position-sensitive gaseous detector for high particle-flux environments”, Nuclear Instruments and Methods in Physics Research Section A: Accelerators, Spectrometers, Detectors and Associated Equipment **376**, 29–35 (1996).

- [36] E. Pollacco, G. Grinyer, F. Abu-Nimeh, T. Ahn, S. Anvar, A. Arokiaraj, Y. Ayyad, H. Baba, M. Babo, P. Baron, D. Bazin, S. Beceiro-Novo, C. Belkhiria, M. Blaizot, B. Blank, J. Bradt, G. Cardella, L. Carpenter, S. Ceruti, E. De Filippo, E. Delagnes, S. De Luca, H. De Witte, F. Druillolle, B. Duclos, F. Favela, A. Fritsch, J. Giovinazzo, C. Gueye, T. Isobe, P. Hellmuth, C. Huss, B. Lachacinski, A. Laffoley, G. Lebertre, L. Legeard, W. Lynch, T. Marchi, L. Martina, C. Maugeais, W. Mittig, L. Nalpas, E. Pagano, J. Pancin, O. Poleshchuk, J. Pedroza, J. Pibernat, S. Primault, R. Raabe, B. Raine, A. Rebii, M. Renaud, T. Roger, P. Roussel-Chomaz, P. Russotto, G. Saccà, F. Saillant, P. Sizun, D. Suzuki, J. Swartz, A. Tizon, N. Usher, G. Wittwer, and J. Yang, “GET: A generic electronics system for TPCs and nuclear physics instrumentation”, Nuclear Instruments and Methods in Physics Research Section A: Accelerators, Spectrometers, Detectors and Associated Equipment **887**, 81–93 (2018).
- [37] F. Becchetti, M. Lee, T. O’Donnell, D. Roberts, J. Kolata, L. Lamm, G. Rogachev, V. Guimarães, P. DeYoung, and S. Vincent, “The TwinSol low-energy radioactive nuclear beam apparatus: status and recent results”, Nuclear Instruments and Methods in Physics Research Section A: Accelerators, Spectrometers, Detectors and Associated Equipment **505**, 377–380 (2003).
- [38] M. Al-Turany, D. Bertini, R. Karabowicz, D. Kresan, P. Malzacher, T. Stockmanns, and F. Uhlig, “The FairRoot framework”, Journal of Physics: Conference Series **396**, 022001 (2012).
- [39] R. O. Duda and P. E. Hart, “Use of the Hough transformation to detect lines and curves in pictures”, Communications of the ACM **15**, 11–15 (1972).
- [40] M. A. Fischler and R. C. Bolles, “Random sample consensus: a paradigm for model fitting with applications to image analysis and automated cartography”, Communications of the ACM **24**, 381–395 (1981).
- [41] L. McFadden and G. Satchler, “Optical-model analysis of the scattering of 24.7 MeV alpha particles”, Nuclear Physics **84**, 177–200 (1966).
- [42] W. von Oertzen, M. Freer, and Y. Kanada-En’yo, “Nuclear clusters and nuclear molecules”, Physics Reports **432**, 43–113 (2006).
- [43] B. Brown and W. Rae, “The Shell-Model Code NuShellX@MSU”, Nuclear Data Sheets **120**, 115–118 (2014).
- [44] R. Brun and F. Rademakers, “Root — an object oriented data analysis framework”, Nuclear Instruments and Methods in Physics Research Section A: Accelerators, Spectrometers, Detectors and Associated Equipment **389**, New Computing Techniques in Physics Research V, 81–86 (1997).

- [45] R. Dalitz, “CXII. On the analysis of  $\tau$ -meson data and the nature of the  $\tau$ -meson”, The London, Edinburgh, and Dublin Philosophical Magazine and Journal of Science **44**, 1068–1080 (1953).
- [46] R. Chechik, A. Breskin, C. Shalem, and D. Mörmann, “Thick GEM-like hole multipliers: properties and possible applications”, Nuclear Instruments and Methods in Physics Research Section A: Accelerators, Spectrometers, Detectors and Associated Equipment **535**, 303–308 (2004).
- [47] M. Cortesi, S. Rost, W. Mittig, Y. A. Limonge, D. Bazin, J. Yurkon, and A. Stolz, “Multi-layer Thick Gas Electron Multiplier (M-THGEM): a new MPDG structure for high-gain operation at low-pressure”, (2016).
- [48] SOLARIS Collaboration, *SOLARIS Whitepaper*, Available at [https://www.anl.gov/sites/www/files/2018-11/solaris\\_white\\_paper\\_final.pdf](https://www.anl.gov/sites/www/files/2018-11/solaris_white_paper_final.pdf), 2018.
- [49] M. P. Kuchera, R. Ramanujan, J. Z. Taylor, R. R. Strauss, D. Bazin, J. Bradt, and R. Chen, “Machine Learning Methods for Track Classification in the AT-TPC”, (2018).